

Thermoelectric Performance of Spark Plasma Sintered $\text{Co}_4\text{Ge}_6\text{Te}_6$ Ternary Skutterudite and
Doped SnTe Compounds

Thermoelectric Performance of Spark Plasma Sintered $\text{Co}_4\text{Ge}_6\text{Te}_6$ Ternary Skutterudite and
Doped SnTe Compounds

by

Masoud Aminzare

A thesis submitted to the School of Graduate Studies

in partial fulfilment of the requirements for the degree

MASTER OF SCIENCE

McMaster University

Hamilton, Ontario

2018

Copyright © Masoud Aminzare, 2018. All rights reserved.

MASTER OF SCIENCE (2018)

Department of Chemistry and Chemical Biology

TITLE: Thermoelectric Performance of Spark Plasma Sintered $\text{Co}_4\text{Ge}_6\text{Te}_6$ Ternary Skutterudite
and Doped SnTe Compounds

AUTHOR: Masoud Aminzare (McMaster University)

SUPERVISOR: Professor Yuriy Mozharivskyj

NUMBER OF PAGES: xiv, 113

Abstract

A large amount of thermal energy is being wasted every day from domestic and industrial usages such as home appliance and heating system, vehicle exhaust and many industrial processes including melting, refining, annealing, and forming. However, there were a significant impact on the environment and economy if one could recover this waste energy and convert it to useful energy for the industrial or domestic consumptions. Thermoelectric (TE) generators as a direct heat conversion technology are a promising approach to scavenge waste heat and to significantly improve the overall energy efficiency of energy-intensive industries. However, the energy conversion efficiency of current thermoelectric materials is insufficient to make the technology economically viable. In this study, we investigated two potential thermoelectric materials, $\text{Co}_4\text{Ge}_6\text{Te}_6$ skutterudite and SnTe , in order to enhance their TE properties.

Among all the state-of-the-art thermoelectric materials, skutterudites have been found to be brilliant candidates for thermoelectric applications due to their remarkable electronic transport properties. Ternary skutterudites are isostructural to their binary analogues with the advantage of lower lattice thermal conductivity than the unfilled binary skutterudites due to the increased structural complexity. Here, in order to further understand this system and its thermoelectric properties, polycrystalline $\text{Co}_4\text{Ge}_6\text{Te}_6$ (CGT) was investigated as a model ternary skutterudite material. Spark plasma sintering (SPS) was used to solidify the samples. The microstructure, phase stability, compositional homogeneity and thermoelectric behaviour of the sintered samples under SPS condition were investigated. We found that SPS can form different crystalline phases due to the migration of highly mobile species inside the sample due to the applied electrical current. There were significant inconsistencies in the physical properties of the samples. We also realized that

Sb-doped CGT samples yielded to the highest power factor reported for the CGT derivatives so far.

Moreover, recent environmental regulations have restricted the use of lead in many real-life applications including thermoelectric power generators. SnTe as a lead-free chalcogenide-based material can be a promising TE candidate to attain high thermoelectric performance. However, the main issue with SnTe is high intrinsic Sn vacancies leading to low Seebeck coefficient and high electrical thermal conductivity. In this regard, we aimed to introduce different metallic species into the SnTe samples ($\text{Sn}_{1-x}\text{A}_x\text{Te}$, A= Co, Ni, Zn, Ge, and $x = 0.01, 0.03, 0.05$) to enhance their TE performance. Each metallic species presented different solubility and microstructural impact on the main SnTe phase and therefore caused variations in physical properties. Ge-doped samples had more uniform microstructures with a very few Ge-rich regions, which implies higher Ge solubility in SnTe matrix. The existence of impurity phases in the Co-, Ni-, Zn-doped samples yields lower lattice thermal conductivities without deterioration in charge transport properties, leading to higher ZT values relative to the pristine SnTe sample. Microhardness of the doped samples is also improved due to the crack growth suppression and crack branching.

Acknowledgements

It is my immense pleasure to convey my appreciation to my supervisor, Prof. Yuriy Mozharivskij, for his support, patience, academic guidance, and great encouragements in many ways during my M.Sc. study in the Chemistry and Chemical Biology Department at McMaster University, Canada.

It is also my pleasure to give my gratitude to my committee member, Prof. John Greedan for his support and kind advice on the road to my research purposes.

Thank you to Dr. Jim Britten, Ms. Victoria Jarvis, Mr. Jim Garrett, and all the fantastic, hard-working staff of the Department of Chemistry, BIMR and McMaster University for providing me such a brilliant environment and opportunity to learn and gain valuable experiences. I would also like to express my special appreciation to Dr. Yu-Chih Tseng from CANMET Materials, Natural Resources Canada and Prof. Kuei-Hsien Chen from Institute of Atomic and Molecular Sciences, Academia Sinica, Taipei, Taiwan for their contributions measuring TE properties of my samples.

I would like to thank my dear friends and all past and present colleagues in our group (Dr. Fang Yuan, Timothy Lo, Allan He, Sergei Novikov) who made my MSc study at McMaster University a productive, enjoyable, and memorable experience for my whole life.

The last but not the least, I would like to express my gratefulness to my brilliant and selfless wife, and my family for their great support and love during my study. I would never have gone so far without their true love and support.

Table of Contents

Chapter 1. Part A. Thermoelectricity	15
1-1. Introduction.....	15
1-2. Thermoelectric effects.....	16
1-2-1. Seebeck and Peltier effects.....	16
1-2-2. Thomson effect.....	18
1-3. Thermoelectric parameters.....	19
1-3-1. Electrical conductivity.....	19
1-3-2. Seebeck coefficient.....	19
1-3-3. Power Factor	22
1-3-3-1. Quantum Confinement Effect	22
1-3-3-2. Electron Filtering	22
1-3-3-3. Band Engineering.....	23
1-3-4. Thermal conductivity	25
1-3-4-1. Alloying to lower thermal conductivity	26
1-3-4-2. Reduction of thermal conductivity by nanostructures	27
1-3-4-3. Interface and/or Boundary Scattering	27
1-3-4-4. Nanosized Defect Scattering.....	28
Chapter 1. Part B. Some experimental and characterization methods	30
1-4. Sample preparation	30
1-5. Materials characterization	32
1-5-1. X-ray Powder Diffraction (XRD).....	32
1-5-2. Scanning electron microscopy (SEM).....	33
1-5-3. Energy-dispersive X-ray spectroscopy (EDS).....	34
1-6. Transport Properties Measurements.....	35
1-6-1. Electrical conductivity and Seebeck coefficient measurements	35
1-6-2. Thermal conductivity measurements.....	35
1-7. References.....	38
Chapter 2- Effect of Spark Plasma Sintering and Sb Doping on the Thermoelectric Properties of $\text{Co}_4\text{Ge}_6\text{Te}_6$ Skutterudite	43
2-1. Abstract.....	43
2-2. Introduction	43
2-3. Experimental procedure.....	53

2-4. Results and discussions	55
2-5. Conclusion	79
2-6. References	80
Chapter 3. Effect of Single Metal Doping on the Thermoelectric Properties of SnTe	85
3-1. Abstract.....	85
3-2. Introduction	85
3-3. Experimental procedure.....	88
3-4. Results and Discussions.....	89
3-5. Conclusion	108
3-6. References	109

List of Figures and Tables

Figure 1-1. (a) Thomas Johann Seebeck, (b) schematic illustrations of Seebeck effect (c) power generation efficiency as a function of average zT_{ave} (d) Jean Charles Athanase Peltier, and (e) schematic illustrations of Peltier effect (f) cooling efficiency as a function of average zT_{ave} [3] (g) thermoelectric module [1].....	17
Figure 1-2. Comparison between thermoelectric generators efficiency as a function of T_{hot} ($T_{\text{cold}} = 300 \text{ K}$) and efficiencies for conventional mechanical engines along with the Carnot limit [5, 6].....	18
Figure 1-3. Dependence of electrical conductivity, Seebeck coefficient and thermal conductivity on carrier concentration [6].....	21
Figure 1-4. schematic illustration of changes in Electronic density of states for (left to right) a bulk 3D crystalline semiconductor, a 2D quantum well, a 1D nanowire or nanotube and a 0D quantum dot [5].....	23
Figure 1-5. (a) Schematic demonstrates the resonant level on the DOS [19, 21], and (b) schematic of band convergence in $\text{PbTe}_{0.85}\text{Se}_{0.15}$. At 500 K, the two valence bands converge, resulting in transport contributions from both the L and Σ bands [18, 19].....	24
Figure 1-6. (a) Reduction of thermal conductivity of an $\text{Si}_x\text{Ge}_{1-x}$ alloy as a function of Si content in Ge. (b) Schematic illustration of alloy scattering. short-wavelength phonons are scattered by atomic substitutions [13].....	28
Figure 1-7. (a) Comparison of thermal conductivities of micrograined and nanograined alloys. Solid lines are calculated phonon contributions of bulk and nanograin samples. (b) Figures of merit for micrograined and nanograined alloys [36]. (c) illustration of phonon grain boundary scattering in micrograins and nanograins samples [13].....	29

Figure 1-8. Schematic of thermal conductivity reduction by nanoparticle scattering [13].....	29
Figure 1-9. Schematic diagram of the sample preparation process and sintering of (a) $\text{Co}_4\text{Ge}_6\text{Te}_6$ and (b) SnTe	31
Figure 1-10. illustration of Bragg's law.....	32
Figure 1-11. a schematic diagram showing (a) electrical conductivity and Seebeck coefficient, (b) thermal conductivity measurements.....	37
Figure 2-1. Crystal structure of skutterudite (CoSb_3). The Co and Sb atoms are represented by red and blue balls, respectively. Filler atoms are shown by big yellow balls.....	46
Figure 2-2. ReO_3 crystal structure and octahedral network. Re is in blue and oxygen is in red colour.....	46
Figure 2-3. (a) the octahedral coordination of one of the metal atoms in the ReO_3 structure, (b) the distortion of the anion sublattice in the ReO_3 structure which results in the skutterudite structure, and (c) the skutterudite structure, with its characteristic anion rings [5]. Metal atoms and anions are represented by open and black circles, respectively. (d) The four-membered rings in CoSb_3 and (e) $\text{CoGe}_{1.5}\text{Te}_{1.5}$ [17].....	47
Figure 2-4. Powder neutron diffraction data at different temperature for $\text{CoGe}_{1.5}\text{Te}_{1.5}$ showing the disappearance of the superstructure reflections (labelled with *) during the phase transition [18].....	49
Figure 2-5. (a) Powder X-ray diffraction data for $\text{Co}_4\text{Ge}_6\text{Te}_6$ at different annealing steps. The pattern which is labelled as the reference belongs to [16] (ICDS code 166638) for better comparison. (b) Final observed (crosses), calculated (solid line) and difference (full lower line) profiles from Rietveld refinement of the synthesized and sintered samples using $R\bar{3}$ models....	57

Figure 2-6. (a) Powder X-ray diffraction data before and after sintering. (b) Final observed (crosses), calculated (solid line) and difference (full lower line) profiles from Rietveld refinement of the sintered sample using $Im\bar{3}$ model.....58

Figure 2-7. Powder XRD patterns of samples with different Ge contents after the 3rd annealing step. A cross sign (X) indicates the GeTe impurity phase and the plus signs (+) indicate the CoTe₂ impurity phase.....61

Figure 2-8. Powder XRD patterns of samples with different Ge contents after SPS sintering.....61

Figure 2-9. Electrical conductivity, Seebeck coefficient, and Power factors of stoichiometry CGT sample over the temperature range 100-500 °C. Two bars from a sample have been cut and measured.....63

Figure 2-10. X-ray diffraction patterns of bulk Co₄Ge₆Te₆ sample after sintering at 610 °C for 10 min from different places of (a) top side and (b) bottom side of the sample. (c) Rietveld refinement of X-ray diffraction pattern for the middle spot in (a) (Co₄Ge₆Te₆ sample after sintering) including profile fit, profile difference, and profile residuals.....64

Figure 2-11. X-ray diffraction patterns from different places at the (a) top and (b) bottom sides of the bulk Co₄Ge₆Te₆ sample after sintering at 575 °C for 25 min.....66

Figure 2-12. X-ray diffraction patterns from different places at the (a) top and (b) bottom sides of the bulk Co₄Ge₆Te₆ sample after sintering at 535 °C for 40 min.....67

Figure 2-13. X-ray diffraction patterns from different places at the (a) top and (b) bottom sides of the bulk Co₄Ge₆Te₆ sample after sintering at 500 °C for 60 min.....68

Figure 2-14. SEM micrographs of the surface of the bulk Co₄Ge₆Te₆ sample after SPS. Chemical compositions of the labelled regions are determined by EDX analysis.....69

Figure 2-15. (a) Secondary electron image, and (b-d) elemental mappings of Co, Ge, and Te in the polished $\text{Co}_4\text{Ge}_6\text{Te}_6$ sample prepared via SPS. Ge is almost distributed uniformly while there are some Co-rich and Te-deficient regions.....71

Figure 2-16. Back-scattered electron image of the bulk $\text{Co}_4\text{Ge}_6\text{Te}_6$ sample. Non-uniform contrast indicates differences in composition and phase distribution throughout the sample.....72

Figure 2-17. Schematic configuration of SPS equipment showing the electrical current pathways within the sample and graphite die (a) without and (b) with using Mica films.....75

Figure 2-18. Electrical conductivity and Seebeck coefficient of $\text{Co}_4\text{Ge}_6\text{Te}_6$ samples spark plasma sintered (a, b) without (c, d) with Mica films. Two bars have been cut and measured for each sample. The reference results are extracted from ref [18].....76

Figure 2-19. Powder XRD patterns of synthesised Sb-doped samples after the 3rd annealing step.....77

Figure 2-20. Electrical conductivity, seebeck coefficient and power factor of Sb-doped specimens as a function of temperature.....78

Figure 3-1. (a, c, e, g) Powder XRD patterns of the $\text{Sn}_{1-x}\text{A}_x\text{Te}$ samples doped with Co, Ni, Zn, and Ge from 1 to 5%. (b, d, f, h) Rietveld refinement results for the 5% doped samples. The impurity phases are very well matched with CoTe , Ni_3SnTe_2 and ZnTe for the Co-, Ni-, and Zn-doped samples, respectively. The refined pattern for the 5% Ge-doped sample shows no detectable impurity peaks.....90

Figure 3-2. (a) Secondary electron image, (b) back-scattered electron image and (c-e) elemental mappings of Sn, Te and Co in the polished $\text{Sn}_{0.95}\text{Co}_{0.05}\text{Te}$ sample prepared via SPS. Co-richer precipitates are found on the grain boundaries with the average grain size of $\sim 10 \mu\text{m}$. Lack of Sn on the grain boundaries and

uniform Te distribution confirms the formation of CoTe on the grain boundaries, in agreement with the XRD results (Figure 1 (a) and (b)).....93

Figure 3-3. (a) Secondary electron image, (b) back-scattered electron image and (c-e) elemental mappings of Sn, Te and Ni in the polished $\text{Sn}_{0.95}\text{Ni}_{0.05}\text{Te}$ sample prepared via SPS. A Ni-richer phase precipitates on the grain boundaries and within the grains with the average grain size $\leq 10 \mu\text{m}$. Significant reduction in the Sn signal and slight reduction in the Te signal on the grain boundaries is consistent with the formation of Ni_3SnTe_2 as identified in the XRD data (Figure 1 (g) and (h)).....94

Figure 3-4. (a) Secondary electron image, (b) back-scattered electron image and (c-e) elemental mappings of Sn, Te and Zn in the polished $\text{Sn}_{0.95}\text{Zn}_{0.05}\text{Te}$ sample prepared via SPS. Sn is absent in the Zn-rich areas, while the Te distribution is uniform throughout the sample. The elemental mapping supports the formation of the ZnTe impurity, as witnessed from the XRD data (Figure 1 (c) and (d)).....95

Figure 3-5. (a) Secondary electron image, (b) back-scattered electron image and (c-e) elemental mappings of Sn, Te and Ge in the polished $\text{Sn}_{0.95}\text{Ge}_{0.05}\text{Te}$ sample prepared via SPS. Ge distribution is almost uniform with very few Ge rich regions smaller than $1 \mu\text{m}$. Sn and Te are deficient in the Ge-rich regions. The Ge-rich regions are not detected in the XRD patterns due to their small size and numbers (Figure 1 (e) and (f)).....96

Figure 3-6. Temperature-dependent electrical conductivity for (a) $\text{Sn}_{1-x}\text{Co}_x\text{Te}$, (b) $\text{Sn}_{1-x}\text{Zn}_x\text{Te}$, (c) $\text{Sn}_{1-x}\text{Ge}_x\text{Te}$, and (d) $\text{Sn}_{1-x}\text{Ni}_x\text{Te}$. All samples demonstrate metallic-type behaviour for electrical conductivity..97

Figure 3-7. Temperature-dependent Seebeck coefficient of pure SnTe in comparison with (a) $\text{Sn}_{1-x}\text{Co}_x\text{Te}$, (b) $\text{Sn}_{1-x}\text{Zn}_x\text{Te}$, (c) $\text{Sn}_{1-x}\text{Ge}_x\text{Te}$, and (d) $\text{Sn}_{1-x}\text{Ni}_x\text{Te}$. Samples with different dopants display thermopower values close to that of pure SnTe, except for the Ni-doped samples.....98

Figure 3-8. Temperature dependent power factor of (a) $\text{Sn}_{1-x}\text{Co}_x\text{Te}$, (b) $\text{Sn}_{1-x}\text{Zn}_x\text{Te}$, (c) $\text{Sn}_{1-x}\text{Ge}_x\text{Te}$, and (d) $\text{Sn}_{1-x}\text{Ni}_x\text{Te}$ in comparison with the pure SnTe. Doped samples possess increased power factors, especially at high temperatures.....99

Figure 3-9. Total thermal conductivity, κ_{total} , of (a) $\text{Sn}_{1-x}\text{Co}_x\text{Te}$, (b) $\text{Sn}_{1-x}\text{Zn}_x\text{Te}$, (c) $\text{Sn}_{1-x}\text{Ge}_x\text{Te}$, and (d) $\text{Sn}_{1-x}\text{Ni}_x\text{Te}$ in comparison with pure SnTe as a function of temperature.....100

Figure 3-10. Comparison of the lattice thermal conductivity for different singly-doped SnTe samples [14, 15, 17, 24, 25, 36-40] at 575-600 °C. The lattice thermal conductivities of our Co-, Ni-, and Ge-doped samples are comparable to the lowest κ_L values reported for SnTe so far.....103

Figure 3-11. The dimensionless thermoelectric figure of merit, ZT, of (a) $\text{Sn}_{1-x}\text{Co}_x\text{Te}$, (b) $\text{Sn}_{1-x}\text{Zn}_x\text{Te}$, (c) $\text{Sn}_{1-x}\text{Ge}_x\text{Te}$, and (d) $\text{Sn}_{1-x}\text{Ni}_x\text{Te}$ in comparison with the pure SnTe from room temperature to 600 oC. All doped samples exhibit ZT values higher than that of the pure sample, especially at high temperatures.....104

Figure 3-12. Average of the dimensionless thermoelectric figure of merit, ZT_{ave} (average of all ZT values from room temperature to 600 oC), of $\text{Sn}_{1-x}\text{Co}_x\text{Te}$, $\text{Sn}_{1-x}\text{Zn}_x\text{Te}$, $\text{Sn}_{1-x}\text{Ge}_x\text{Te}$, and $\text{Sn}_{1-x}\text{Ni}_x\text{Te}$ in comparison with pure SnTe. All doped samples demonstrate ZT_{ave} values higher than that of the pure sample. The maximum increase in ZT_{ave} is about 163%.....105

Figure 3-13. (top) Vickers microhardness values, HV, for the 5% Co-, Ni-, Zn-, and Ge-doped SnTe in comparison with the pure sample. (bottom) Crack growth suppression and crack branching are depicted as the main toughening mechanisms.....106

Table 2-1. Thermoelectric properties of some ternary skutterudite compounds.....	50
Table 2-2. Sample preparation parameters during synthesis, annealing and sintering.....	54
Table 2-3. The weight percentage of different phases in the middle of the $\text{Co}_4\text{Ge}_6\text{Te}_6$ sample after SPS sintering obtained from the Rietveld refinement.....	65
Table 2-4. EDX quantitative analysis of 4 different areas of the $\text{Co}_4\text{Ge}_6\text{Te}_6$ sample shown in Figure 2-14. The nominal stoichiometric composition is $\text{Co}_{25}\text{Ge}_{37.5}\text{Te}_{37.5}$ in atomic (Atm%) percentage.....	70
Table 2-5. EDX quantitative analysis of 10 different spots of $\text{Co}_4\text{Ge}_6\text{Te}_6$ sample has been shown in figure 2-16 (all values are in weight percentage). The nominal stoichiometric composition is $\text{Co}_{25}\text{Ge}_{37.5}\text{Te}_{37.5}$ in atomic percentage.....	72
Table 3-1. Lattice parameters and weight percentages of secondary phases in the Co-, Ni, Zn-, Ge-doped samples after SPS.....	91
Table 3-2. Room and high temperature total thermal conductivity κ_t , Lorenz number, electronic and lattice thermal conductivity for the pristine and 5% Co-, Ni-, Zn-, and Ge-doped samples...	101

Chapter 1. Part A. Thermoelectricity

1-1. Introduction

The global demand for energy is increasing every day due to the huge industrial and domestic usage. Although using more energy seems to be unavoidable, it must be controlled and managed. Renewable energy technologies have been in great attention nowadays due to the increasing price of fossil fuels, environmental issues and industrial growth. While the total energy consumption rises every year worldwide, only 10% of this energy supply is generated by green sources such as solar and the wind; the rest is made of fossil fuel combustion with an efficiency of 30-40%. In other words, only one-third of energy is utilised and the rest is lost as waste heat, which has a catastrophic impact on both the economy and environment. Therefore, it is necessary to retrieve waste heat in order to enhance the efficiency of the energy consumption. Here, development of thermoelectric materials can play a vital role; as they can scavenge the waste heat and convert it into useful electricity [1-3].

TE modules possess the several benefits such as low cost, reliability, no moving parts, plain configuration, scalability, low noise and being environmentally friendly. They are potentially applicable in different areas from low power applications to large-scale waste heat recovery systems, for instance in automobiles, computers, refrigerators, watches, etc [2, 4].

However, TE devices have still low performing efficiency compared to other state of art technologies, which makes their operation restricted. Recently, researchers have intensively tried several types of compounds to find appropriate thermoelectric materials with improved properties. Scientists have applied different phenomena like band convergence in semiconductors to increase the electrical conductivity or optimise the Seebeck coefficient, or hierarchical structures to reduce

the thermal conductivity by increasing phonon scattering inside the structure. In addition, some materials with intrinsically low thermal conductivity have been developed for TE applications [1-3]. Although the outcomes so far achieved are very promising compared to a decade ago, more efficient, stable and cheaper materials are required.

1-2. Thermoelectric effects

1-2-1. Seebeck and Peltier effects

In 1821, Seebeck found that if a pair of different metals in a circuit is warmed up, while the other side of this pair maintained cold, then current would flow in the system. This phenomenon is named “Seebeck effect” in honour of him. On the other hand, in 1834, Peltier discovered heat is released or absorbed at the junction of two dissimilar metals when an electric current passed through a circuit consisting of these metals (Figure 1-1) [1, 2].

Thermoelectric modules consist of several p-n semiconductor pairs, which are thermally in parallel but electrically in series in order to let electrons and holes move in the same direction pulling heat from one end to the other (Figure 1-1) [1].

The performance of thermoelectric materials can be defined by the term “figure of merit”, zT :

$$zT = \frac{S^2 \sigma T}{\kappa} \quad (1)$$

where S is the Seebeck coefficient, σ the electrical conductivity, κ the thermal conductivity, T the absolute temperature, and $S^2 \sigma$ is called power factor [2, 3]. Very high zT close to infinity gives the highest performance equivalent to the Carnot efficiency (figure 1-2). However, this is not achievable due to the low performances of available thermoelectric materials. Therefore, ZT

enhancement through optimization of the ZT -governing parameters becomes a priority in the thermoelectric research [2, 3].

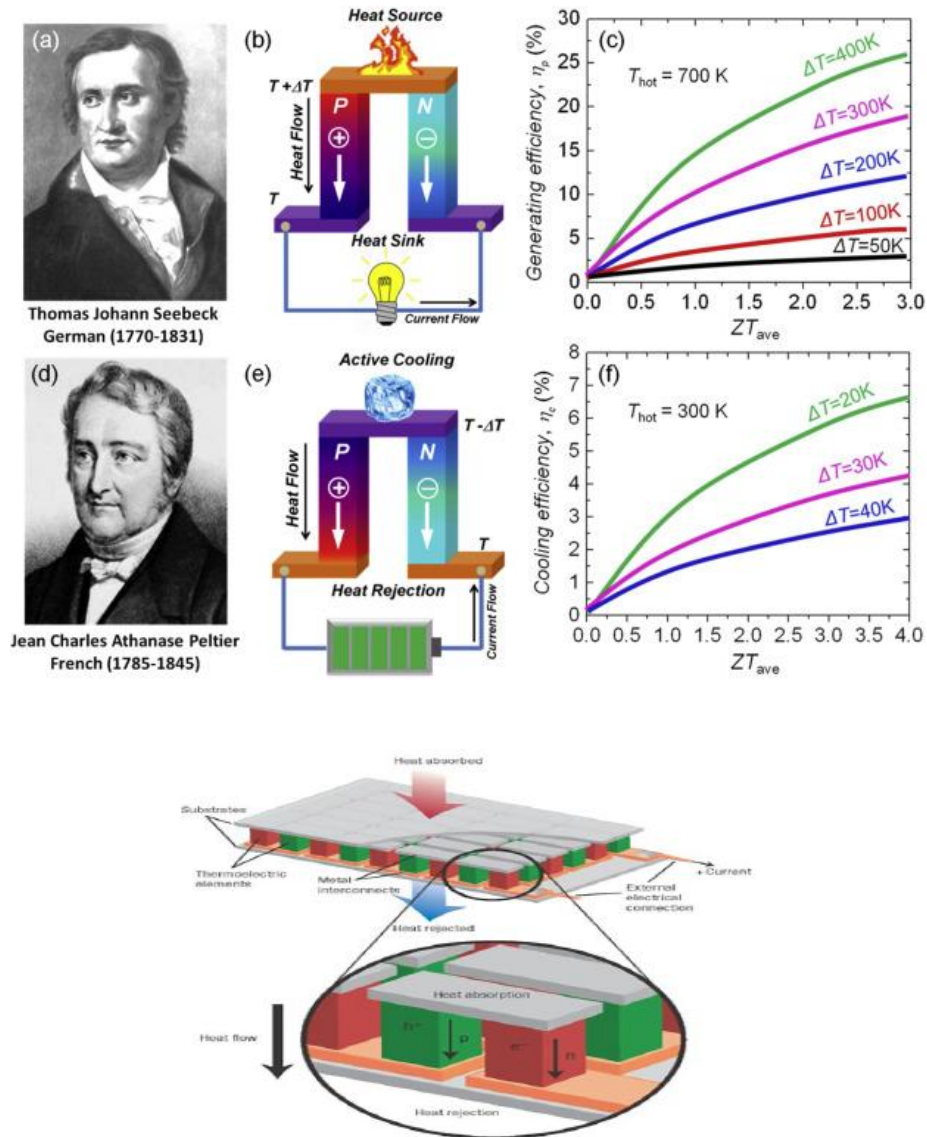


Figure 1-1. (a) Thomas Johann Seebeck, (b) schematic illustrations of Seebeck effect (c) power generation efficiency as a function of average ZT_{ave} (d) Jean Charles Athanase Peltier, and (e) schematic illustrations of Peltier effect (f) cooling efficiency as a function of average ZT_{ave} [3]

(g) thermoelectric module [1].

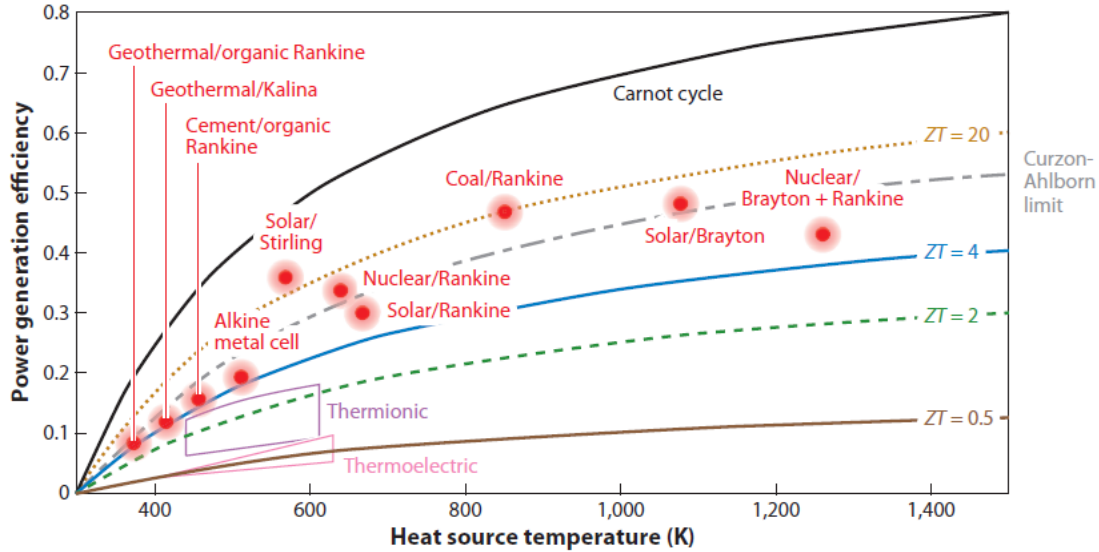


Figure 1-2. Comparison between thermoelectric generators efficiency as a function of T_{hot} ($T_{\text{cold}} = 300 \text{ K}$) and efficiencies for conventional mechanical engines along with the Carnot limit [5, 6].

1-2-2. Thomson effect

In addition to the Seebeck effect and Peltier effect, William Thomson in 1851 observed the third thermoelectric effect, the Thomson effect. This effect explains that heating or cooling occurs when the current passes through a conductor with a temperature gradient. It should be highlighted that the Seebeck, Peltier, and Thomson effects are different appearances of one phenomenon and can be related to and understood by the Seebeck coefficient.

The Thomson effect is present for a single conductor, unlike the Peltier and Seebeck effects. The relationships between the thermoelectric coefficients are known as Kelvin's laws, are:

$$\pi = ST \quad (2)$$

$$\tau = T(dS/dT) \quad (3)$$

1-3. Thermoelectric parameters

1-3-1. Electrical conductivity

Electrical conductivity ($\sigma = 1/\rho$, ρ is electrical resistivity) is a fundamental matter property that indicates how well electrical current can pass through a given material. Accordingly, there are three main types of materials based on their electrical conductivity values: metals ($\rho \sim 10^{-6} \Omega\cdot\text{m}$ or less), semiconductors, and insulators ($\rho \sim 10^6 \Omega\cdot\text{m}$ or higher). The conductivity of a semiconductor is in between those of metals and insulator materials. For thermoelectric materials, it has been suggested that 10^{-3} to $10^{-2} \Omega\cdot\text{m}$ is the preferred range for electrical resistivity [7] which is typical for semiconductors.

Electrical conductivity is temperature dependent, however, the change of conductivity for metals and semiconductors as a function of temperature is different. Metals conductivity drop as temperature rises, while the conductivity of semiconductors increases with temperature. Semiconductors have a very low electrical conductivity at low temperatures due to the limited number of free charge carriers [8]. Furthermore, electrical conductivity depends on materials intrinsic parameters such as carrier concentration, the mean free path of the charge carriers, etc.:

$$\sigma = en\mu = ne^2 \frac{\tau(E)}{m^*} \quad (4)$$

in which n is the carrier concentration, μ the mobility, τ the relaxation time and m^* the charge carrier effective mass [2, 3]. Higher σ can be obtained by increasing τ . i.e. increasing the time between consecutive scattering events.

1-3-2. Seebeck coefficient

As mentioned above for the definition of the Seebeck effect, a temperature difference applied in a conductor or semiconductor generates a voltage difference or an electric field [9]. The magnitude

of this voltage/electric field is called Seebeck coefficient or thermopower ($S = \Delta V/\Delta T$) which is the voltage developed per unit temperature difference in a conductor and is expressed in units of $\mu\text{V}/\text{K}$. Materials represent different thermoelectric sensitivities or Seebeck coefficients. As an example, iron possesses a Seebeck coefficient around $20 \mu\text{V}/\text{K}$ at 0°C , which means a positive voltage of $20 \mu\text{V}$ is generated in iron for 1°C temperature difference near 0°C . Thermoelectric devices perform as electrical power generators using the Seebeck effect (figure 1-1) [10, 11]. As there is one dominant carrier type (electrons or holes) in each semiconductor, Seebeck coefficients can also possess negative numbers, an indication for an n-type or electron dominated semiconductor. For instance, the Seebeck coefficient of copper-nickel alloy (constantan) is about $-35 \mu\text{V}/^\circ\text{C}$ at 0°C .

Thermopower above $200 \mu\text{V}/\text{K}$ is required to acquire $ZT > 2$, thus semiconductors are promising for thermoelectric application as their Seebeck coefficient can reach $100 \mu\text{V}/\text{K}$ or higher, while most metals possess Seebeck coefficients of $10 \mu\text{V}/\text{K}$ or less. It is also worth to mention that Seebeck coefficient linearly depends on temperature only for slight changes in temperature (very narrow temperature gradient), and this relationship turns out to be non-linear for larger temperature differences [10, 12]. It is therefore important to indicate at which temperature the Seebeck coefficient is being measured.

The Seebeck coefficient also depends on the material property (mainly carrier concentration and effective mass) [2, 3]:

$$S = \frac{\Delta V}{\Delta T} = \frac{8\pi^2 k_B^2 T}{3eh^2} m^* \left(\frac{\pi}{3n}\right)^{\frac{2}{3}} \quad (5)$$

The high-performance TE materials need to have high S and σ , however, improvement in zT by maximising the S and σ can be a challenge due to the competition between Seebeck coefficient and electrical conductivity. For instance, if one wants to increase the S by increasing the carrier effective mass, he/she will simultaneously decrease the electrical conductivity because μ is lower for charge carriers with a heavier mass m^* . The same thing can happen when manipulating carrier concentrations; while an increase in the carrier concentration raises the σ , it conversely decreases the S . Therefore, increasing band mass or carrier concentration is not always beneficial for optimizing the zT value.

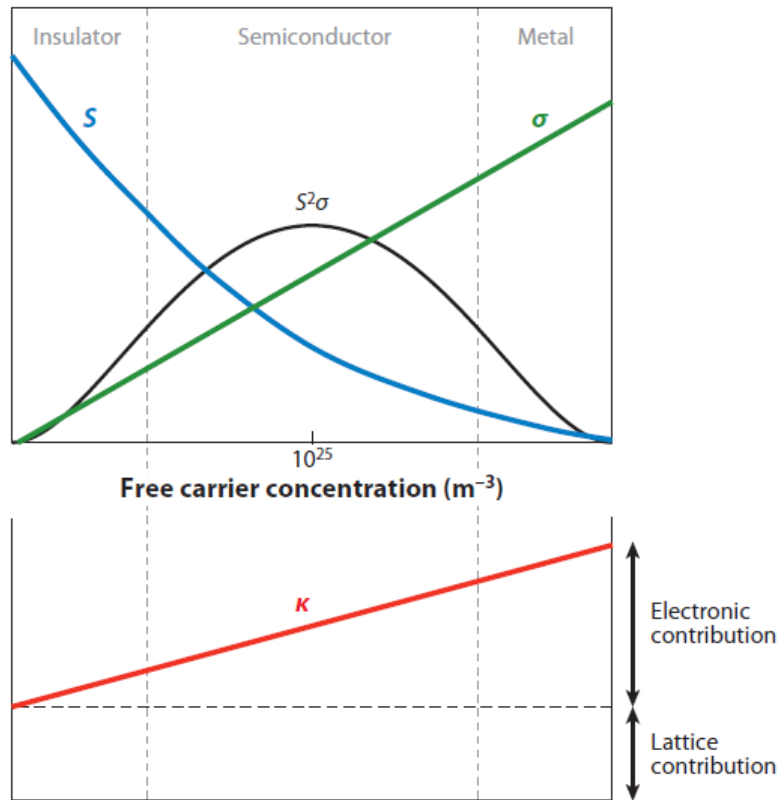


Figure 1-3. Dependence of electrical conductivity, Seebeck coefficient and thermal conductivity on carrier concentration [6].

Figure 1-3 illustrates the relationship between the carrier concentration and S , σ for semiconductors, metals and insulators. S decreases with increasing carrier concentration, while σ rises.

1-3-3. Power Factor

As seen in Figure 1-3, highest power factor is obtained only for some carrier concentration because the Seebeck coefficient and electrical conductivity have different dependence on carrier concentration, so it is important to adjust the carrier concentration close to the optimum value, which is temperature dependent, and differs based on the material used [13].

1-3-3-1. Quantum Confinement Effect

As explained in the above sections, the Seebeck coefficient, electrical conductivity, and power factor are interdependent in nature. However, there are approaches that one can uncouple these three parameters. For example, one can increase the Seebeck coefficient without altering the electrical conductivity too much by reducing the dimensionality of a material which will change the electron density of states due to the electron confinement [13]. In other words, the quantum confinement effect introduces discrete and sharp densities of states into the low-dimensional materials. Therefore, it is possible to improve the Seebeck coefficient without decreasing electrical conductivity significantly. Such approach requires very small dimensions lower than 20 nm, low temperatures, and precise doping to position the Fermi level near a sharp DOS peak.

1-3-3-2. Electron Filtering

An energy barrier which is formed at the intersection between different semiconductors, or between a semiconductor and a metal, can act as a filter for charge carriers. It means high-energy charge species can pass this barrier while charge carriers with energy less than the barrier height are blocked and scattered. Accordingly, the Seebeck coefficient intensely increases while electrical resistivity fluctuates slightly [13].

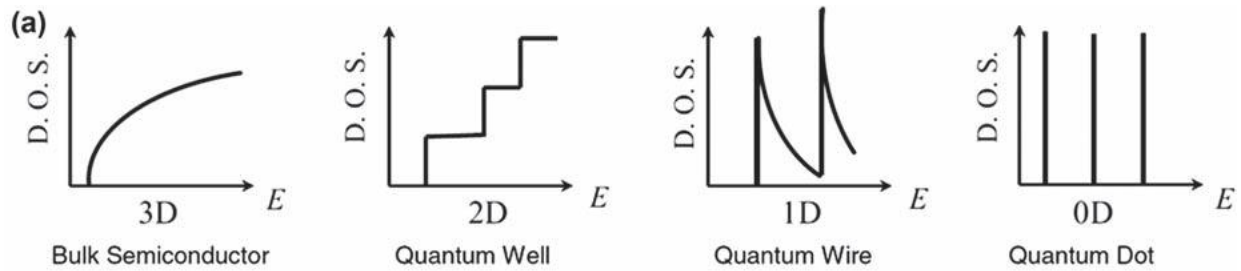


Figure 1-4. schematic illustration of changes in Electronic density of states for (left to right) a bulk 3D crystalline semiconductor, a 2D quantum well, a 1D nanowire or nanotube and a 0D quantum dot [5].

1-3-3-3. Band Engineering

The electrical transport behaviour of a material principally depends on its band structure, therefore the overall TE performance can be optimized by proper band structure adjustment. Recent studies have reported that band engineering via (1) band gap enlargement [14] to stabilize carrier concentration; (2) resonant state near the Fermi level [15, 16] to increase Seebeck coefficient; and (3) band convergence [17, 18] to improve Seebeck coefficient, can enhance the power factor [19].

Minor carriers which are thermally excited at elevated temperatures can raise the total charge carrier density and consequently reduce zT due to Seebeck coefficient reduction and electronic thermal conductivity enhancement. Previous studies revealed that band gap adjustment of a semiconductor can efficiently be tuned by proper doping, and the enlarged band gap can suppress the minor carriers by increasing the thermal excitation temperature of minor charge carriers toward a higher temperature range [14, 19, 20].

The energy level of some impurities lies in the conduction or valence bands of the main material, e.g. thallium in PbTe [5], and generates “resonant” states inside the valence or conduction bands due to a distortion of the host band (Figure 1-5). This results in significant increase of the effective mass, m^* when the Fermi level is positioned on the rapidly rising side of the distorted density of

states. As the result, Seebeck coefficient increases without a major reduction in the electrical conductivity and carrier concentrations [13, 15, 16, 19].

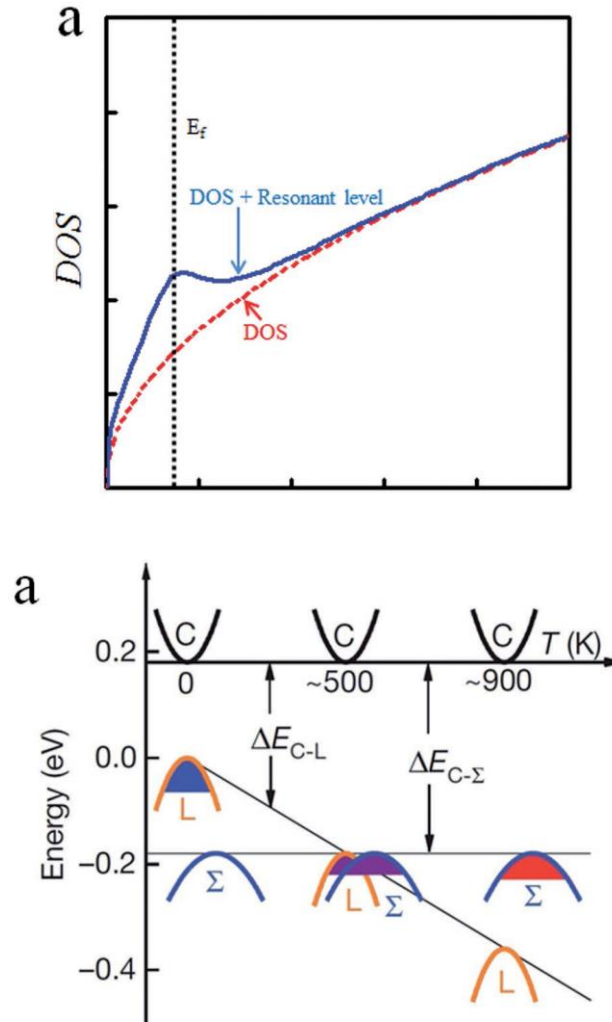


Figure 1-5. (a) Schematic demonstrates the resonant level on the DOS [19, 21], and (b) schematic of band convergence in $\text{PbTe}_{0.85}\text{Se}_{0.15}$. At 500 K, the two valence bands converge, resulting in transport contributions from both the L and Σ bands [18, 19].

The m^* can be also increased when multiple electronic bands of materials converge through appropriate doping and increasing temperature (Figure 1-5 (b)), while keeping mobility of charge carriers (μ) unaffected [18, 19]. For example, two-valence band model of PbTe consists of a

principle valence band (L band) active at low temperature and a secondary valence band (Σ band) dominating at higher temperatures (Figure 1-5(b)) [19]. Small energy separation ($\Delta E = E_{VL} - E_{V\Sigma}$) of ≈ 0.2 eV is present between these two valence bands [18, 19], which turns out to be smaller with Se doping in PbTe structure at 500 K. therefore, band convergence between the L band and Σ band occurs and leads to an increased m^* without reducing μ too much [18]. As a result, PF can be greatly increased [19].

1-3-4. Thermal conductivity

Thermal conductivity (κ) is another important parameter in ZT formula which describes how the heat is transferred in the material [2, 3]. Low thermal conductivity in addition to the high electrical conductivity and high thermopower is essential for a high performance thermoelectric material. Electrical conductivity and the Seebeck coefficient are only dependent on the electronic properties of the material, however, two different terms are contributed to the thermal conductivity, κ_t , lattice thermal conductivity (phonons travelling through the lattice), κ_l and electrical thermal conductivity (electrons and holes transporting heat), κ_e [22].

$$\kappa_t = \kappa_l + \kappa_e \quad (6)$$

It is not straightforward to obtain a higher thermoelectric figure of merit by simply increasing the electrical conductivity and minimizing the thermal conductivity, as there is a correlation between the two according to the Wiedemann-Franz equation; the electronic contribution to the thermal conductivity (κ_e) is directly related to the σ :

$$\kappa_e = \sigma L_0 T \quad (7)$$

where L_0 is the Lorentz number: $2.44 \times 10^{-8} \text{ W}\Omega\text{K}^{-2}$.

Therefore, electrons not only conduct the electricity but also they conduct heat inside the material (Fig. 2) [2, 3]. So, this means that increasing the σ which is suitable to boost the zT value, can also increase the electronic thermal conductivity, which decreases the zT . The power factor can be improved by optimizing the charge carrier concentration, carrier effective masses, both of which depend on the material's electronic structure, while decreasing the lattice thermal conductivity requires totally different strategies, which depend on the rigidity, atomic masses, and other characteristics of the lattice [23]. In this regard, the phonon-glass electron-crystal (PGEC) concept, proposed by Nolas et al. [10] is a valuable approach for the development of new thermoelectric materials. A PGEC material has electronic properties like crystalline solids while its thermal properties are similar to those of an amorphous material.

An ideal thermoelectric material should contain high-mobility semiconductor areas with optimized electronic structure along with phonon-glass areas without destroying the charge carrier movement [24].

There are several important factors that can help to enhance zT via the reduction of lattice thermal conductivity: (a) using crystalline materials with complex structures, (ii) introducing heavier and bigger, weakly-bonded atoms into the structure, (iii) the existence of inclusions and/or impurities, (iv) the formation of solid solutions and (v) applying a large number of grain boundaries [25]. Furthermore, nanostructuring is another very powerful method to reduce the lattice thermal conductivity; it allows to achieve the zT value above 1-2 in comparison with values < 1 for bulk materials [26].

1-3-4-1. Alloying to lower thermal conductivity

Alloying has been used for longtime as a conventional method to decrease thermal conductivity in crystalline materials [27]. Figure 1-6 represents the thermal conductivity of $\text{Si}_x\text{Ge}_{1-x}$ alloy system [28].

Accordingly, the thermal conductivity of an alloy of Si and Ge is much lower than the values for pure Si and Ge. The lowest thermal conductivity is at about 50-70% Si and Ge, called the alloy limit, while it is very challenging to decrease the thermal conductivity lower than this value with the same crystallinity. However, one can reduce the alloy limit by using nanostructures [29-32]. Phonon scattering due to atomic substitutions, known as alloy scattering (Figure 1-6(b)), is responsible for lower thermal conductivity of alloys. Particularly, atomic-scale defects scatter high-frequency phonons effectively [13].

1-3-4-2. Reduction of thermal conductivity by nanostructures

The phonon scattering increases at the interfaces, so using nanostructures will decrease the lattice thermal conductivity due to the enlarged surface-to-volume ratio. Although nanostructuring raises the electron scattering at the same time, it is still possible to lower down the lattice thermal conductivity without severe effect on the electrical conductivity. Such approach requires an electron mean free path shorter than the phonon mean free path [33]. Overall, the mean free path of phonons and electrons are on the order of ~ 100 nm and ~ 10 nm, respectively. Therefore, phonons can be effectively scattered and the transport of electrons is not changed too much if the length scale of the particles is between the mean free paths of phonons and electrons [13, 27, 34].

1-3-4-3. Interface and/or Boundary Scattering

1-dimensional (1D, e.g. nanowire), 2D (e.g. superlattice or multi-layers) or 3D materials can function as nanostructures and be used to reduce the lattice thermal conductivity. Phonons are scattered at the surface/interfaces of these nanostructures, which results in a dramatic decrease of the thermal conductivity [29, 31, 32, 35]. In 3D materials, grain boundary scattering reduces the thermal conductivity. Grain boundary scattering is higher when the grain size is smaller. Figure 1-7 represents experimental thermal conductivity of a nanograin materials in comparison with the same composite having micron size grains. Consequently, the calculated lattice thermal conductivity of nano grain sample is lower (black line in Figure 1-7) [36].

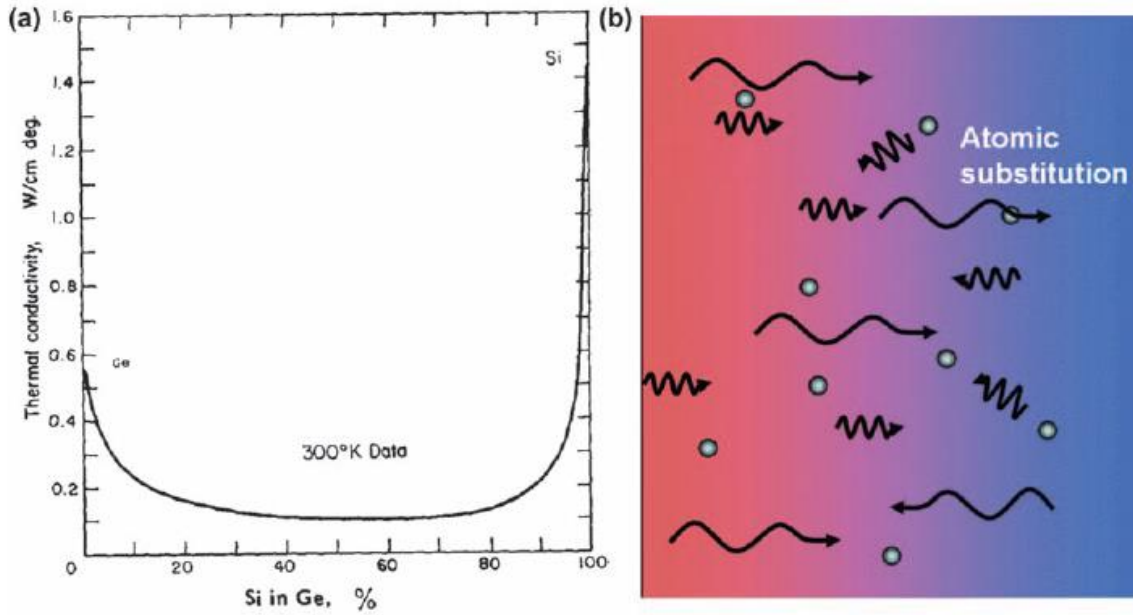


Figure 1-6. (a) Reduction of thermal conductivity of an Si_xGe_{1-x} alloy as a function of Si content in Ge.

(b) Schematic illustration of alloy scattering. short-wavelength phonons are scattered by atomic substitutions [13].

1-3-4-4. Nanosized Defect Scattering

Atomic substitutions like alloy atoms in the matrix can scatter short-wavelength phonons very well, but they are not able to scatter mid- to long-wavelength phonons due to their small sizes [13, 37, 38]. However, mid- and long-wavelength phonons can be scattered very well by nanosize defects embedded inside the host material. Figure 1-8 (a) demonstrates the phonon scattering mechanism by nanoparticles to reduce the thermal conductivity.

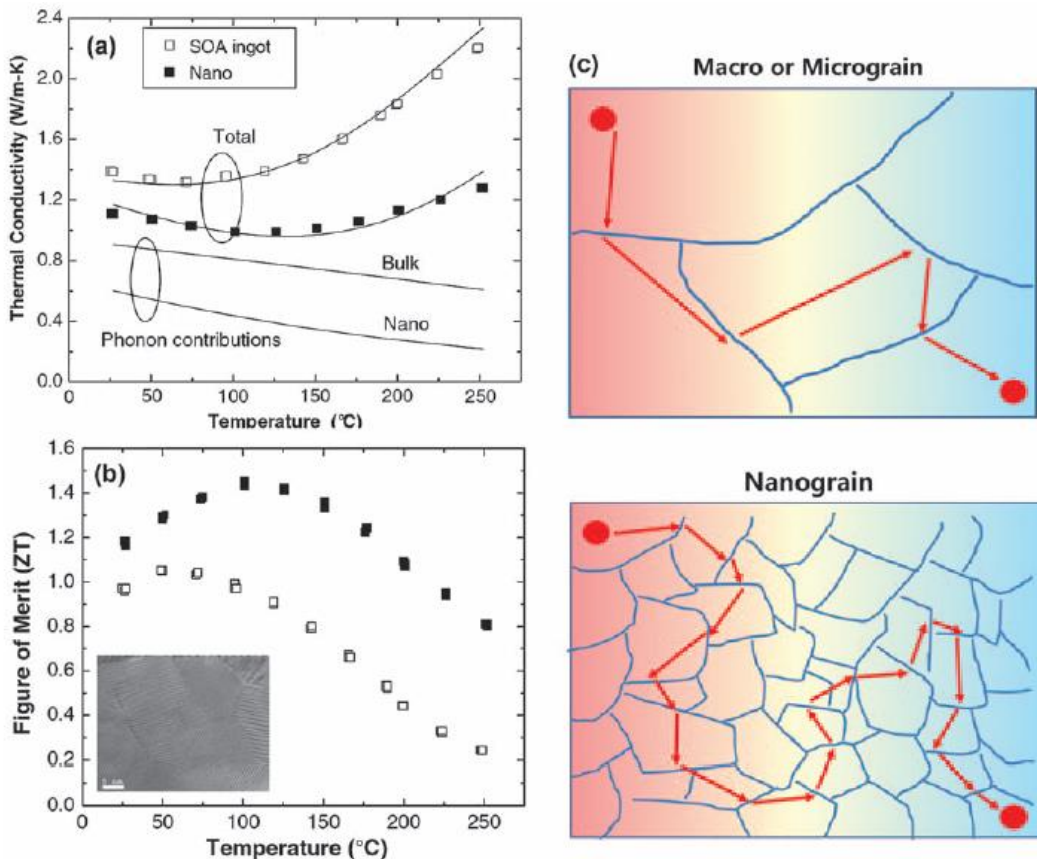


Figure 1-7. (a) Comparison of thermal conductivities of micrograined and nanograined alloys. Solid lines are calculated phonon contributions of bulk and nanograin samples. (b) Figures of merit for micrograined and nanograined alloys [36]. (c) illustration of phonon grain boundary scattering in micrograins and nanograins samples [13].

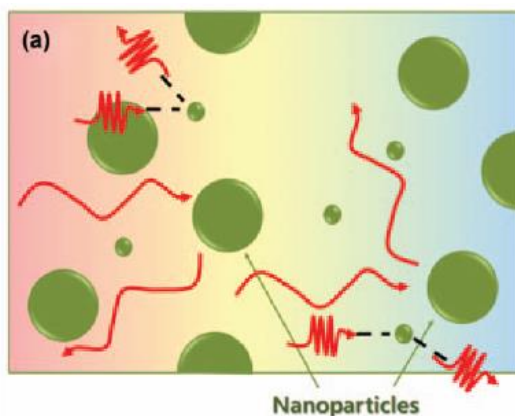


Figure 1-8. Schematic of thermal conductivity reduction by nanoparticle scattering [13].

Chapter 1. Part B. Some experimental and characterization methods

1-4. Sample preparation

Solid state synthesis approach has been used to prepare $\text{Co}_4\text{Ge}_6\text{Te}_6$ Skutterudite and SnTe samples. For $\text{Co}_4\text{Ge}_6\text{Te}_6$ Skutterudite samples, an appropriate amount of Co and Ge were reacted initially using arc melting method and then, Te lumps as well as other additives were added to the GeTe mixture according to the desired stoichiometric ratios of each specimen and hand-grinded using mortar and pestle. The mixture of precursors was cold pressed and loaded into silica ampoules. The silica tubes were closed, transferred to a vacuum line, evacuated, and sealed by using an oxygen/natural gas torch. The furnaces used were profiled to have accurate annealing temperatures. The mixture was initially heated for 10 hrs at 450 °C followed by a period of 4 days at 610 °C. The tubes were cooled down naturally and opened in the air. The solid products were hand ground and cold pressed again in the air before second annealing in an evacuated silica tube at 610 °C for 4 days. The annealing process was repeated one more times in order to produce samples as pure as possible (Figure 1-9). For SnTe samples, high-quality polycrystalline ingots of $\text{Sn}_{1-x}\text{A}_x\text{Te}$ ($x = 0-0.05$) were prepared through melting stoichiometric amounts of the starting elements in vacuum sealed silica tubes (10^{-3} Torr, 10 mm in diameter). The samples were slowly heated to 1000 °C over 10 h, then soaked for 6 h, and then rapidly quenched in the ice-water mixture. The ingots were then hand ground in an agate mortar to obtain fine powders for the sintering step.

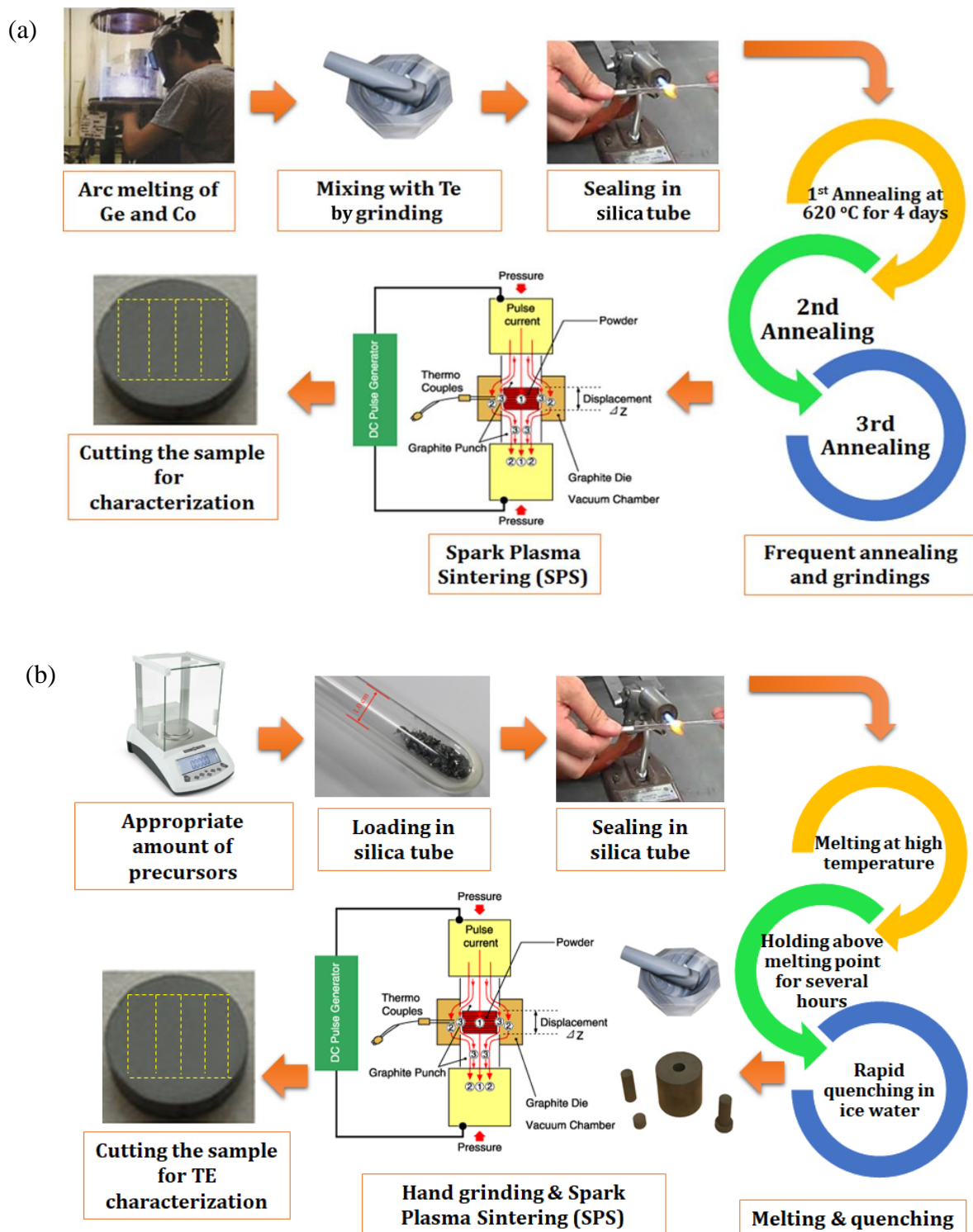


Figure 1-9. Schematic diagram of the sample preparation process and sintering of (a) $\text{Co}_4\text{Ge}_6\text{Te}_6$ and (b) SnTe .

Densification of all the specimens was accomplished by spark plasma sintering (SPS) technique using appropriate temperature, time and pressure under vacuum. The densities of the specimens were measured by both dimensional and Archimedes' methods. Consequently, densities higher than 95% of the theoretical values were acquired for all samples. After sintering, the samples were cut into pellets and bars with a low speed saw for thermoelectric measurements. The sample preparation processes and sintering are summarised schematically in Figure 1-9. The detailed sample preparation and experimental procedure will be discussed in the next chapters.

1-5. Materials characterization

1-5-1. X-ray Powder Diffraction (XRD)

X-ray powder diffraction (XRD) is a fast analytical technique to acquire information on the lattice parameters (crystallographic structure) and chemical composition (phase identification) of crystalline materials.

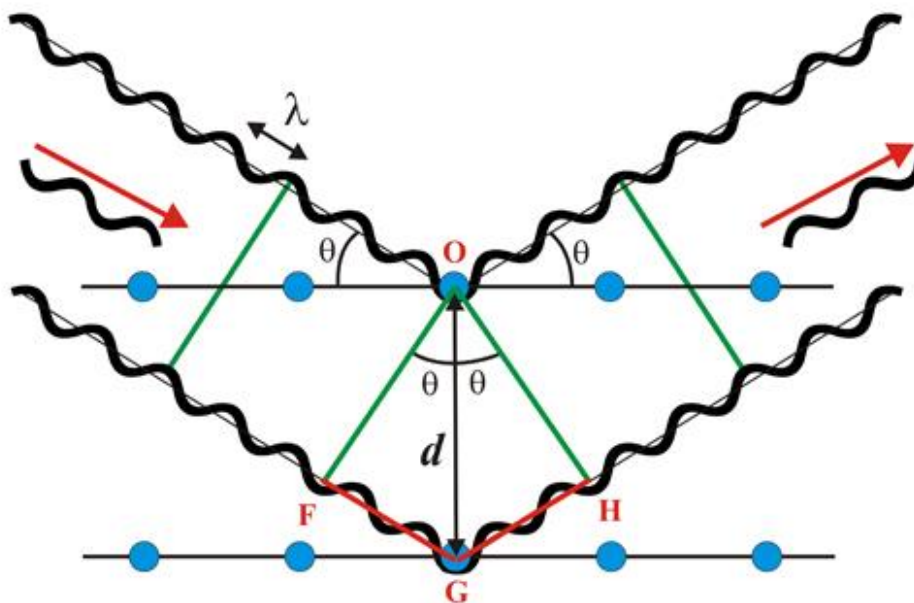


Figure 1-10. illustration of Bragg's law.

In X-ray diffraction, a constructive interference of scattered X-rays occurs. A cathode ray tube generates X-rays, and then X-rays are filtered to produce monochromatic radiation, collimated to concentrate them, and directed toward the sample. The constructive interference happens when the Bragg's law is satisfied (Figure 1-10):

$$n\lambda = 2d\sin\theta \quad (6)$$

where d , θ , n and λ are the spacing between diffracting planes, the incident angle, an integer representing the order of the diffraction peak, and the wavelength of the beam, respectively. Accordingly, the Bragg's law correlates the wavelength of the X-ray radiation to the diffraction angle and lattice spacing in a crystalline sample. These diffracted X-rays are then collected, processed, and counted for phase characterization. Because of the random orientation of the powdered sample, all possible diffraction angles of the lattice should be observed by scanning the sample over a wide range of 2θ angles. Analysis of the diffracted peaks allows identification of the crystalline sample because each mineral possesses a unique set of d -spacings.

In this thesis, the XRD experiments for all the fabricated samples were performed on a PANalytical X'Pert Pro diffractometer with a linear X'Celerator detector and Cu $K\alpha_1$ ($\lambda = 1.5406 \text{ \AA}$) radiation at room temperature. Sample powders were deposited on a zero-background silicon disc. The XRD data were refined by the Rietveld method using the Rietica program [39].

1-5-2. Scanning electron microscopy (SEM)

A focused beam of high-energy electrons is used in the scanning electron microscope (SEM) technique to produce a variety of signals at the surface of solid samples. The signals detected from electron-sample interactions disclose information about morphology (texture), chemical composition, and orientation of the sample. Generally, an area of the sample surface is used to collect data and generate a 2D image that displays sample properties.

When the incident electrons interact with the solid sample, secondary electrons (which produce SEM images), backscattered electrons (BSE), diffracted backscattered electrons (EBSD), photons, visible light, and heat will form. Among these interactions, secondary and backscattered electrons are usually used for imaging purposes.

Secondary electrons are great for displaying the morphology and topography of samples, while the backscattered electrons are beneficial for contrast demonstration of samples with different phases and compositions.

In this thesis, the morphology and structure of fabricated bulk samples were obtained by using a Tescan Vega II LSU (USA) SEM in both secondary and backscatter modes of imaging.

1-5-3. Energy-dispersive X-ray spectroscopy (EDS)

Energy dispersive X-ray spectroscopy (EDS) is an elemental analysis technique that is normally attached to a scanning electron microscopy (SEM), transmission electron microscopy (TEM), or scanning transmission electron microscopy (STEM). EDS is used to attain information on the elemental distributions or chemical composition of a sample. EDS is based on the impact of the electron beam and the sample, which produces X-rays that are characteristic of the elements present in the sample. It is also a very powerful method to examine the elemental composition of individual points or to map out the elemental distribution of the imaged area. When an atom in the sample is sufficiently excited by the incoming electron beam, characteristic X-rays will be emitted in all directions, but they may not escape the sample. The chance for detection and measurement of an X-ray escaping the material depends on its energy, the number of X-rays, and the density of the characterized material. This can reduce the accuracy in inhomogeneous and rough samples. An EDS system has three main parts: (1) the X-ray detector which detects and converts X-rays into electronic signals, (2) the pulse processor, and the analyser which measures the electronic signals

to determine the energy of each X-ray detected, and (3) the analyser which interprets and displays the X-ray data.

1-6. Transport Properties Measurements

1-6-1. Electrical conductivity and Seebeck coefficient measurements

After the SPS process, one sample of each composition was cut into a bar shape for the electrical conductivity and Seebeck coefficient measurements which were conducted simultaneously by means of an ULVAC ZEM-3 instrument. The electrical conductivity is measured using the four-point method, therefore, the voltage drop could be neglected. The measurements were performed under high purity helium atmosphere to prevent oxidation at elevated temperature measurements. During the measurement, the sample was held vertically in between the upper and lower blocks (electrodes). A temperature gradient along the sample length was produced by an electrical resistive heater which is placed in the lower block. Temperatures (T_1 and T_2) and the electric potential differences (dV) across the sample were measured using two thermocouples and two provided channels. Small electric current passes through the sample using the electrodes, and the thermocouple wires measure the voltage difference created by the current in the sample. The sample resistivity is determined at various temperatures from the V-I curve. The Seebeck coefficient is calculated based on the voltage differences of the sample over different temperatures. Therefore, the Seebeck values are determined from the slope of ΔV vs. ΔT plot. A schematic of the electrical conductivity and Seebeck coefficient measurements is given in Figure 1-11.

1-6-2. Thermal conductivity measurements

The laser flash method is used for thermal conductivity measurement which by far is the most practical technique. As shown in Figure 1-11, a thin sample is exposed to a high-intensity short-duration laser. The front surface of the specimen absorbs the energy of the pulsed laser, and as the

result, the temperature of the rear face rises. The thermal diffusivity value is determined using the specimen thickness and the time required for the rear face temperature to increase to a certain percentage of its maximum value. Thermal diffusivity, D , specific heat, C_p , and density, ρ , are required to calculate thermal conductivity as a function of temperature. The following formula shows this relation:

$$\kappa_{\text{total}} = DC_p\rho \quad (8)$$

For adiabatic conditions, D is determined by the following equation:

$$D = 0.1388 \cdot I^2/t_{0.5} \quad (9)$$

where I is the thickness of the test sample in cm, and $t_{0.5}$ is the time at 50% of temperature increase measured at the rear of the specimen in seconds.

In this thesis, the thermal diffusivity data for all fabricated samples was directly measured from room temperature to 600 °C on the Netzsch LFA-457 instrument under vacuum. Square samples with the dimensions of $\sim 10 \times 10$ mm and ~ 1 mm thickness were used for the measurements. The temperature dependent heat capacity, C_p , was derived using a standard sample (pyroceram) in a LFA-457.

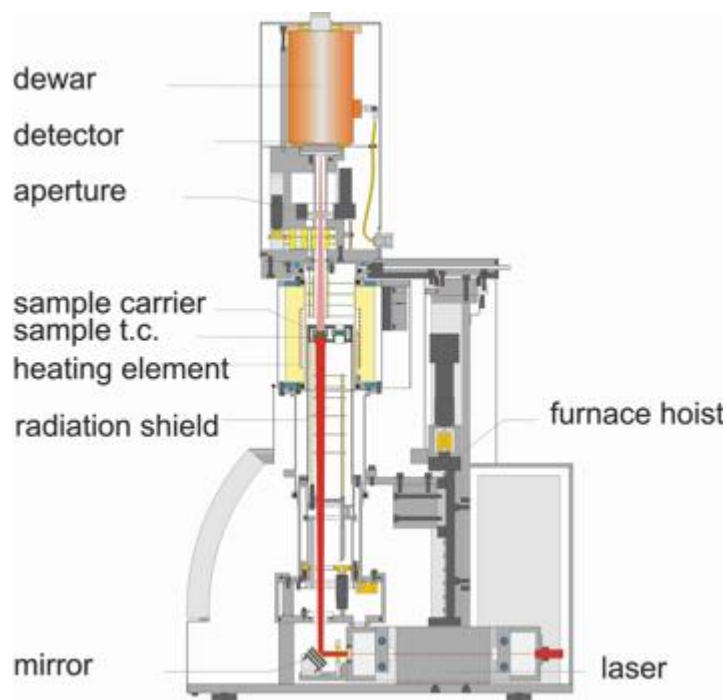
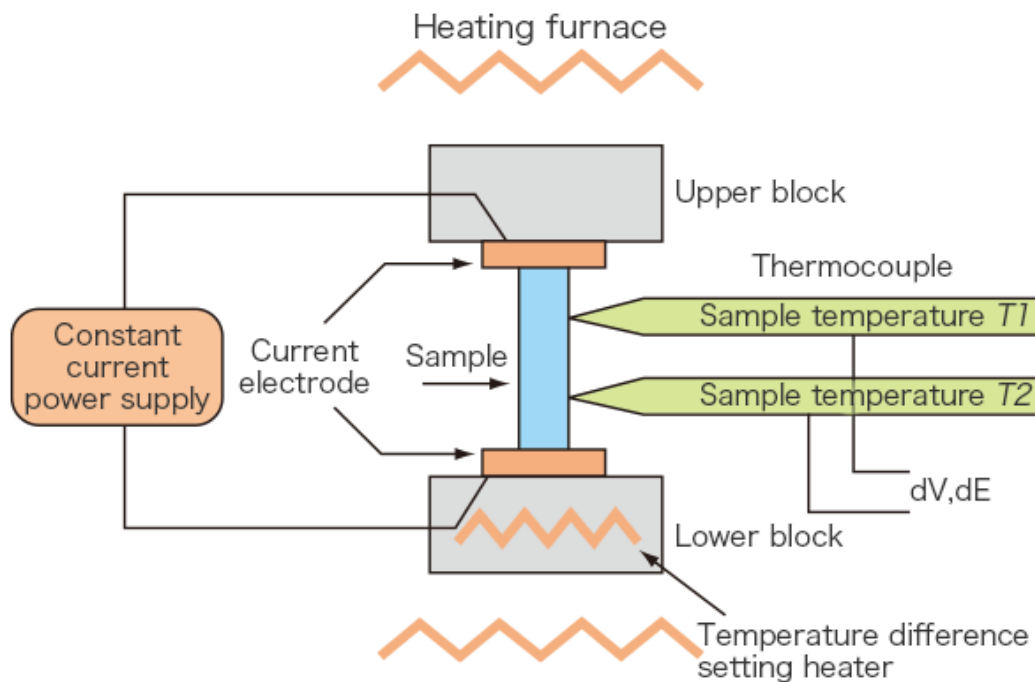


Figure 1-11. a schematic diagram showing (a) electrical conductivity and Seebeck coefficient, (b) thermal conductivity measurements.

1-7. References

- [1] A. Dey, O. P. Bajpai, A. K. Sikder, S. Chattopadhyay, and M. A. S. Khan, "Recent advances in CNT/graphene based thermoelectric polymer nanocomposite: A proficient move towards waste energy harvesting," *Renewable and Sustainable Energy Reviews* 53, vol. 53, pp. 653–671, 2016.
- [2] D. K. Aswal, R. Basu, and A. Singh, "Key issues in development of thermoelectric power generators: High figure-of-merit materials and their highly conducting interfaces with metallic interconnects," *Energy Conversion and Management*, vol. 114, pp. 50–67, 2016.
- [3] X. Zhang and L.-D. Zhao, "Thermoelectric materials: Energy conversion between heat and electricity," *Journal of Materiomics*, vol. 1, pp. 92-105, 2015.
- [4] K. V. Selvana and M. S. M. Ali, "Micro-scale energy harvesting devices: Review of methodological performances in the last decade," *Renewable and Sustainable Energy Reviews*, vol. 54, pp. 1035-1047, 2016.
- [5] D. Champier, "Thermoelectric generators: A review of applications," (in English), *Energy Conversion and Management*, Review vol. 140, pp. 167-181, May 2017.
- [6] A. Shakouri, "Recent Developments in Semiconductor Thermoelectric Physics and Materials," *Annual Review of Materials Research*, Vol 41, vol. 41, pp. 399-431, 2011.
- [7] I. B. Cadoff and E. Miller, *Thermoelectric Materials and Devices*. New York: Reinhold Publishing Corporation, 1960.
- [8] A. Bulusu and D. G. Walker, "Review of electronic transport models for thermoelectric materials," *Superlattices and Microstructures*, vol. 44, no. 1, Jul 2008.
- [9] J. R. Sootsman, D. Y. Chung, and M. G. Kanatzidis, "New and Old Concepts in Thermoelectric Materials," *Angewandte Chemie-International Edition*, vol. 48, no. 46, pp. 8616-8639, 2009.

- [10] G. S. Nolas, D. T. Morelli, and T. M. Tritt, "Skutterudites: A phonon-glass-electron crystal approach to advanced thermoelectric energy conversion applications," *Annual Review of Materials Science*, vol. 29, pp. 89-116, 1999.
- [11] J. C. Zheng, "Recent advances on thermoelectric materials," *Frontiers of Physics in China*, vol. 3, no. 3, pp. 269-279, Sep 2008.
- [12] T. M. Tritt and M. A. Subramanian, "Thermoelectric materials, phenomena, and applications: A bird's eye view," *Mrs Bulletin*, vol. 31, no. 3, pp. 188-194, Mar 2006.
- [13] C. Kang, H. Wang, J.-H. Bahk, H. Kim, and W. Kim, "CHAPTER 6 Thermoelectric Materials and Devices," in *Hierarchical Nanostructures for Energy Devices: The Royal Society of Chemistry*, 2015, pp. 107-141.
- [14] Y. Z. Pei, N. A. Heinz, and G. J. Snyder, "Alloying to increase the band gap for improving thermoelectric properties of Ag₂Te," *Journal of Materials Chemistry*, vol. 21, no. 45, pp. 18256-18260, 2011.
- [15] J. P. Heremans, B. Wiendlocha, and A. M. Chamoire, "Resonant levels in bulk thermoelectric semiconductors," *Energy & Environmental Science*, vol. 5, no. 2, pp. 5510-5530, Feb 2012.
- [16] D. Bilc, S. D. Mahanti, E. Quarez, K. F. Hsu, R. Pcionek, and M. G. Kanatzidis, "Resonant states in the electronic structure of the high performance thermoelectrics AgPbmSbTe_{2+m}: The role of Ag-Sb microstructures," *Physical Review Letters*, vol. 93, no. 14, Oct 2004, Art. no. 146403.
- [17] M. Hong, Z. G. Chen, Y. Z. Pei, L. Yang, and J. Zou, "Limit of zT enhancement in rocksalt structured chalcogenides by band convergence," *Physical Review B*, vol. 94, no. 16, Oct 2016, Art. no. 161201.

- [18] Y. Z. Pei, X. Y. Shi, A. LaLonde, H. Wang, L. D. Chen, and G. J. Snyder, "Convergence of electronic bands for high performance bulk thermoelectrics," (in English), *Nature*, Article vol. 473, no. 7345, pp. 66-69, May 2011.
- [19] L. Yang, Z. G. Chen, M. S. Dargusch, and J. Zou, "High Performance Thermoelectric Materials: Progress and Their Applications," *Advanced Energy Materials*, vol. 8, no. 6, Feb 2018, Art. no. 1701797.
- [20] K. Hoang, S. D. Mahanti, and M. G. Kanatzidis, "Impurity clustering and impurity-induced bands in PbTe-, SnTe-, and GeTe-based bulk thermoelectrics," *Physical Review B*, vol. 81, no. 11, Mar 2010, Art. no. 115106.
- [21] A. J. Minnich, M. S. Dresselhaus, Z. F. Ren, and G. Chen, "Bulk nanostructured thermoelectric materials: current research and future prospects," *Energy & Environmental Science*, vol. 2, no. 5, pp. 466-479, 2009.
- [22] A. P. Goncalves, E. B. Lopes, O. Rouleau, and C. Godart, "Conducting glasses as new potential thermoelectric materials: the Cu-Ge-Te case," *Journal of Materials Chemistry*, vol. 20, no. 8, pp. 1516-1521, 2010.
- [23] A. V. Dmitriev and I. P. Zvyagin, "Current trends in the physics of thermoelectric materials," *Physics-Uspekhi*, vol. 53, no. 8, pp. 789-803, 2010.
- [24] C. L. Wan, Y. F. Wang, N. Wang, and K. Koumoto, "Low-Thermal-Conductivity $(MS)_{1+x}(TiS_2)_2$ (M = Pb, Bi, Sn) Misfit Layer Compounds for Bulk Thermoelectric Materials," *Materials*, vol. 3, no. 4, pp. 2606-2617, Apr 2010.
- [25] A. P. Goncalves *et al.*, "Semiconducting glasses: A new class of thermoelectric materials?," *Journal of Solid State Chemistry*, vol. 193, pp. 26-30, Sep 2012.

- [26] Y. Ma *et al.*, "Enhanced thermoelectric figure-of-merit in p-type nanostructured bismuth antimony tellurium alloys made from elemental chunks," *Nano Letters*, vol. 8, no. 8, pp. 2580-2584, Aug 2008.
- [27] W. Kim, R. Wang, and A. Majumdar, "Nanostructuring expands thermal limits," *Nano Today*, vol. 2, no. 1, pp. 40-47, Feb 2007.
- [28] P. D. Maycock, "Thermal conductivity of silicon, germanium, III–V compounds and III–V alloys," *Solid-State Electronics*, vol. 10, pp. 161-168, 1967.
- [29] W. S. Capinski, H. J. Maris, T. Ruf, M. Cardona, K. Ploog, and D. S. Katzer, "Thermal-conductivity measurements of GaAs/AlAs superlattices using a picosecond optical pump-and-probe technique," *Physical Review B*, vol. 59, no. 12, pp. 8105-8113, Mar 1999.
- [30] D. Y. Li, Y. Y. Wu, P. Kim, L. Shi, P. D. Yang, and A. Majumdar, "Thermal conductivity of individual silicon nanowires," *Applied Physics Letters*, vol. 83, no. 14, pp. 2934-2936, Oct 2003.
- [31] R. Venkatasubramanian, E. Siivola, T. Colpitts, and B. O'Quinn, "Thin-film thermoelectric devices with high room-temperature figures of merit," *Nature*, vol. 413, no. 6856, pp. 597-602, Oct 2001.
- [32] T. C. Harman, P. J. Taylor, M. P. Walsh, and B. E. LaForge, "Quantum dot superlattice thermoelectric materials and devices," *Science*, vol. 297, no. 5590, pp. 2229-2232, Sep 2002.
- [33] A. Majumdar, "Thermoelectricity in semiconductor nanostructures," *Science*, vol. 303, no. 5659, pp. 777-778, Feb 2004.
- [34] M. Law, J. Goldberger, and P. D. Yang, "Semiconductor nanowires and nanotubes," *Annual Review of Materials Research*, vol. 34, pp. 83-122, 2004.

- [35] A. I. Boukai, Y. Bunimovich, J. Tahir-Kheli, J. K. Yu, W. A. Goddard, and J. R. Heath, "Silicon nanowires as efficient thermoelectric materials," *Nature*, vol. 451, no. 7175, pp. 168-171, Jan 2008.
- [36] B. Poudel *et al.*, "High-thermoelectric performance of nanostructured bismuth antimony telluride bulk alloys," *Science*, vol. 320, no. 5876, pp. 634-638, May 2008.
- [37] W. Kim and A. Majumdar, "Phonon scattering cross section of polydispersed spherical nanoparticles," *Journal of Applied Physics*, vol. 99, no. 8, Apr 2006, Art. no. 084306.
- [38] W. Kim *et al.*, "Thermal conductivity reduction and thermoelectric figure of merit increase by embedding nanoparticles in crystalline semiconductors," *Physical Review Letters*, vol. 96, no. 4, Feb 2006, Art. no. 045901.
- [39] B. A. Hunter and C. J. Howard, *Rietica*. Menai, Australia: Australian Nuclear Science and Technology Organization, 2000.

Chapter 2- Effect of Spark Plasma Sintering and Sb Doping on the Thermoelectric Properties of $\text{Co}_4\text{Ge}_6\text{Te}_6$ Skutterudite

2-1. Abstract

For high-performance thermoelectric material, spark plasma sintering (SPS) has been widely used to manufacture specimens in a very short period compared to other sintering techniques. However, the microstructural evolution, phase stability and compositional homogeneity of thermoelectric materials under SPS conditions has been rarely investigated. In this work, we studied the effect of SPS on microstructure, phase homogeneity and thermoelectric properties of a ternary $\text{Co}_4\text{Ge}_6\text{Te}_6$ skutterudite as a model system. Phase homogeneity of the spark plasma sintered $\text{Co}_4\text{Ge}_6\text{Te}_6$ pellets has been investigated by XRD diffraction and EDX elemental analysis. Significant variations in the physical properties reflect the presence of different crystalline phases due to the current-driven migration of mobile species inside the samples. Furthermore, small amounts of Sb, added to investigate the role of dopants on the physical properties, yielded the highest power factor for the $\text{Co}_4\text{Ge}_6\text{Te}_6$ -based compounds.

2-2. Introduction

The global energy demand is constantly increasing due to the industrial and domestic usage. While renewable energy technologies are poised to meet some of that energy demand, currently only 10% of the energy is generated by green sources such as solar, wind and hydropower; the rest is obtained from fossil fuel combustion with an efficiency of 30-40%. In other words, more than half of the energy is lost as waste heat, which has a detrimental impact on economy and environment. Therefore, it is imperative to retrieve some of the waste heat and enhance the efficiency of energy production. Development of thermoelectric (TE) generators can play a vital role, as they can scavenge the waste heat and convert it into electricity [1-3].

Thermoelectric modules consist of p-n semiconductor pairs, which are thermally in parallel but electrically in series in order to let electrons and holes move in the same direction pulling heat from the hot end to the colder one [1]. In addition to being environmentally friendly, thermoelectric modules offer other benefits such as reliability and mechanical rigidity (no moving parts), simple configuration, scalability, and absence of noise. They can be potentially used in different areas from small- to large-scale waste heat recovery systems, e.g. in automobiles, steel mills, cement plants. [2, 4]. However, TE devices have low overall efficiency compare to other technologies, which limits their use.

The performance of thermoelectric materials is defined by the “figure of merit” term, $zT = S^2\sigma T/\kappa$, where S is Seebeck coefficient, σ the electrical conductivity, κ the thermal conductivity, T , the absolute temperature; $S^2\sigma$ is called power factor [2, 3]. Very high zT values would allow approaching the Carnot efficiency, which is determined only by absolute temperatures. However, this is not achievable due to the low performances of available thermoelectric materials. Still, zT enhancement is a primary focus in thermoelectric research and it is accomplished through optimization of three primary TE properties (σ , S and κ) [2, 3]. The high-performance TE materials need to have both high S and σ , but this poses a challenge due to the competition between Seebeck coefficient and electrical conductivity. Additionally, thermal conductivity (κ) has to be low, but it can be difficult to minimize it since it has both lattice, κ_l , and electronic, κ_e , contributions, with the latter being proportional to the electrical conductivity.

Recently, researchers step up their efforts to find suitable thermoelectric materials with improved properties. Different phenomena, such as band convergence to optimize the electrical conductivity or Seebeck coefficient, hierarchical structures to reduce the thermal conductivity through phonon scattering, have been used. In addition, some materials with intrinsically low thermal conductivity

have been developed for TE applications [1-3]. Although the outcomes achieved are very promising compared to a decade ago, more efficient materials are required. To date, the highest zT value is around 2.5 for p-type semiconductors (e.g. PbTe–SrTe) and around 2 for n-type semiconductors (e.g. AgPb_mSbTe_{2+m} (LAST)) [2, 3].

Skutterudites are one of the promising TE compounds with the general composition of MX₃ (M: transition metals, such as Co, Fe, Rh or Ir. X: pnictogen atoms, such as P, As or Sb). They crystallise in a complex body-centred structure with the space group $Im\bar{3}$, and can be described as an infinite array of distorted and tilted octahedra, with each octahedron sharing corners with six neighbouring octahedra. Skutterudites structure can also be considered as a derivative of the ReO₃ structure. In other words, severe distortion of the anion sublattice in the ReO₃ structure (by tilting of octahedra) leads to the skutterudite structure. In this regard, four anions which are located at the edges of the ReO₃ unit cell move towards the center of the unit cell and create the characteristic four-member X₄ rings of the skutterudite structure [5]. In the resulted new body-centred unit cell with space group $Im\bar{3}$, cations are placed in the octahedral coordination, while anions are coordinated by two cations and two anions. Another consequence of this specific configuration is that the linkage of octahedra generates a void at the centre of [MX₆]₈ octahedral-cluster and this void could be filled by different elements [6]. Hence, filled skutterudites (A_yM₄X₁₂, A is the filling element) are obtained by fully filling or partially filling the voids. This promisingly affects the thermoelectric properties, specifically the thermal conductivity [7].

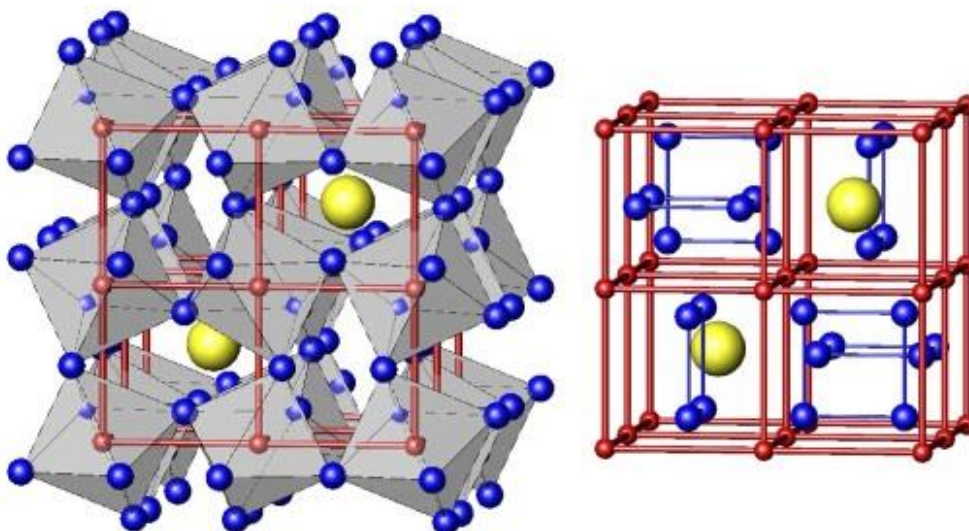


Figure 2-1. Crystal structure of skutterudite (CoSb₃). The Co and Sb atoms are represented by red and blue balls, respectively. Filler atoms are shown by big yellow balls.

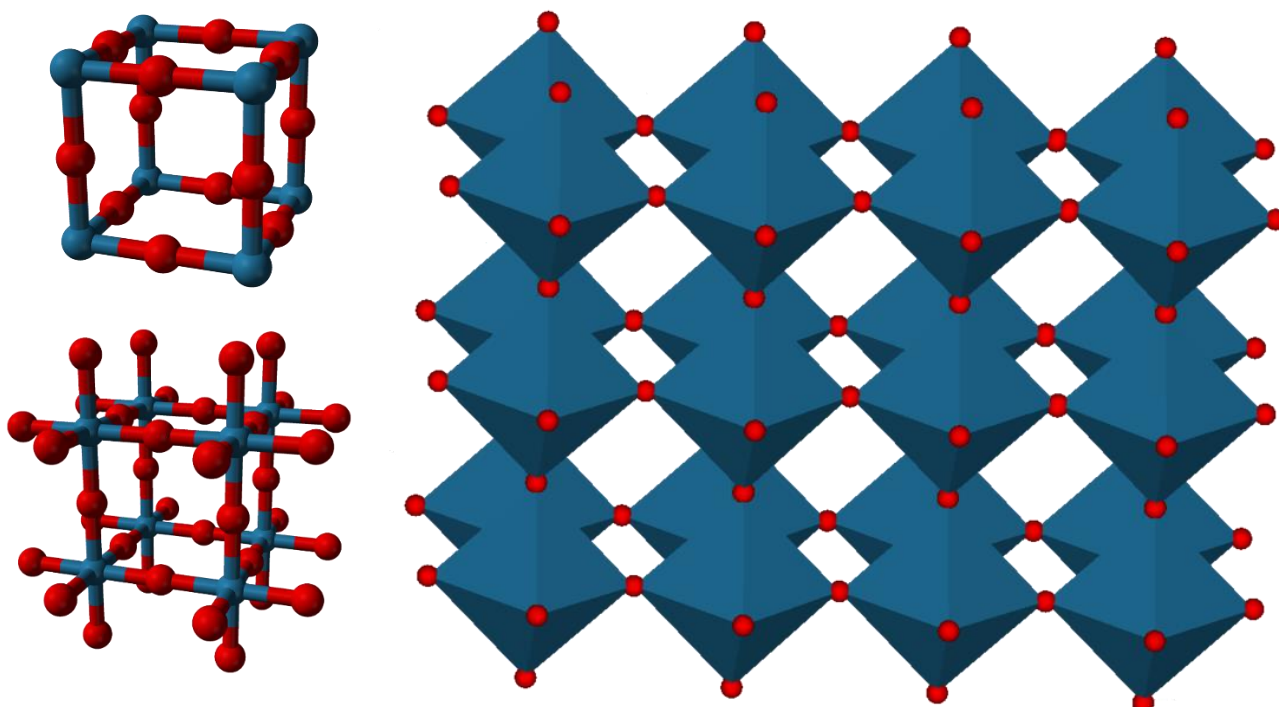


Figure 2-2. ReO₃ crystal structure and octahedral network. Re is in blue and oxygen is in red colour.

Good electrical conductivity stemming from the high electron mobility makes binary skutterudites promising candidates for thermoelectric applications. However, high lattice thermal conductivity limits their thermoelectric performance. In order to reduce the lattice thermal conductivity, voids in skutterudites are partially or fully filled with different atoms (Figure 2-1), including alkali and alkaline earth metals, rare earth, and transition elements, which leads to significant phonon scattering and velocity reduction [8-11]. Filled $\text{Co}_4\text{Sb}_{12}$ skutterudite displays favourable thermoelectric properties and is already used for thermoelectric power generation.

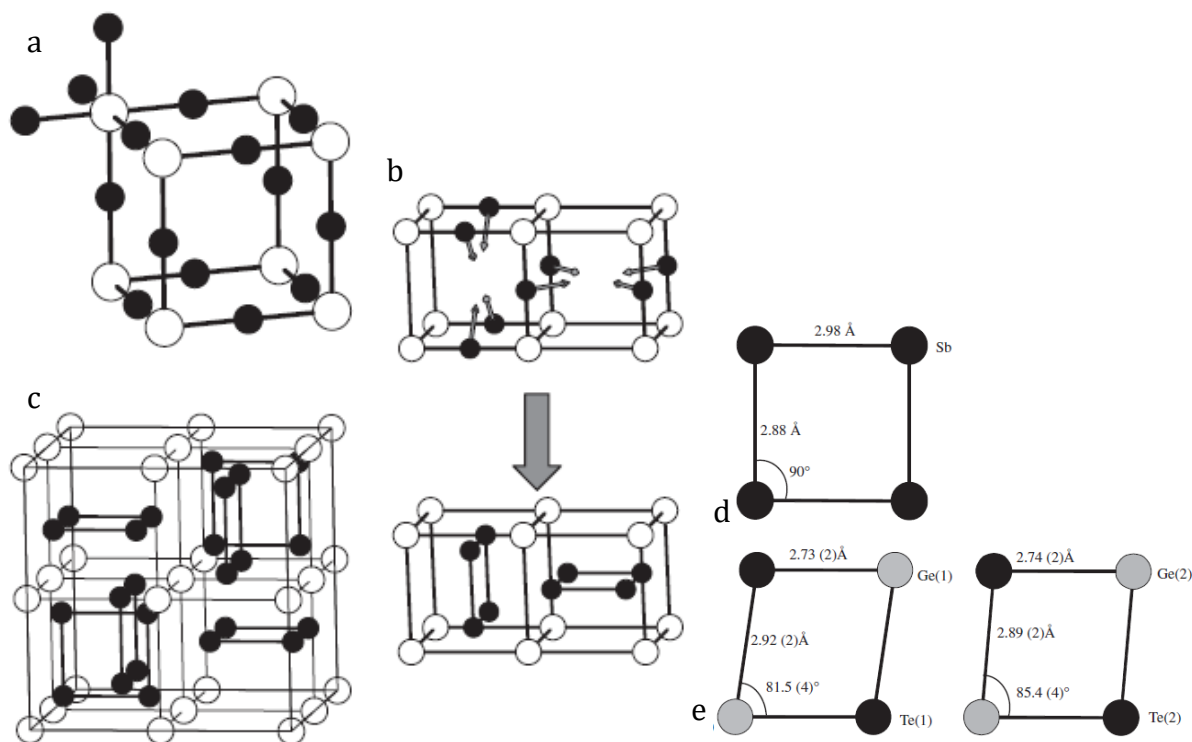


Figure 2-3. (a) the octahedral coordination of one of the metal atoms in the ReO_3 structure, (b) the distortion of the anion sublattice in the ReO_3 structure which results in the skutterudite structure, and (c) the skutterudite structure, with its characteristic anion rings [5]. Metal atoms and anions are represented by open and black circles, respectively. (d) The four-membered rings in CoSb_3 and (e) $\text{CoGe}_{1.5}\text{Te}_{1.5}$ [17].

Ternary skutterudites isoelectronic with binary skutterudites can be formed either by anionic substitution with an equimolar mixture of the 14 and 16 group elements or by isoelectronic substitution at the cation site by a pair of the 8 and 10 group metals. In binary skutterudites all the M–X distances are identical (but the X–M–X angles deviate from 90), and only one crystallographically distinct, rectangular X₄ ring with short and long X–X distances is created. However, in the ternary CoX_{1.5}Y_{1.5} skutterudites, two crystallographically distinct four-member [X₂Y₂] rings are formed (Figure 2-3 (d-e)), in which the X and Y atoms are trans to each other. This stems from the presence of more distorted octahedra in the ternary skutterudites. The X–Y–X angles are greater than 90 and the four-membered rings are diamond-like instead of rectangular. Crystallographic studies on ternary skutterudites concluded that the anions are ordered (rather than being randomly distributed) in the layers perpendicular to the [111] direction of the skutterudite unit cell [12-17]. This ordering is accompanying by distortion of the anion rings, causing the symmetry reduction from cubic to rhombohedral ($Im\bar{3} \rightarrow R\bar{3}$). High-temperature order-disorder transitions and reverse symmetry increase ($R\bar{3} \rightarrow Im\bar{3}$) have been reported in CoGe_{1.5}Te_{1.5} (Figure 2-4), but its impact on the transport properties is not documented yet [18].

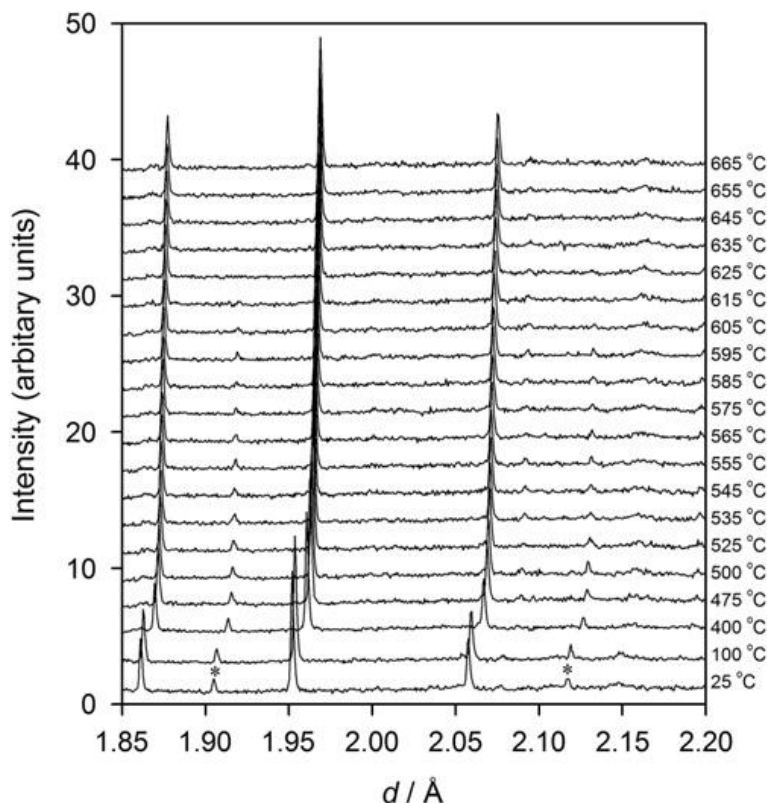


Figure 2-4. Powder neutron diffraction data at different temperature for $\text{CoGe}_{1.5}\text{Te}_{1.5}$ showing the disappearance of the superstructure reflections (labelled with *) during the phase transition [18].

Physical properties of some ternary skutterudites have been previously investigated (Table 2-1). Compared with binary skutterudites, high Seebeck coefficients and low electrical conductivities were observed owing to larger effective masses. For example, first principles calculations of the electronic band structure and vibrational spectra of $\text{CoGe}_{1.5}\text{Te}_{1.5}$ and $\text{CoSn}_{1.5}\text{Te}_{1.5}$ showed that these materials have a multivalley band with heavy electrons and larger band gaps yielding large S and electrical resistivity values compared to the binary analogues [19]. The large complexity of the unit cell leads to lattice thermal conductivities lower than that of CoSb_3 , and further κ_l reductions can be achieved with fillers [7]. It was calculated that point-defect scattering is 5 times larger for the partially Ce- and Yb-filled phases than for the unfilled $\text{CoGe}_{1.5}\text{Se}_{1.5}$, indicating a

strong phonon scattering attributable to the disorder on the filled site [20]. However, high zT values have not yet been achieved with ternary skutterudites (Table 2-1).

Table 2-1. Thermoelectric properties of some ternary skutterudite compounds.

Material	σ_{\max} ($S.cm^{-1}$)		S_{\max} ($\mu V.K^{-1}$)		K_{\min} ($W.m^{-1}.K^{-2}$)		PF_{\max} ($\mu W.cm^{-1}.K^{-2}$)		zT_{\max}		Ref
	Value	T	Value	T	Value	T	Value	T	Value	T	
	(~)	(K)	(~)	(K)	(~)	(K)	(~)	(K)	(~)	(K)	
CoSn _{1.5} Te _{1.5}	80	900	-210	613	2	678	1.5	900	0.06	823	[21]
RhSn _{1.5} Te _{1.5}	730	500	160	783	2.18	873	10	873	0.35	803	[21]
IrSn _{1.5} Te _{1.5}	212	623	240	973	1.55	973	6	623	0.33	1000	[21]
CoGe _{1.452} Se _{1.379}	1.5	400	-590	180	---	---	0.16	300	---	---	[20]
Ce _{0.13} Co ₄ Ge ₆ Se ₆	9.5	293	-330	303	---	---	1	293	---	---	[22]
Yb _{0.14} Co ₄ Ge ₆ Se ₆	50	293	-170	303	---	---	1.35	293	---	---	[22]
CoGe _{1.5} Te _{1.5}	52	773	-380	423	2.25	673	2.15	585	0.051	673	[18]
CoSn _{1.5} Se _{1.5}	250	310	250	603	2.2	723	6.3	443	0.106	577	[6]
Co _{3.6} Ru _{0.2} Sn ₆ Se ₆	385	300	50	633	1.95	550	0.6	558	0.016	610	[13]
Co _{3.8} Ni _{0.2} Sn ₆ Se ₆	270	690	-145	623	1.8	550	5.5	688	0.18	700	[13]
CoSn _{1.5} Te _{1.5}	130	930	-460	420	2.5	620	1.5	523	---	---	[23]
Co _{0.95} Ni _{0.05} Sn _{1.5} Te _{1.5}	335	930	-240	720	---	---	7.9	718	---	---	[23]
Co _{0.95} Ru _{0.05} Sn _{1.5} Te _{1.5}	175	930	90	550	---	---	0.65	918	---	---	[23]
RhGe _{1.5} S _{1.5}	1.96	348	120	348	---	---	0.027	348	---	---	[15]
CoGe _{1.5} S _{1.5}	0.072	373	210	373	1.23	773	0.003	373	---	---	[15]
CoGe _{1.5} Te _{1.5}	0.25	288	-800	135	1.12	698	0.12	288	---	---	[15]
IrGe _{1.5} Te _{1.5}	0.15	303	240	303	---	---	0.01	303	---	---	[15]
CoSn _{1.5} Te _{1.5}	0.37	350	-380	373	0.65- 0.75	300- 800	0.05	350	---	---	[15]
IrSn _{1.5} Te _{1.5}	5.5	350	125	335	---	---	0.075	350	---	---	[15]
RuSb ₂ Te	345	333	160	528	---	---	7.5	520	0.09	673	[24]
Ru _{0.95} Fe _{0.05} Sb ₂ Te	325	203	165	690	---	---	5.5	680	0.15	673	[24]
RuSb ₂ Sn _{0.1} Te _{0.9}	396	273	105	690	---	---	3.5	680	0.128	673	[24]
Yb _{0.05} RuSb ₂ Te	285	353	150	550	---	---	5.75	578	0.147	673	[24]
Co ₄ Ge _{5.8} Sb _{0.4} Te _{5.8}	470	373	-180	773	---	---	12	773	---	---	This work

Zevalkink et al [21] has recently reported on n-type CoSn_{1.5}Te_{1.5}, p-type IrSn_{1.5}Te_{1.5} and RhSn_{1.5}Te_{1.5} skutterudites. Powder X-ray diffraction patterns and Rietveld refinements revealed

the supercell reflections, resulting from the ordering of Sn and Te in the square rings in all three compounds. Moreover, low thermal conductivity, relatively large band gaps, and band structure features similar to those in binary skutterudites resulted in zT values of up to 0.06, 0.33 and 0.35 for $\text{CoSn}_{1.5}\text{Te}_{1.5}$, $\text{IrSn}_{1.5}\text{Te}_{1.5}$ and $\text{RhSn}_{1.5}\text{Te}_{1.5}$, respectively. Furthermore, the effects of cation doping on the thermoelectric properties of $\text{Co}_4\text{Sn}_6\text{Se}_6$ was studied through the substitution of transition metals (Ni, Ru) at Co site [13]. It was demonstrated that the Ru atoms behave as acceptors, while Ni atoms acted as electron donors. In comparison with $\text{Co}_4\text{Sb}_{12}$ binary skutterudite, the thermal conductivity has been reduced in both the pristine and transition metals doped $\text{Co}_4\text{Sn}_6\text{Se}_6$ samples. The maximum zT of 0.18 at 700 K was achieved for the $\text{Co}_{3.8}\text{Ni}_{0.2}\text{Sn}_6\text{Se}_6$ compound. Theoretical and experimental studies suggested that TE properties of the ternary skutterudites can be further optimized through doping or filling with other elements, such as alkaline-earth metals [25].

Although, both the structure and composition have vital effects on TE properties, the sample preparation process, such as heat treatment and sintering procedure, will impact TE properties as well. TE devices are made of p- and n-type semiconductor legs having regular well-defined shape. These legs mostly consist of polycrystalline powders that were compacted into a dense bulk specimen. Likewise, physical property measurements usually require bulk materials with regular shapes, which can be obtained by hot densification of powders followed by cutting them into appropriate sizes. The most widely used densification methods are hot pressing (HP) and spark plasma sintering (SPS). During HP, a sample is heated by an external heat source, while during SPS heat is generated internally by large, pulsed direct current passing through the graphite die and powder sample. An advantage of the SPS technique is a very fast heating rate, up to 1000 K/min, which significantly decreases the sintering time. Short heating times can prevent phase

separation and suppress grain growth. Additionally, simultaneous application of electrical current and high pressure allows decreasing the compaction temperature. As a result, SPS yields smaller grains when starting from fine or nano-crystalline powder and, thus, permits to lower the sample lattice thermal conductivity due to increased phonon scattering at the grain boundaries [26]. However, the SPS densification mechanisms are still not fully understood and several mechanisms, such as local melting and evaporation, surface activation on particles, and field-assisted diffusion, etc. have been suggested, etc. [26-30].

Unfortunately, SPS can also have detrimental effects on the sample; a strong electrical current can lead to compositional inhomogeneity and phase decomposition. For examples, Zn_4Sb_3 decomposes into ZnSb, Zn, and Sb when densified by SPS [31-33]. Yin et. al. [31] studied the phase distribution of spark plasma sintered thermoelectric Zn_4Sb_3 samples by Seebeck microprobe scanning and spatially resolved X-ray diffraction. They observed severe variations in the Seebeck coefficient due to the presence of ZnSb phase at the bottom of the pellet and metallic Zn impurity at the top. Indeed, highly mobilized Zn atoms migrate under the applied current, resulting in the phase non-uniformity throughout the sample. Zn_4Sb_3 is not the only material showing instability under SPS and other systems with complex structure and/or high mobility species will display similar problems. Additionally, the Peltier heating and cooling occurs at the sample-die interfaces when direct current passes through the sample during SPS, generating a temperature difference between the two ends of the sample and consequently a density gradient within the sample. The better the TE performance of the sintered sample, the larger the temperature gradient. The Peltier effect is a persistent issue for direct current SPS systems and it may affect the sample's composition and its TE performance [34].

Based on the abovementioned facts, we decided to explore the effects of the spark plasma sintering on the microstructural homogeneity and TE properties of the $\text{Co}_4\text{Ge}_6\text{Te}_6$ (CGT) samples. Additionally, we aimed to optimize TE performance of ternary skutterudites for intermediate temperature applications. We have observed that electrical current in SPS causes decomposition of the CGT materials and has a detrimental effect on their transport properties. Introduction of an insulator layer stopped the direct flow of the current through the CGT sample and allowed us to obtain high-quality samples. Moreover, antimony (Sb) doping was found to yield the highest power factor reported for the CGT-based compounds.

2-3. Experimental procedure

In the present study, all the skutterudite samples were prepared by solid-state reaction of the elements. Co (99.999 wt. %), Ge (99.995 wt.%), Sb (99.995 wt.%), and tellurium (99.999 wt.%) pieces were used for the syntheses without further purification. Samples with different Ge/Te ratios were prepared by altering the Ge amount while keeping the Te amount constant to explore the effect of different Ge/Te ratios. In addition, anion co-substitutions were fulfilled by replacing both Ge and Te anions with Sb.

An appropriate amount of Co and Ge were initially reacted using arc melting method. Then, Te lumps as well as other additives were added to the CoGe mixture according to the desired stoichiometric ratios of each specimen and hand-grinded using mortar and pestle. The mixture was cold pressed and loaded into silica ampoules (10 mm in diameter). The silica tubes were closed, transferred to a vacuum line, evacuated, and sealed (10^{-3} Torr) by using an oxygen/natural gas torch. The furnaces used for annealing the samples were profiled to assure the temperature accuracy. The annealing temperatures are summarized in Table 2-2.

The samples were initially heated for 10 hrs at 450 °C followed by a period of 4 days at 610 °C. The tubes samples cooled down naturally and opened in the air. The solid products were hand ground and cold pressed again in the air before second annealing in an evacuated silica tubes at 610 °C for 4 days. The annealing process was repeated one more times in order to obtain pure samples.

Table 2-2. Sample preparation parameters during synthesis, annealing and sintering.

procedure	Temperature (°C)		Time	condition
	a	b		
Solid state reaction + 1 st annealing	450	610	4 days	vacuum
2 nd annealing		610	4 days	vacuum
3 rd annealing		610	4 days	vacuum
SPS		500-610	10 – 60 min	vacuum

Dense polycrystalline pellets with a thickness of 3-4 mm were prepared by SPS compaction. During the pressing, a heating rate of 100 K/min to a maximum temperature from 500 to 610 °C and holding time of 10-60 min under vacuum were applied to the samples. The samples were compacted in a graphite die with a diameter of 15 mm under a pressure of 45 MPa. Inside the press, the CGT powder was sandwiched between two pieces of 0.15 mm thick graphite foils. The graphite foil was added for good electrical and thermal contacts between punches and powder. The pellet was cut in appropriate size to investigate the physical properties and microstructure. The densities of the specimens were measured by determining their dimension and mass. Consequently, densities higher than 95% of the theoretical values were acquired for all samples. X-ray diffraction (XRD) and energy dispersive spectroscopy (EDX) were employed to characterize the samples' crystallinity, homogeneity, chemical composition and elemental distributions. Powder XRD data were collected for $2\theta = 10-80^\circ$ with a PANalytical X'Pert Pro

diffractometer with a linear X'Celerator detector using Cu-K α_1 ($\lambda = 1.5406 \text{ \AA}$) radiation at room temperature. To minimise background intensity, powders were placed on a flat-low background silicon disc. The XRD data were examined by the Rietveld method using the Rietica program [35]. In addition, the X-ray diffraction pattern of bulk samples were collected using the Bruker D8 DISCOVER, DAVINCI.DESIGN diffractometer, equipped with a Co sealed tube source ($\lambda_{\text{avg}} = 1.79026 \text{ \AA}$). Microstructural analysis was done using scanning electron microscopy (SEM, Tescan Vega II LSU, USA) in both secondary and backscatter modes of imaging. The samples were prepared by hand polishing using 2400 SiC and 4000 SiC polishing papers. Sample composition and elemental distribution were determined via energy-dispersive X-ray analysis (EDX).

After densification, polycrystalline bulk specimens were cut into $2 \times 2 \times 10 \text{ mm}^3$ parallelepipeds for high-temperature transport properties measurements (σ , S). The surface of each specimen was gently polished using 2400 SiC and 4000 SiC polishing papers. Simultaneous data collection of the Seebeck coefficient and electrical resistivity was accomplished under a He atmosphere from room temperature to 500°C on a ULVAC-RIKO ZEM-3 instrument system.

2-4. Results and discussions

The powder X-ray diffraction data for the stoichiometric $\text{Co}_4\text{Ge}_6\text{Te}_6$ sample after sequential annealing are shown in Figure 2-5 (a). The X-ray diffraction results of the first and second annealing steps demonstrate the presence of tiny amounts of other phases (GeTe and CoTe_2), while the third annealing step yields a pure sample, which can be indexed based on the cubic unit cell of archetypal skutterudite compounds. Initial refinement with the CoSb_3 skutterudite structure as a starting model (space group $\text{Im}\bar{3}$, $a = 8.7224(4) \text{ \AA}$) lead to acceptable values of agreement factors; however, relatively weak superstructure diffractions could not be fitted by this cubic model. Comparable results were reported for $\text{CoSn}_{1.5}\text{Se}_{1.5}$, $\text{CoSn}_{1.5}\text{Te}_{1.5}$ and $\text{IrSn}_{1.5}\text{Te}_{1.5}$ [12, 15, 36]. As

was previously shown [17, 18], the ordering among Ge and Te atoms leads to the $Im\bar{3}$ to $R\bar{3}$ symmetry lowering and appearance of the superstructure reflections. Accordingly, the Rietveld refinement based on the space group $R\bar{3}$ converged to lower agreement factors, and all reflections were fitted by this anion ordered structure model (Figure 2-5 (b)).

A lower symmetry introduces two independent anion sites into each four-atom anion ring. Refinement of site occupancy factors for the anion positions, with the constraint, that each site remains fully occupied and that the overall stoichiometry is maintained, discloses that the Ge and Te anions are nearly fully ordered over the anion rings at room temperature. A representative refinement profile is shown in Figure 2-5 (b). ~6% of Ge atoms are located in Te sites; this is in good agreement with the previous neutron diffraction study on $CoGe_{1.5}Te_{1.5}$ [18]. Ordering in $CoGe_{1.5}Te_{1.5}$ is somewhat lower than in $CoGe_{1.5}S_{1.5}$ and $CoGe_{1.5}Se_{1.5}$, which suggests that ordering decreases for larger anions [16, 18]. In addition, slight displacement of the Co (1) atom from the ideal $(0, 0, \frac{1}{4})$ position is observed.

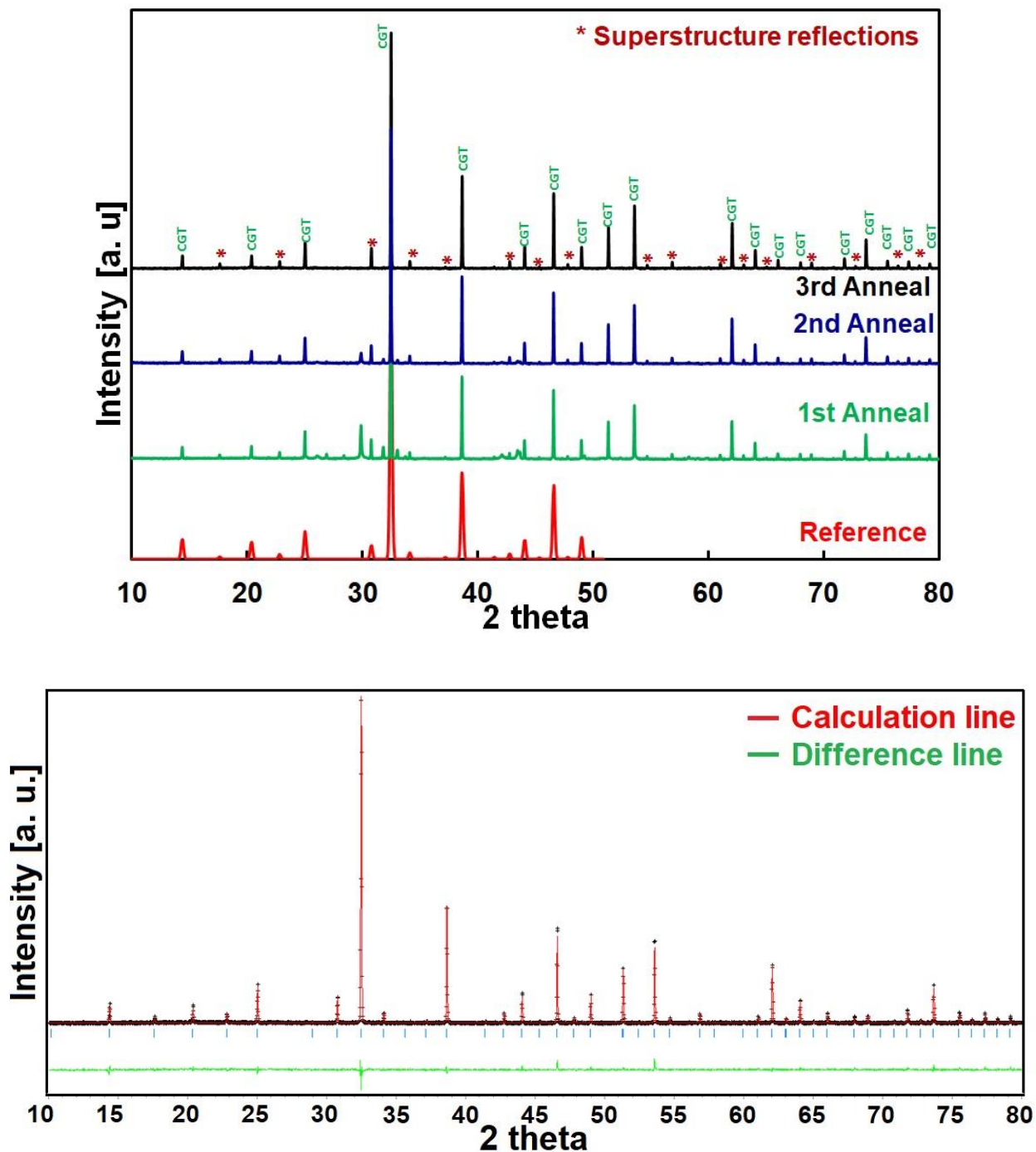


Figure 2-5. (a) Powder X-ray diffraction data for $\text{Co}_4\text{Ge}_6\text{Te}_6$ at different annealing steps. The pattern which is labelled as the reference belongs to [16] (ICDS code 166638) for better comparison. (b) Final observed (crosses), calculated (solid line) and difference (full lower line) profiles from Rietveld refinement of the synthesized and sintered samples using $R\bar{3}$ models.

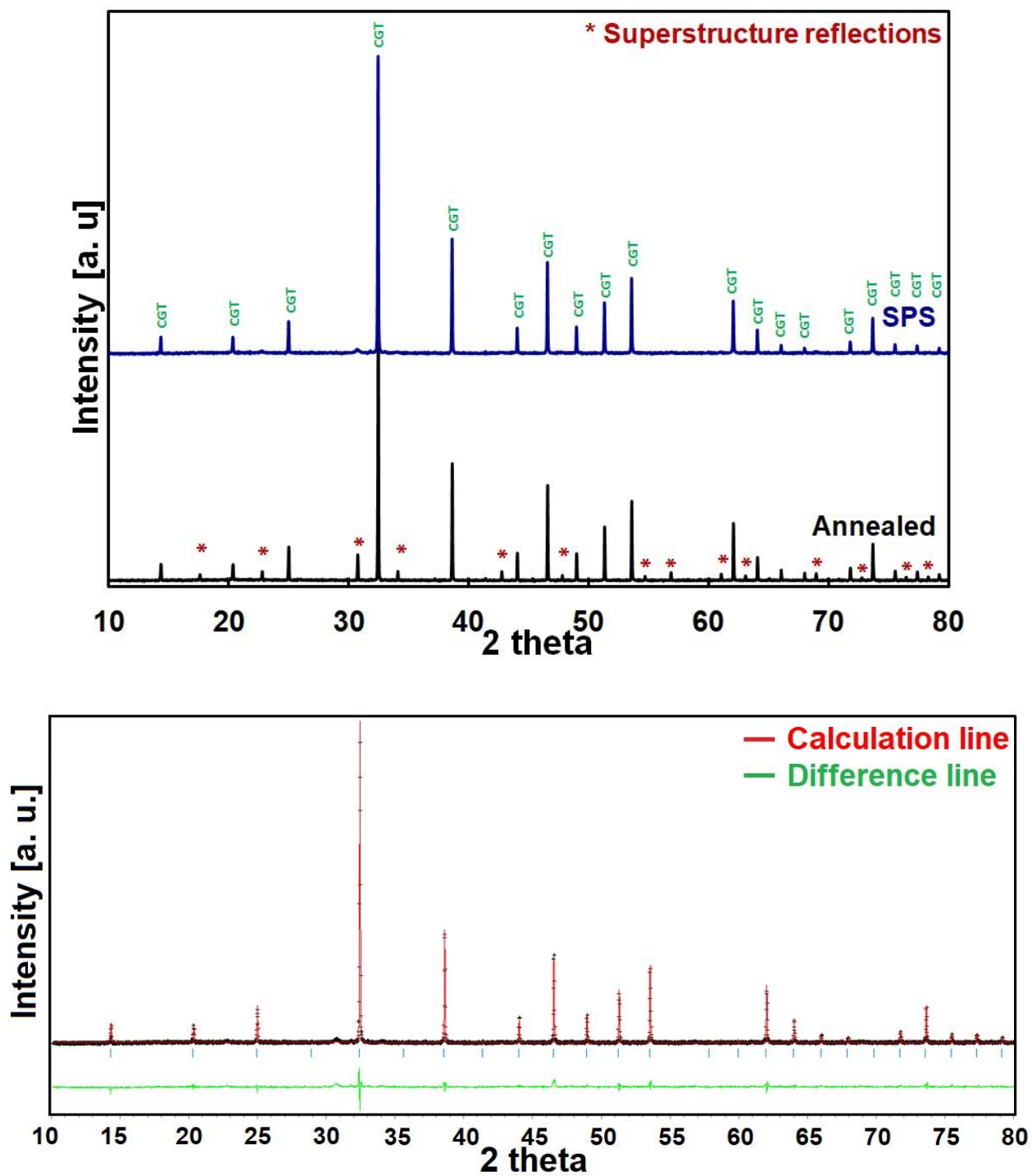


Figure 2-6. (a) Powder X-ray diffraction data before and after sintering. (b) Final observed (crosses), calculated (solid line) and difference (full lower line) profiles from Rietveld refinement of the sintered sample using $Im\bar{3}$ model.

The weaker reflections present in the powder diffraction patterns of $\text{Co}_4\text{Ge}_6\text{Te}_6$ sample violate the body-centred reflection condition ($h+k+l = 2n$) of the typical skutterudite structure (space group $\text{Im}\bar{3}$), while the absence of peak splitting suggests that a cubic unit cell is retained. However, structural models for the skutterudite phase based on cubic subgroups of $\text{Im}\bar{3}$ (such as $\text{Pm}\bar{3}$, $\text{P}23$) failed to reproduce adequately the observed intensities. In contrast, successful refinement of the powder diffraction pattern suggests that $\text{R}\bar{3}$ can be considered as an isotropy subgroup of $\text{Im}\bar{3}$, and extra peaks can be associated with anion ordering along the $[111]$ direction of the original unit cell.

Interestingly, peak splitting, as well as weak superstructure reflections, have been observed for $\text{IrGe}_{1.5}\text{Se}_{1.5}$. Therefore, Rietveld refinement of $\text{IrGe}_{1.5}\text{Se}_{1.5}$ using the anion-ordered structure model based on the space group $\text{R}\bar{3}$ yielded low agreement factors, which was not achieved by using a cubic structural model [37].

Powder diffraction data collected after spark plasma sintering reveals that almost all superstructure relevant reflections are disappeared (Figure 2-6 (a)). All the reflections, except for a small, broad one at 31° , can be indexed based on a cubic unit cell (space group $\text{Im}\bar{3}$). It suggests a phase transformation from rhombohedral to cubic after SPS sintering. Figures 2-5 (b) and 2-6 (b) show successful Rietveld refinements of data collected before and after sintering using rhombohedral (space group $\text{R}\bar{3}$) and cubic skutterudite models (space group $\text{Im}\bar{3}$), respectively. Previously, the structural studies using high-resolution neutron diffraction experiments disclosed that complete anion ordering maintained in $\text{CoGe}_{1.5}\text{S}_{1.5}$ up to its melting temperature ($900 < T \text{ (}^\circ\text{C)} < 950$), while $\text{CoGe}_{1.5}\text{Te}_{1.5}$ experienced an order-disorder transition above 600°C . This may be correlated to the stronger p_π - p_π interactions between Ge and S in the anion rings when compared to the Ge and Te interactions [18]. The site occupancy for the anions in $\text{CoGe}_{1.5}\text{Te}_{1.5}$ stayed nearly constant between

room temperature (0.83(1)) and 555 °C (0.82(1)), but decreased rapidly to 0.5 at 605 °C [18]. This means a statistical distribution of the Ge and Te anions over the Ge_2Te_2 rings after the phase transition. They also demonstrated that the two crystallographically independent Ge_2Te_2 rings (diamond shape with angles that deviate from 90°) in the rhombohedral phase transform into one crystallographically independent anion ring (rectangular shape with angles of 90°) in the cubic skutterudite phase. In other words, an order-disorder transition occurs in $\text{CoGe}_{1.5}\text{Te}_{1.5}$ skutterudite at high temperature [18].

The XRD patterns for each specimen with different Ge contents before SPS sintering are given in Figure 2-7. As the Ge content deviates more from its stoichiometry amount, there is a small number of impurity phases present. Samples with Ge below the stoichiometry amount contain the CoTe_2 impurity phase, while samples with Ge above the stoichiometry ratio have the GeTe impurity. All the other reflections can be indexed according to the rhombohedral unit cell (space group $R\bar{3}$), indicating anion ordering in all samples and tailoring the Ge/Te ratio has no effect on the superstructure formation. After the SPS sintering, the samples with different Ge amounts contain less impurities as well as lower superstructure reflections, meaning that sintering promotes $\text{Co}_4\text{Ge}_6\text{Te}_6$ formation and rhombohedral-to-cubic phase (Figure 2-8).

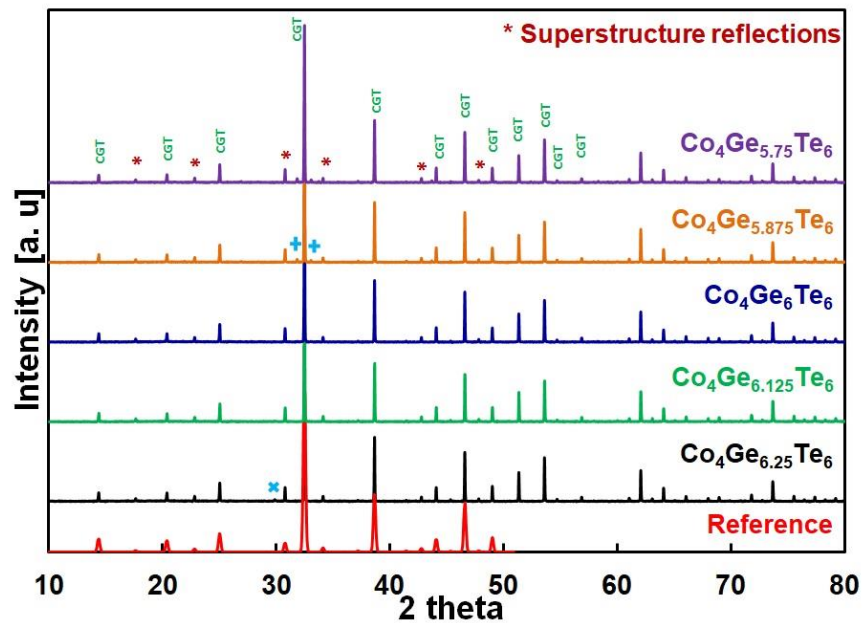


Figure 2-7. Powder XRD patterns of samples with different Ge contents after the 3rd annealing step. A cross sign (X) indicates the GeTe impurity phase and the plus signs (+) indicate the CoTe_2 impurity phase.

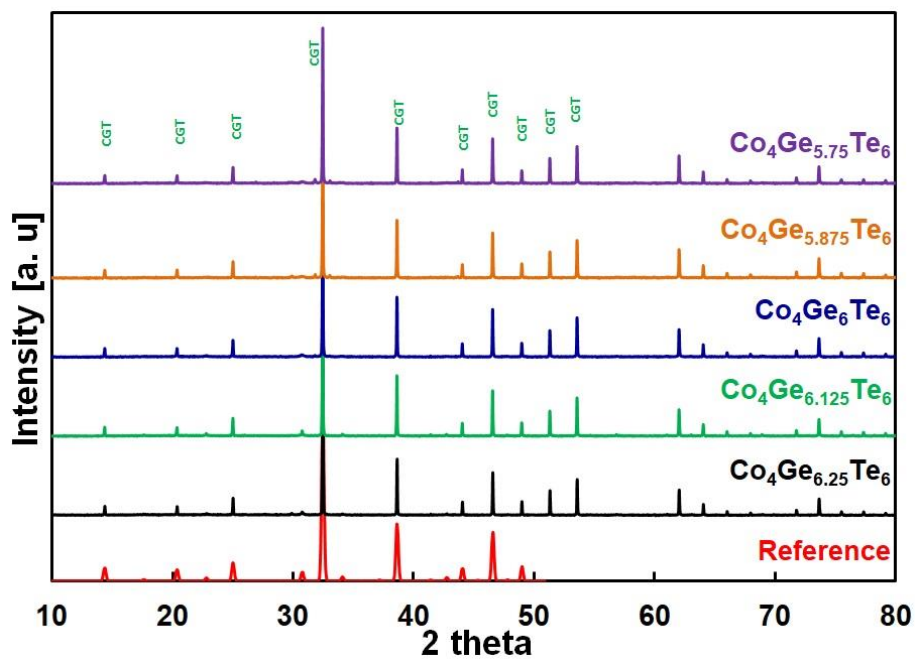


Figure 2-8. Powder XRD patterns of samples with different Ge contents after SPS sintering.

Electrical conductivity, Seebeck coefficient and power factor of $\text{Co}_4\text{Ge}_6\text{Te}_6$ samples upon heating are demonstrated in Figures 2-9. In order to measure physical properties of the sample and to make sure of the consistency of the results, two bars from a sample have been cut and measured. The electrical conductivity increases in both samples with increasing temperature which is consistent with semiconducting behaviour. However, two bars of the same sample exhibit different electrical conductivity, this can be due to errors during the measurement or poor sample quality. In comparison with previous studies, the electrical conductivity of all our samples is higher than the electrical conductivity reported for pure $\text{Co}_4\text{Ge}_6\text{Te}_6$ samples (around $5\text{-}50 \text{ S}\cdot\text{cm}^{-1}$ over 30 to 500 °C) [18]. This inconsistency is smaller for the Seebeck coefficient measurement (Figure 2-9). Although, all samples have a negative Seebeck coefficient, which is consistent with the n-type nature of $\text{Co}_4\text{Ge}_6\text{Te}_6$ Seebeck coefficient values are quite different. The Seebeck coefficient can be as high as $\sim -400 \mu\text{V}\cdot\text{K}^{-1}$ at 150 °C for pure $\text{Co}_4\text{Ge}_6\text{Te}_6$ sample [18], while our highest Seebeck coefficient is lower than $-100 \mu\text{V}\cdot\text{K}^{-1}$.

Accordingly, the discrepancies in electrical conductivities and Seebeck coefficients lead to different power factors for each bar (Figure 2-9). In order to find the reasons for having such diverse results, more detail structural and microstructural analysis were necessary.

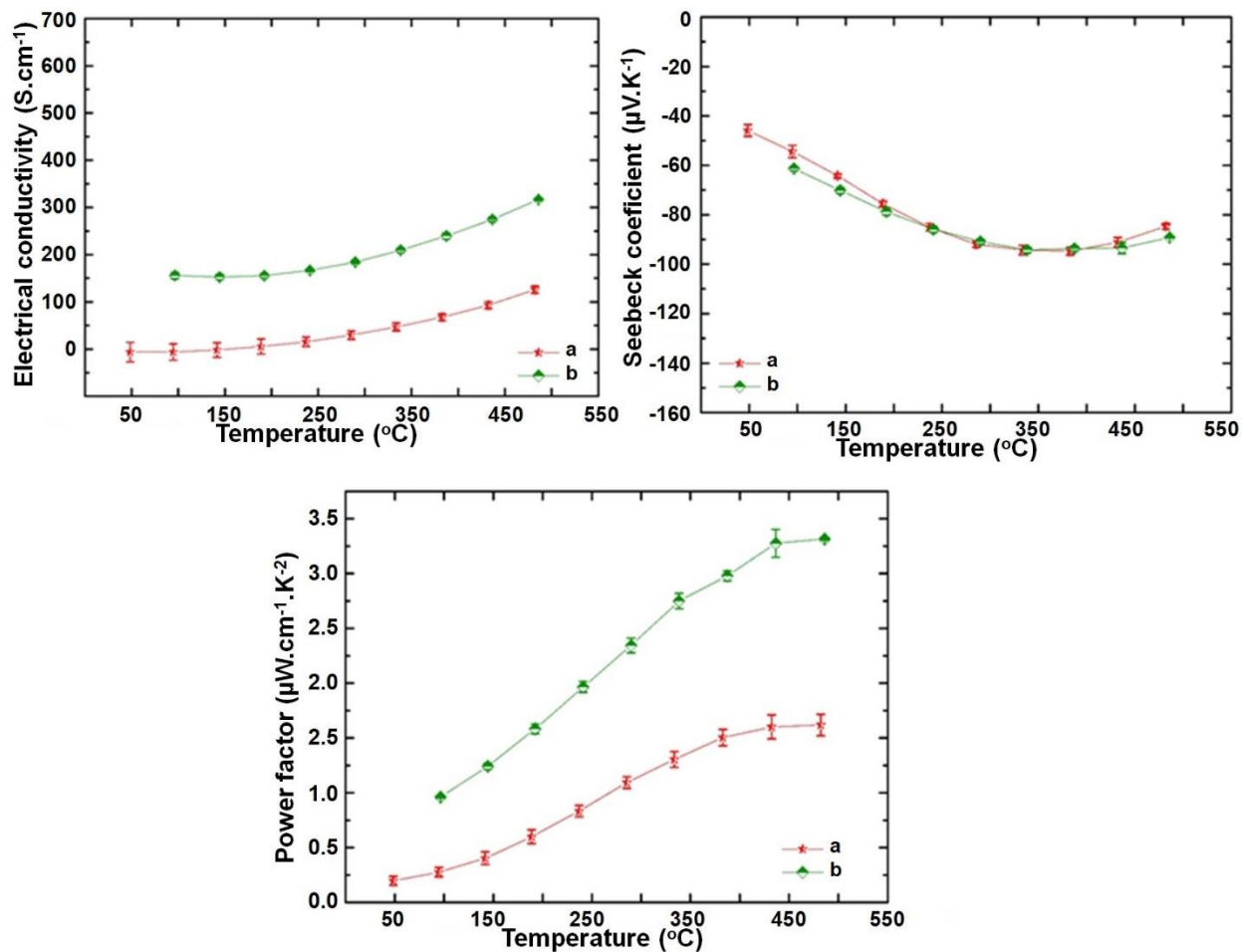


Figure 2-9. Electrical conductivity, Seebeck coefficient, and Power factors of stoichiometry CGT sample over the temperature range 100-500 °C. Two bars from a sample have been cut and measured.

X-ray diffraction analysis was carried out on different areas of bulk stoichiometry $\text{Co}_4\text{Ge}_6\text{Te}_6$ sample after SPS sintering (Figure 2-10). There were extra peaks in all diffraction patterns collected from different spots of the sample in addition to the $\text{Co}_4\text{Ge}_6\text{Te}_6$ reflections. Rietveld refinement of the diffraction pattern from the middle spot on the top of the bulk sample is shown in Figure 2-10 (c) and the weight percentage of all phases is summarised in Table 2-3. This particular spot has around 50% of the main $\text{Co}_4\text{Ge}_6\text{Te}_6$ phase and the rest are other phases.

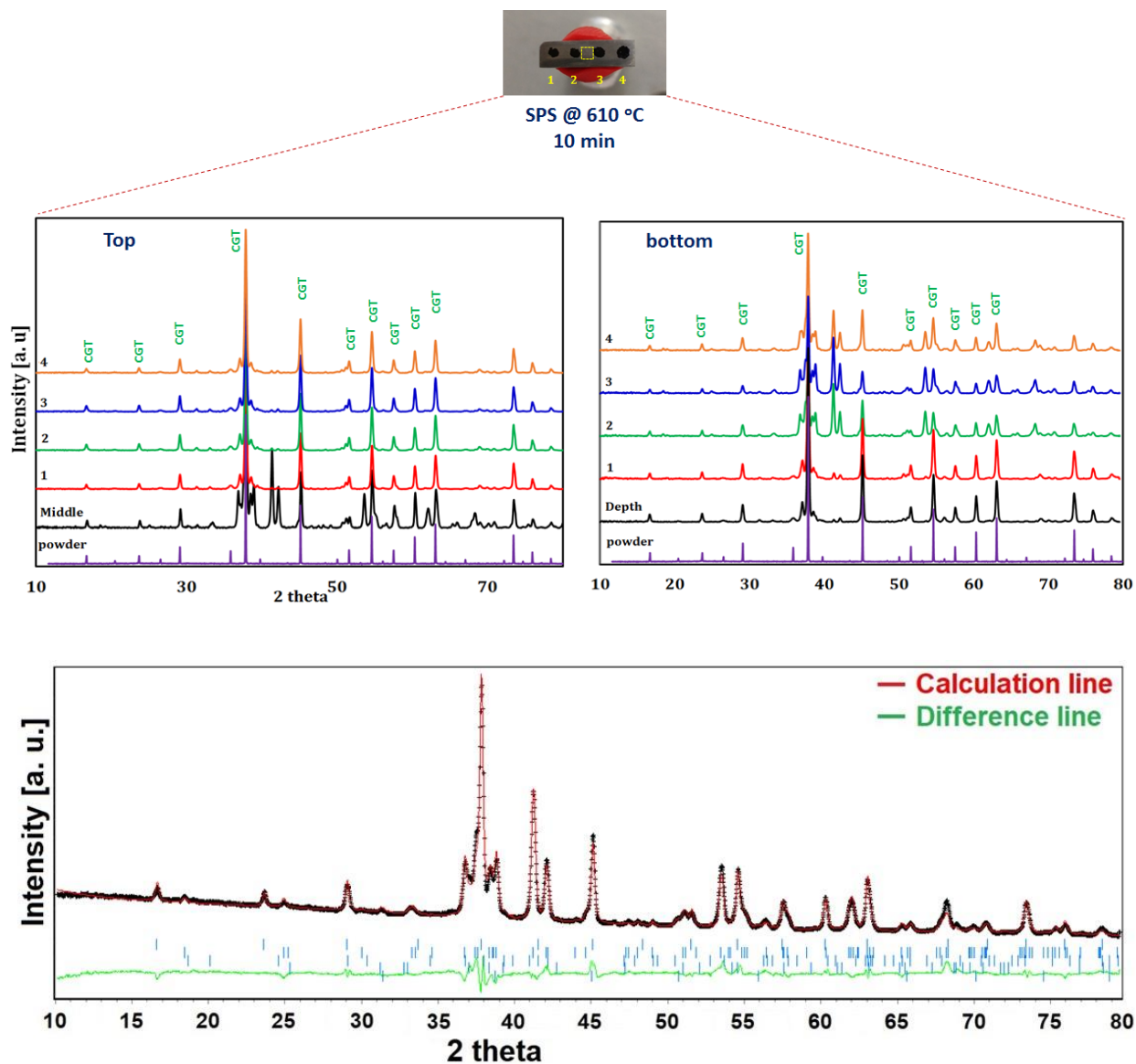


Figure 2-10. X-ray diffraction patterns of bulk $\text{Co}_4\text{Ge}_6\text{Te}_6$ sample after sintering at $610\text{ }^\circ\text{C}$ for 10 min from different places of (a) top side and (b) bottom side of the sample. (c) Rietveld refinement of X-ray diffraction pattern for the middle spot in (a) ($\text{Co}_4\text{Ge}_6\text{Te}_6$ sample after sintering) including profile fit, profile difference, and profile residuals.

Table 2-3. The weight percentage of different phases in the middle of the $\text{Co}_4\text{Ge}_6\text{Te}_6$ sample after SPS sintering obtained from the Rietveld refinement.

Phases	Weight Percentage of Phases
$\text{Co}_4\text{Ge}_6\text{Te}_6$	46.8(3)
CoGeTe	42.5(3)
CoTe_2	7.1(2)
CoGe	3.6(2)

The amount of secondary phases vary from one area to another, as apparent from the diffraction patterns in Figure 2-10. These data are in contradiction with the powder diffraction pattern of the sintered samples, shown in Figure 2-6 (a). Such discrepancy can be explained by the fact that a small piece from the edge of each sample was cut, hand ground and analyzed via X-ray diffraction. It has been proven that spark plasma sintering may cause a non-uniform temperature gradient inside the sample, with the temperature on the edges being different from the temperature in the middle [26]. Therefore, different secondary phases may be present at the edges and center of the sintered sample.

We have tried different SPS temperatures and times in order to avoid formation of secondary phases. X-ray diffraction analysis on different areas of bulk $\text{Co}_4\text{Ge}_6\text{Te}_6$ samples sintered at 575 °C for 25 min, 535 °C for 40 min, and 500 °C for an hour are shown in Figures 2-11, 2-12 and 2-13, respectively. There are impurity peaks in all diffraction patterns collected from different spots, but they are much lower than those in the sample sintered at 610 °C (Figure 2-10). These results indicate that lowering the sintering temperature increased the sample purity. Sintering at 500 °C for 1 hour failed to create a dense sample with good mechanical properties (Figure 2-13). Although

increasing the SPS temperature to 535 °C improve the sample's hardness, the secondary phases were still present (Figure 2-12). Therefore, the best sintering temperature is 575 °C (Figure 2-11) but with shorter holding time to minimize formation of other phases.

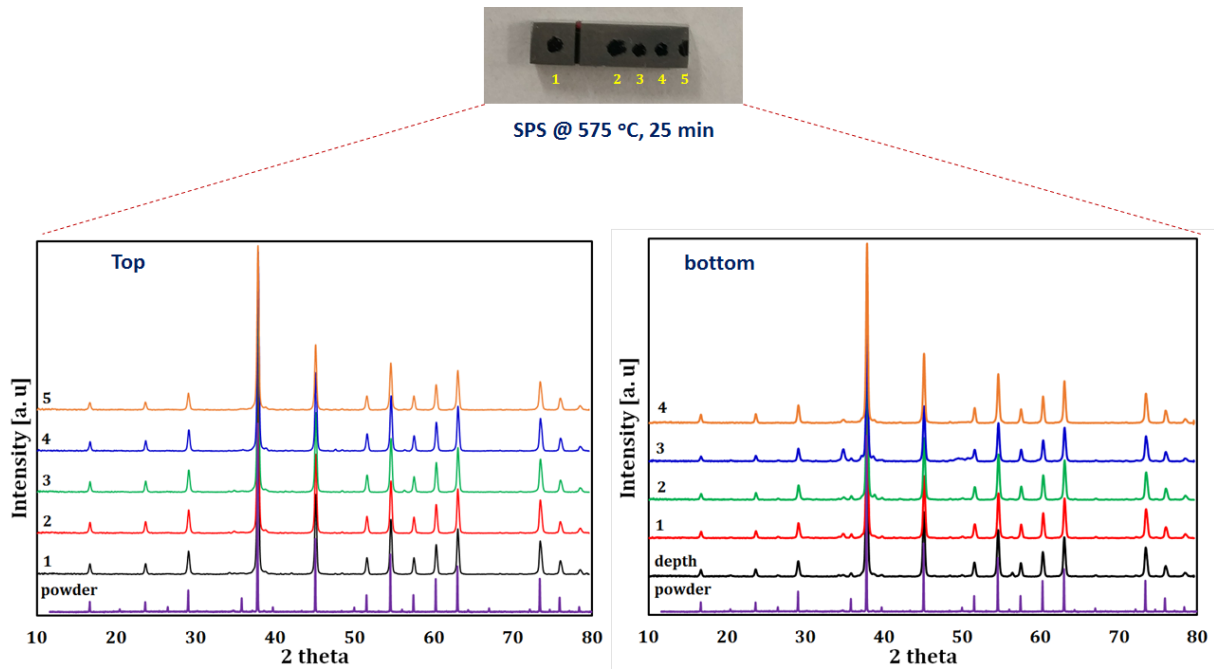


Figure 2-11. X-ray diffraction patterns from different places at the (a) top and (b) bottom sides of the bulk $\text{Co}_4\text{Ge}_6\text{Te}_6$ sample after sintering at 575 °C for 25 min.

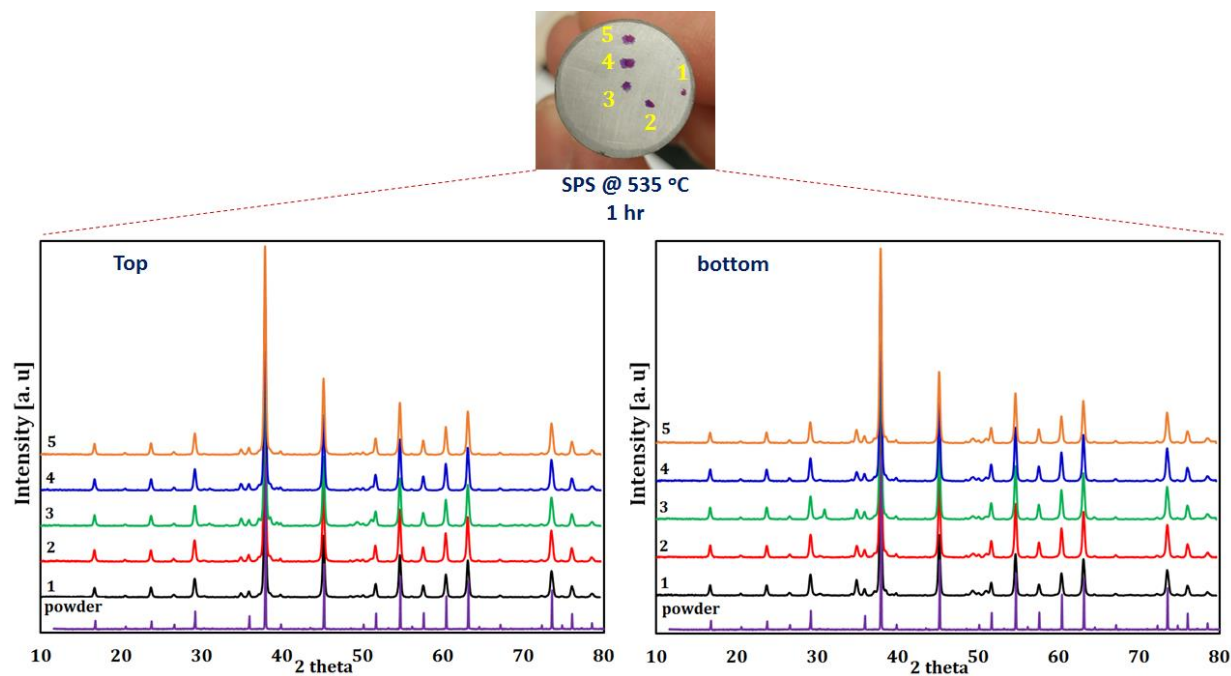


Figure 2-12. X-ray diffraction patterns from different places at the (a) top and (b) bottom sides of the bulk $\text{Co}_4\text{Ge}_6\text{Te}_6$ sample after sintering at 535 °C for 40 min.

SEM and EDX analyses were performed to investigate the microstructure in more details. Figure 2-14 and Table 2-4 represent the microstructure of different areas of the stoichiometric $\text{Co}_4\text{Ge}_6\text{Te}_6$ sample together with their EDX elemental analysis. Interestingly, different areas of the sample have different compositions. Elemental EDX mapping is given in Figure 2-15, it shows distribution of each element in a relatively big area of the surface of the sample. Ge is distributed almost uniformly entire the sample. However, there are some Co-rich and Te-deficient regions. The SEM backscattering mode confirms that the sample is not homogenous (Figure 2-16). The EDX compositions of 10 different regions of the $\text{Co}_4\text{Ge}_6\text{Te}_6$ sample are summarised in Table 2-5. In the black regions, there are almost no Te. Grey areas have an almost stoichiometric composition, while whiter places have slightly more Te. These results prove that the sample is not uniform microstructurally.

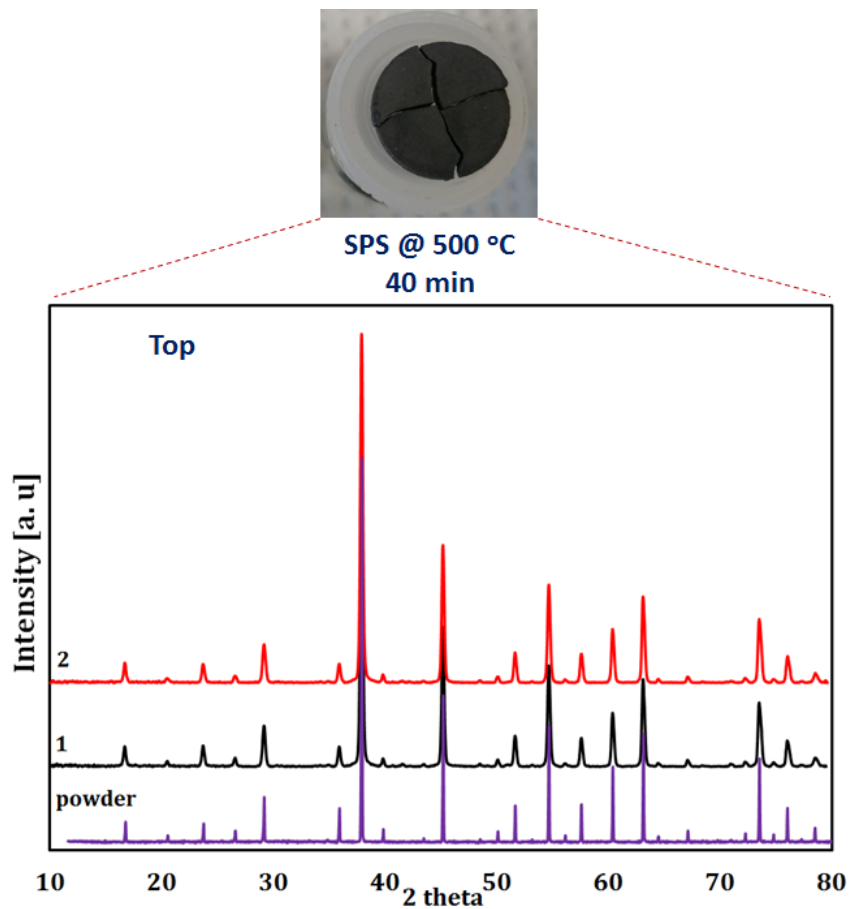


Figure 2-13. X-ray diffraction patterns from different places at the (a) top and (b) bottom sides of the bulk $\text{Co}_4\text{Ge}_6\text{Te}_6$ sample after sintering at 500 °C for 60 min.

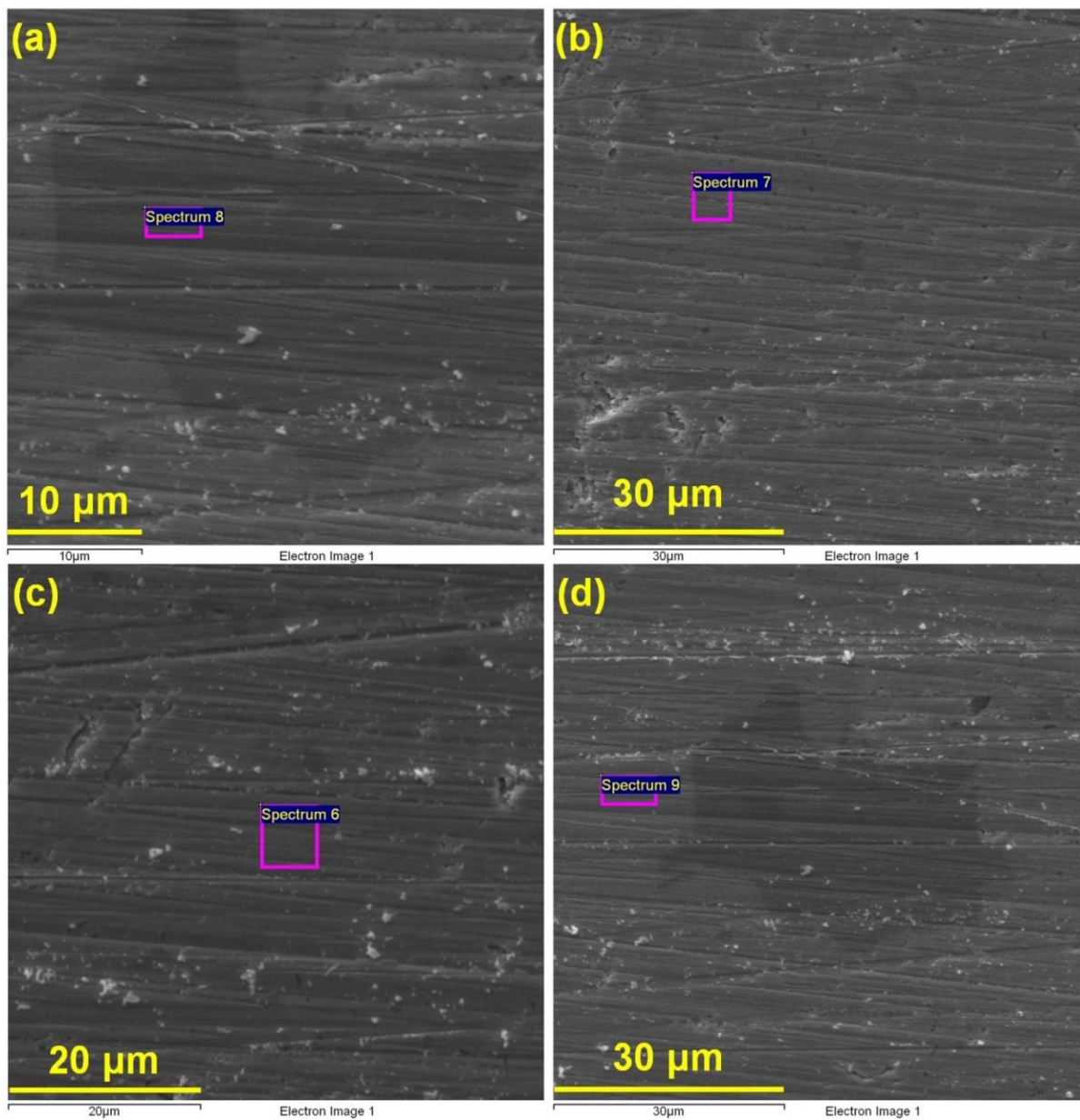


Figure 2-14. SEM micrographs of the surface of the bulk $\text{Co}_4\text{Ge}_6\text{Te}_6$ sample after SPS.

Chemical compositions of the labelled regions are determined by EDX analysis.

Table 2-4. EDX quantitative analysis of 4 different areas of the $\text{Co}_4\text{Ge}_6\text{Te}_6$ sample shown in Figure 2-14. The nominal stoichiometric composition is $\text{Co}_{25}\text{Ge}_{37.5}\text{Te}_{37.5}$ in atomic (Atm%) percentage.

Element	(a)	(b)	(c)	(d)
	Atm%	Atm%	Atm%	Atm%
Co K	48.71	24.52	32.08	30.22
Ge K	51.29	37.13	33.90	34.74
Te L	-	38.35	34.02	35.05

Indeed, a sample with non-uniform composition will give inconsistency physical properties. The reasons for the decomposition can be improper SPS temperature and duration. Furthermore, the electrical current passing through the sample may have caused migration of high mobility species inside the sample and formation of secondary phases in different regions of the sample. Another possibility is that non-uniform electrical current inside the sample leads to temperature overshoots inside the sample causing phase decomposition.

Lim et. al. [27] explored the effect of SPS conditions on microstructural evolution, and the thermoelectric properties of p-type $(\text{Bi}_{0.25}\text{Sb}_{0.75})_2\text{Te}_3$ materials. They showed that the relatively low eutectic temperature and the presence of volatile tellurium (Te) are important parameters to control both microstructure and thermoelectric properties. Rapid evaporation of Te leads to a strong dependence of thermoelectric property on SPS conditions which needs to be carefully optimized for materials containing volatile elements with low eutectic temperature.

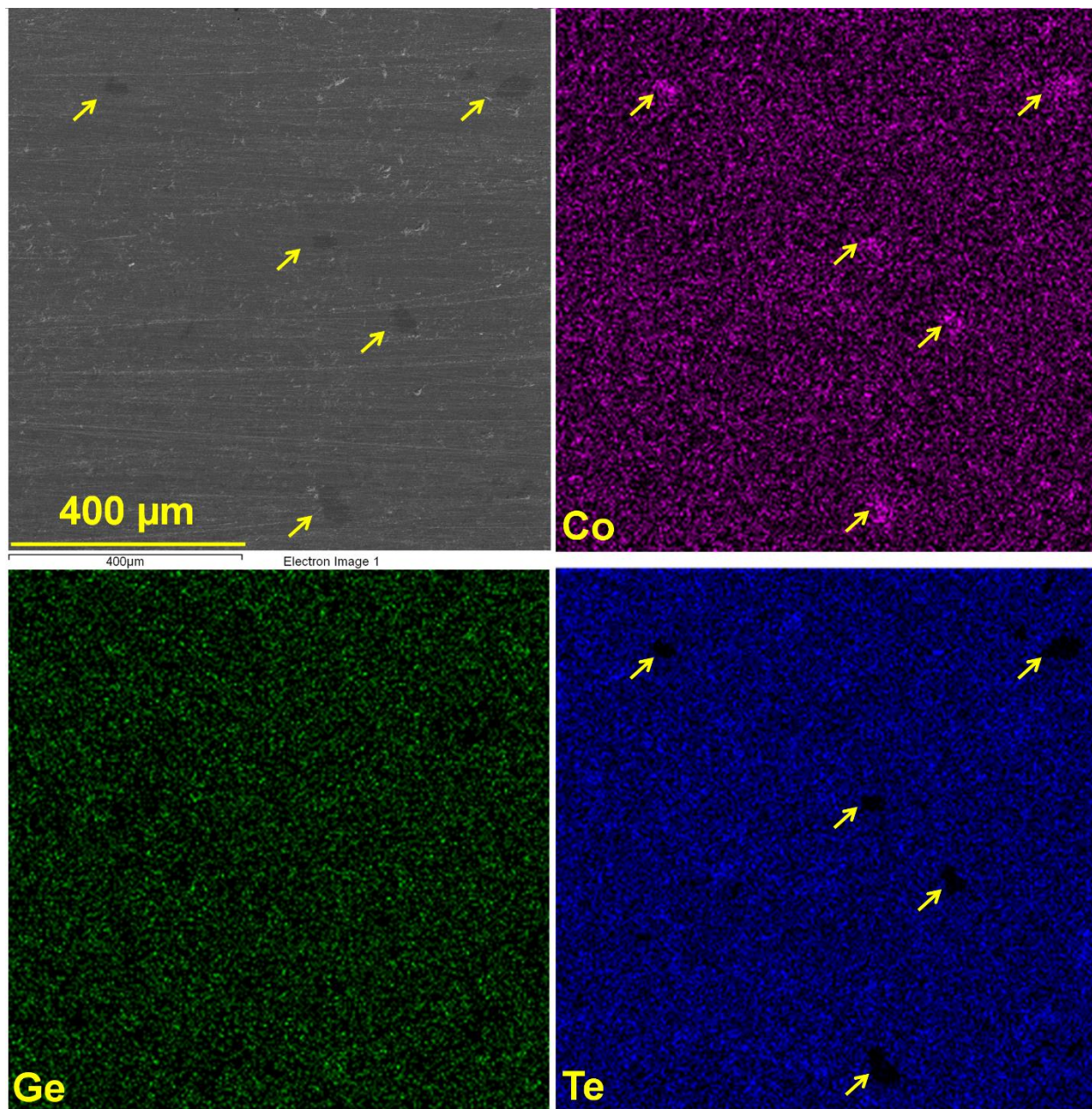


Figure 2-15. (a) Secondary electron image, and (b-d) elemental mappings of Co, Ge, and Te in the polished $\text{Co}_4\text{Ge}_6\text{Te}_6$ sample prepared via SPS. Ge is almost distributed uniformly while there are some Co-rich and Te-deficient regions.

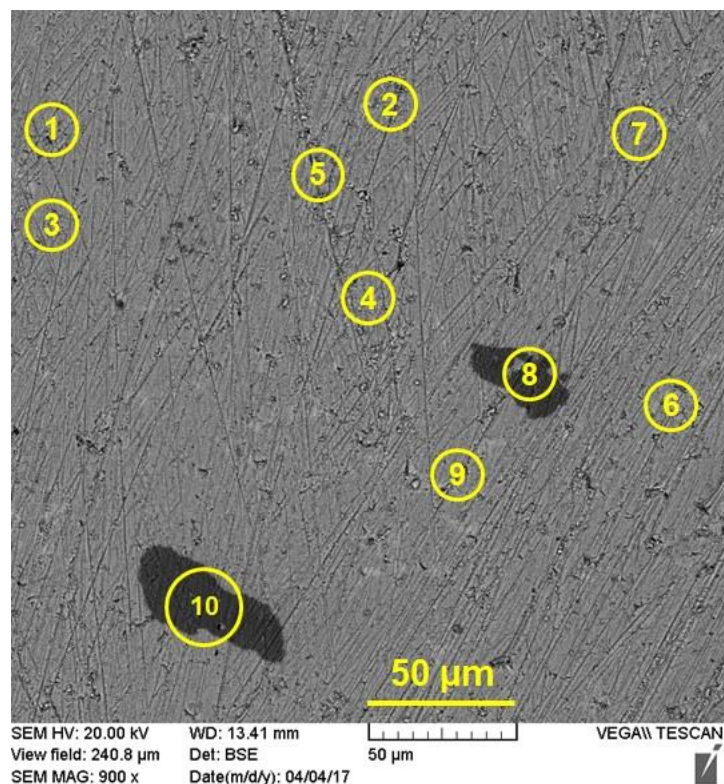


Figure 2-16. Back-scattered electron image of the bulk $\text{Co}_4\text{Ge}_6\text{Te}_6$ sample. Non-uniform contrast indicates differences in composition and phase distribution throughout the sample.

Table 2-5. EDX quantitative analysis of 10 different spots of $\text{Co}_4\text{Ge}_6\text{Te}_6$ sample has been shown in figure 2-16 (all values are in weight percentage). The nominal stoichiometric composition is

$\text{Co}_{25}\text{Ge}_{37.5}\text{Te}_{37.5}$ in atomic percentage.

Element	1	2	3	4	5	6	7	8	9	10
Co	19.25	24.88	23.59	21.71	23.63	16.78	24.00	47.28	18.90	47.41
Ge	40.64	34.61	39.03	39.57	38.76	41.44	37.99	50.97	41.56	51.67
Te	40.11	40.51	37.39	38.72	37.61	41.78	38.01	1.75	39.54	0.92

It has been also demonstrated that Zn_4Sb_3 is thermally unstable at elevated temperatures [38-40] due to the migration of highly mobile Zn ions in the structure [41-43]. Consequently, ZnSb, Zn, and Sb were formed when Zn_4Sb_3 was heated to 625 K [39]. Using Seebeck microprobe analysis, Yin et. al. [31] also distinguished different sections with different Seebeck coefficients which stemmed from the compositional changes in the pellet. They proposed that decomposition and resulting compositional variation in the pellet may be related to the inhomogeneous current density within the pellet during SPS. In another word, Zn^{2+} cations are driven by the electrical potential during SPS and subsequently accumulate at the cathode. The compositional gradient leads to a significant inhomogeneity in the Seebeck coefficient. Similarly, Zhang et. al. [33] studied the thermoelectric properties of Zn_4Sb_3 prepared by spark plasma sintering (SPS) method. They detected a reversible structural transformation between Zn_4Sb_3 and ZnSb. The as-milled powder was composed of the pure Zn_4Sb_3 phase, however after SPS, one side of the sintered pellet converted to the ZnSb phase. The Zn_4Sb_3 phase has been retrieved annealing at 300 °C using positron annihilation lifetime measurements, Zhang et. al. [33] confirmed that Zn migration driven by direct current and Zn diffusion activated by annealing were driving forces for these phase transformations. They also found that extra Zn can impede the decomposition of β - Zn_4Sb_3 into ZnSb and Zn.

In order to avoid the abovementioned issues, lower sintering temperature as well as electrically insulating film between the sample and die punches were employed. We used Mica film to separate the graphite punches and CGT powder during the SPS process. It is worth mentioning that, Tomida et. al. [34] detected temperature difference caused by the Peltier effect during the SPS sintering of large n-type $(Yb \text{ or } La, Ca, Al, Ga, In)_{0.8}(Co, Fe)_4Sb_{12}$ skutterudite samples. Therefore, an electrical insulating material (Mica) was introduced between the punches and the sintering body

to stop the Peltier effect. Consequently, an n-type La-filled skutterudite sample with a diameter of 200 mm, the thickness of 21 mm, and weight of 5 kg was effectively manufactured [34]. Figure 2-17 schematically illustrates the difference in current pathways through the sample and graphite die without and with Mica films. When a Mica film is present, the pulsed direct current cannot flow directly through the sintering body. This minimizes non-homogeneous current distribution through the sample and eliminates Peltier heating at the top and bottom surfaces.

Interestingly, electrical conductivity and Seebeck coefficient of samples sintered using a Mica film (Figure 2-18) presents very good agreement with literature. This means that the phase composition and thus physical properties of a sample are affected by the compaction process and caution needs to be taken during sintering step. In our case, having an insulator barrier layer to avoid huge electrical current passing directly through the sample is essential.

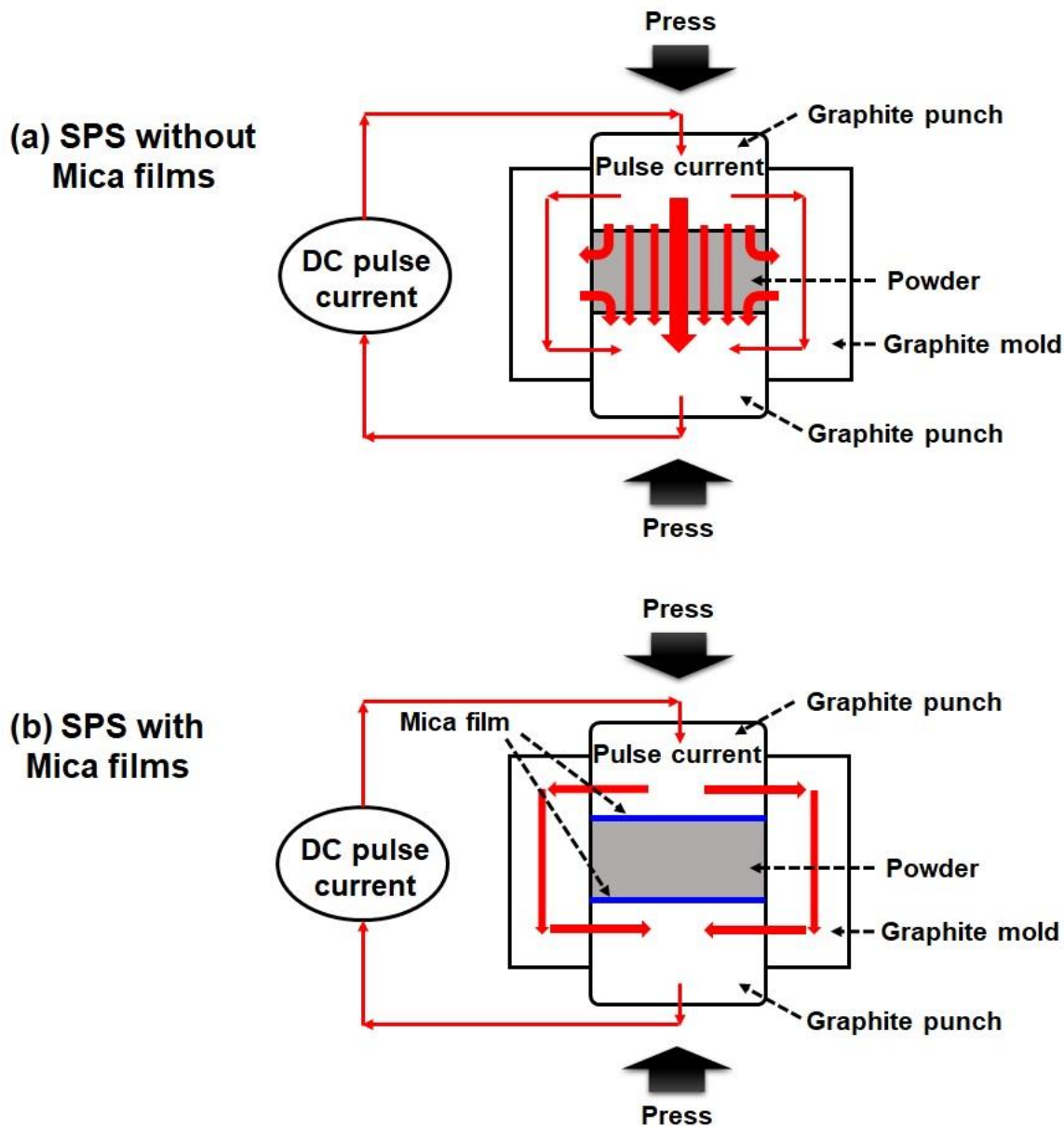


Figure 2-17. Schematic configuration of SPS equipment showing the electrical current pathways within the sample and graphite die (a) without and (b) with using Mica films.

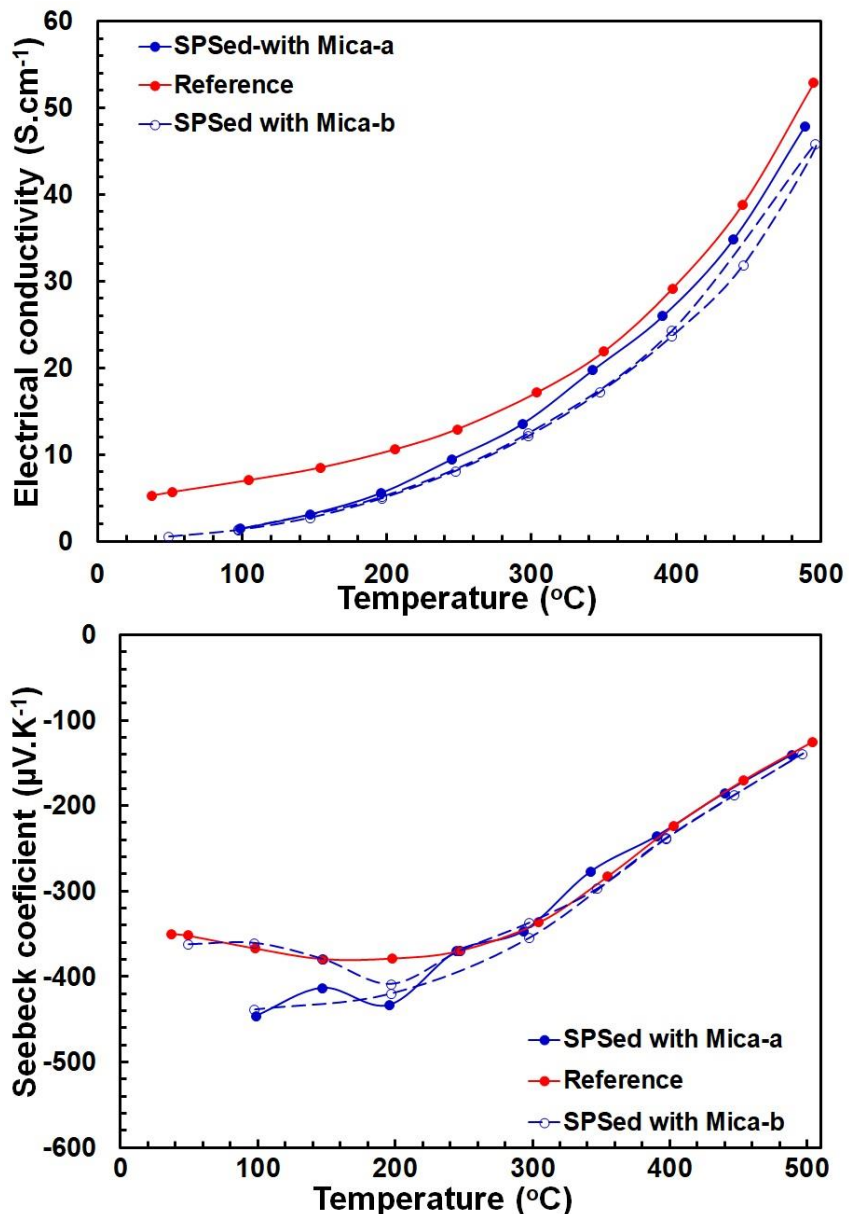


Figure 2-18. Electrical conductivity and Seebeck coefficient of $\text{Co}_4\text{Ge}_6\text{Te}_6$ samples spark plasma sintered (a, b) without (c, d) with Mica films. Two bars have been cut and measured for each sample. The reference results are extracted from ref [18].

XRD patterns for the Sb-doped samples before sintering are shown in Figure 2-19. A small number of impurity phases is visible in the XRD patterns when the dopant concentration is large. Specifically, samples with a higher amount of Sb contain CoSb_2 and GeTe impurity phases.

Moreover, the presence of anion ordering in all samples is evident and all reflections can be indexed according to the rhombohedral unit cell (space group $R\bar{3}$). However, the same sample after SPS sintering have fewer impurities as well as a reduced amount of superstructure reflections, meaning that sintering promotes the $\text{Co}_4\text{Ge}_6\text{Te}_6$ formation and rhombohedral-to-cubic transformation.

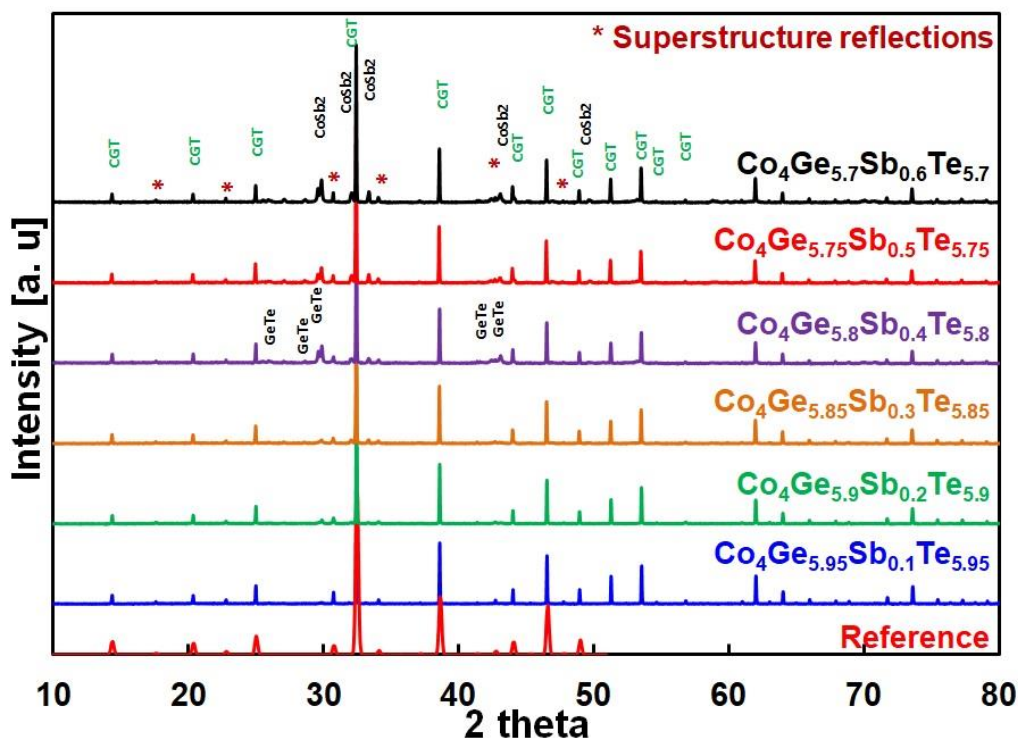


Figure 2-19. Powder XRD patterns of synthesised Sb-doped samples after the 3rd annealing step.

Figures 2-20 depict the thermoelectric properties of Sb-doped samples at different temperatures. Similar to the previous experiments, two bars from each sample have been cut and measured. Sb-doped samples show a slight decrease in electrical conductivity over the measured temperature range. The electrical conductivity of all the doped samples are higher in comparison with the electrical conductivity of pure $\text{Co}_4\text{Ge}_6\text{Te}_6$ sample [14].

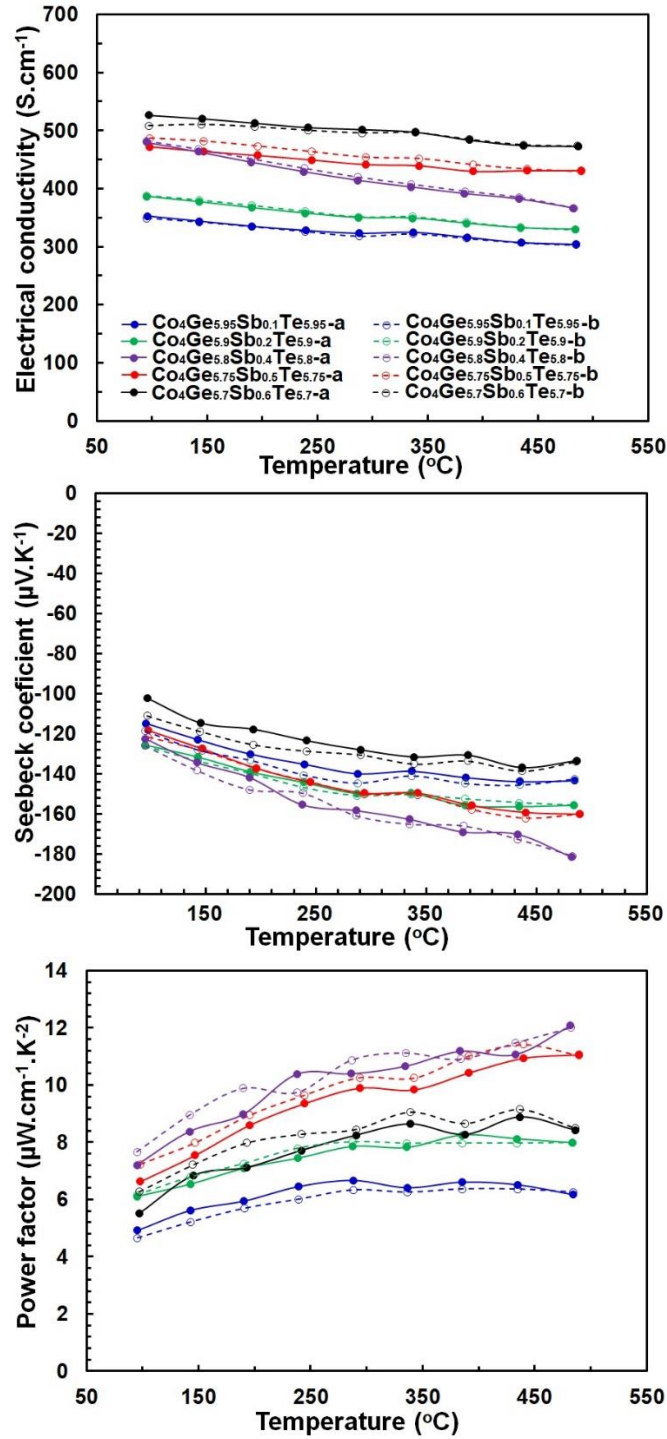


Figure 2-20. Electrical conductivity, seebeck coefficient and power factor of Sb-doped specimens as a function of temperature.

Seebeck coefficient of all samples has negative values, representative of an n-type behavior. All samples have a lower negative Seebeck coefficient (in absolute terms) than the pure $\text{Co}_4\text{Ge}_6\text{Te}_6$ sample [18]. Although the Seebeck coefficient is lower, much higher electrical conductivity of the Sb-doped samples lead to the significant enhancements in their power factors when compared to the pure $\text{Co}_4\text{Ge}_6\text{Te}_6$. (Figure 2-20). To the best of our knowledge, Sb-doped samples exhibit the highest power factors reported for $\text{Co}_4\text{Ge}_6\text{Te}_6$ derivatives, so far. Although samples have been sintered at 575 °C for 25 minutes, their thermoelectric properties are highly consistent over all temperature ranges, which suggests compositional homogeneity throughout the sample.

2-5. Conclusion

The thermoelectric properties of $\text{Co}_4\text{Ge}_6\text{Te}_6$ (CGT) samples depend significantly on sample purity and microstructural uniformity. Accordingly, the sintering step seems to be the most important step in sample preparation in order to obtain the best TE performance. The Peltier effect, migration of high mobile species, etc. may result in compositional and microstructural variations, which affect the physical properties of the compacted sample. CGT may be an extreme case due to the tendency to decompose at elevated temperatures, but in general, characterization of a TE sample after SPS has to be performed with caution. Furthermore, anion substitution affects both the electrical conductivity and Seebeck coefficient and therefore substitution of anion rings can be expected to have a major effect on the properties of these materials. Sb-doped samples demonstrated the highest power factors achieved for $\text{Co}_4\text{Ge}_6\text{Te}_6$ compounds, so far.

2-6. References

- [1] A. Dey, O. P. Bajpai, A. K. Sikder, S. Chattopadhyay, and M. A. S. Khan, "Recent advances in CNT/graphene based thermoelectric polymer nanocomposite: A proficient move towards waste energy harvesting," *Renewable and Sustainable Energy Reviews* 53, vol. 53, pp. 653–671, 2016.
- [2] D. K. Aswal, R. Basu, and A. Singh, "Key issues in development of thermoelectric power generators: High figure-of-merit materials and their highly conducting interfaces with metallic interconnects," *Energy Conversion and Management*, vol. 114, pp. 50–67, 2016.
- [3] X. Zhang and L.-D. Zhao, "Thermoelectric materials: Energy conversion between heat and electricity," *Journal of Materiomics*, vol. 1, pp. 92-105, 2015.
- [4] K. V. Selvana and M. S. M. Ali, "Micro-scale energy harvesting devices: Review of methodological performances in the last decade," *Renewable and Sustainable Energy Reviews*, vol. 54, pp. 1035-1047, 2016.
- [5] P. Vaquero, G. G. Sobany, and M. Stindl, "Structure and electrical transport properties of the ordered skutterudites $M\text{Ge}_{1.5}\text{S}_{1.5}$ ($M = \text{Co}, \text{Rh}, \text{Ir}$)," *Journal of Solid State Chemistry*, vol. 181, pp. 768–776, 2008.
- [6] F. Laufeka, J. Navrátil, J. Pláčil, T. Plecháček, and C. Dražsar, "Synthesis, crystal structure and transport properties of skutterudite-related $\text{CoSn}_{1.5}\text{Se}_{1.5}$," *Journal of Alloys and Compounds*, vol. 479, pp. 102–106, 2009.
- [7] H. Luo *et al.*, "A large family of filled skutterudites stabilized by electron count," *Nature Communications*, vol. 6, pp. 6489-6497, 2015.
- [8] M. M. Koza, M. R. Johnson, R. Viennois, H. Mutka, L. Girard, and D. Ravot, "Breakdown of phonon glass paradigm in la- and ce-filled $\text{fe}_4\text{sb}_{12}$ skutterudites," *Nature Mater.*, vol. 7, pp. 805–810, 2008.
- [9] G. S. Nolas, G. Fowler, and J. Yang, "Assessing the role of filler atoms on the thermal conductivity of filled skutterudites," *J. Appl. Phys.*, vol. 100, p. 043705, 2006.

- [10] P. F. Qui *et al.*, "High-temperature electrical and thermal transport properties of fully filled skutterudites RFe_4Sb_{12} ($R=Ca, Sr, Ba, La, Ce, Pr, Nd, Eu,$ and Yb)," *J. Appl. Phys.*, vol. 109, p. 063713, 2011.
- [11] B. Sales, D. Mandrus, B. C. Chakoumakos, V. Keppens, and J. R. Thompson, "Filled skutterudite antimonides: Electron crystals and phonon glasses," *Phys. Rev. B*, vol. 56, p. 15081, 1997.
- [12] R. J. Cava and J. W. G. Bos, "Synthesis, crystal structure and thermoelectric properties of $IrSn_{1.5}Te_{1.5}$ -based skutterudites," *Solid State Commun.*, vol. 141, pp. 38–41, 2007.
- [13] J. Navratil, T. Plechacek, L. Benes, C. Drasar, and F. Laufek, "Thermoelectric properties of $Co_4Sn_6Se_6$ ternary skutterudites," *Journal of Electronic Materials*, vol. 39, pp. 1880–1884, 2010.
- [14] J. Navrátil, T. Plecháček, L. Beneš, and M. Vlček, "SOME TRANSPORT PROPERTIES OF $CoGe_{1.5}Te_{1.5}$," *J. Optoelect. Adv. Mat.*, vol. 6, pp. 787–790, 2004.
- [15] P. Vaqueiro and G. G. Sobany, "Ternary skutterudites: Anion ordering and thermoelectric properties," in *MRS Fall Meeting, 2007: Mater. Res. Soc. Symp. Proc.*
- [16] P. Vaqueiro, G. G. Sobany, and A. V. Powell, "A synchrotron powder X-ray diffraction study of the skutterudite-related phases $AB_{1.5}Te_{1.5}$ ($A = Co, Rh, Ir; B = Ge, Sn$)," *Dalton Transactions*, vol. 39, pp. 1020–1026, 2010.
- [17] P. Vaqueiro, G. G. Sobany, A. V. Powell, and K. S. Knight, "Structure and thermoelectric properties of the ordered skutterudite $CoGe_{1.5}Te_{1.5}$," *J. Solid State Chem.*, vol. 179, pp. 2047–2053, 2006.
- [18] A. Kaltzoglou, A. V. Powell, K. S. Knight, and P. Vaqueiro, "High-temperature order–disorder transitions in the skutterudites $CoGe_{1.5}Q_{1.5}$ ($Q=S, Te$)," *Journal of Solid State Chemistry*, vol. 198, pp. 525–531, 2013.
- [19] D. Volja, B. Kozinsky, A. Li, D. Wee, N. Marzari, and M. Fornari, "Electronic, vibrational, and transport properties of pnictogen-substituted ternary skutterudites," *Physical Review B*, vol. 85, p. 245211, 2012.

- [20] G. S. Nolas, J. Yang, and R. W. Ertenberg, "Transport properties of $\text{CoGe}_{1.5}\text{Se}_{1.5}$," *Physical Review B*, vol. 68, p. 193206, 2003.
- [21] A. Zevalkink *et al.*, "Electronic structure and thermoelectric properties of pnictogen-substituted $\text{ASn}_{1.5}\text{Te}_{1.5}$ (A = Co, Rh, Ir) skutterudites," *Journal of Applied Physics*, vol. 118, p. 035107, 2015.
- [22] Y. Dong, K. Wei, and G. S. Nolas, "Transport properties of partially filled skutterudite derivatives $\text{Ce}_{0.13}\text{Co}_4\text{Ge}_6\text{Se}_6$ and $\text{Yb}_{0.14}\text{Co}_4\text{Ge}_6\text{Se}_6$," *Physical Review B*, vol. 87, p. 195203, 2013.
- [23] Y. Nagamoto, K. Tanaka, and T. Koyanagi, "Thermoelectric Properties of the Skutterudite-Related Phase $\text{CoSn}_{1.5}\text{Te}_{1.5}$," presented at the 16th International Conference on Thermoelectrics, 1997.
- [24] J. Navratil, T. Plechacek, C. Drasar, and F. Laufek, "Thermoelectric Properties of RuSb_2Te Ternary Skutterudites," (in English), *Journal of Electronic Materials*, Article vol. 42, no. 7, pp. 1864-1869, Jul 2013.
- [25] S. Bang, D. Wee, A. Li, M. Fornari, and B. Kozinsky, "Thermoelectric properties of pnictogen-substituted skutterudites with alkaline-earth fillers using first-principles calculations," *Journal Of Applied Physics*, vol. 119, pp. 205102-205109, 2016.
- [26] O. Guillon *et al.*, "Field-Assisted Sintering Technology/ Spark Plasma Sintering: Mechanisms, Materials, and Technology Developments," *ADVANCED ENGINEERING MATERIALS* vol. 16, pp. 830-849, 2014.
- [27] S. S. Lim *et al.*, "Effect of spark plasma sintering conditions on the thermoelectric properties of $(\text{Bi}_{0.25}\text{Sb}_{0.75})_2\text{Te}_{-3}$ alloys," (in English), *Journal of Alloys and Compounds*, Article vol. 678, pp. 396-402, Sep 2016.
- [28] M. Omori, "Sintering, consolidation, reaction and crystal growth by the spark plasma system (SPS)," (in English), *Materials Science and Engineering a-Structural Materials Properties*

- Microstructure and Processing*, Article; Proceedings Paper vol. 287, no. 2, pp. 183-188, Aug 2000.
- [29] U. Anselmi-Tamburini, S. Gennari, J. E. Garay, and Z. A. Munir, "Fundamental investigations on the spark plasma sintering/synthesis process - II. Modeling of current and temperature distributions," (in English), *Materials Science and Engineering a-Structural Materials Properties Microstructure and Processing*, Article vol. 394, no. 1-2, pp. 139-148, Mar 2005.
- [30] N. Frage, S. Cohen, S. Meir, S. Kalabukhov, and M. P. Dariel, "Spark plasma sintering (SPS) of transparent magnesium-aluminate spinel," (in English), *Journal of Materials Science, Letter* vol. 42, no. 9, pp. 3273-3275, May 2007.
- [31] H. Yin, M. Christensen, N. Lock, and B. B. Iversen, "Zn migration during spark plasma sintering of thermoelectric Zn₄Sb₃," *Applied Physics Letters*, vol. 101, no. 4, Jul 23 2012, Art. no. 043901.
- [32] M. S. Song, S. M. Choi, W. S. Seo, J. Moon, and K. W. Jang, "Thermoelectric and mechanical properties of Zn₄Sb₃ polycrystals sintered by spark plasma sintering," (in English), *Journal of the Korean Physical Society*, Article vol. 60, no. 10, pp. 1735-1740, May 2012.
- [33] T. Zhang, K. Zhou, X. F. Li, Z. Q. Chen, X. L. Su, and X. F. Tang, "Reversible structural transition in spark plasma-sintered thermoelectric Zn₄Sb₃," (in English), *Journal of Materials Science*, Article vol. 51, no. 4, pp. 2041-2048, Feb 2016.
- [34] T. Tomida *et al.*, "Fabrication of 200 mm Diameter Sintering Body of Skutterudite Thermoelectric Material by Spark Plasma Sintering," (in English), *Journal of Electronic Materials*, Article; Proceedings Paper vol. 46, no. 5, pp. 2944-2949, May 2017.
- [35] B. A. Hunter and C. J. Howard, *Rietica*. Menai, Australia: Australian Nuclear Science and Technology Organization, 2000.
- [36] F. Laufek, J. Navratil, and V. Golias, "Synthesis and Rietveld refinement of skutterudite-related phase CoSn(1.5)Te(1.5)," (in English), *Powder Diffraction*, Article vol. 23, no. 1, pp. 15-19, Mar 2008.

- [37] F. Laufek and J. Navrátil, "Crystallographic study of ternary ordered skutterudite IrGe_{1.5}Se_{1.5}," *Powder Diffraction*, vol. 25, pp. 247-252, 2010.
- [38] L. T. Zhang, M. Tsutsui, K. Ito, and M. Yamaguchi, "Effects of ZnSb and Zn inclusions on the thermoelectric properties of beta-Zn₄Sb₃," (in English), *Journal of Alloys and Compounds*, Article vol. 358, no. 1-2, pp. 252-256, Aug 2003.
- [39] B. L. Pedersen and B. B. Iversen, "Thermally stable thermoelectric Zn₄(Sb)₃ by zone-melting synthesis," (in English), *Applied Physics Letters*, Article vol. 92, no. 16, p. 3, Apr 2008, Art. no. 161907.
- [40] Y. Mozharivskij, A. O. Pecharsky, S. Bud'ko, and G. J. Miller, "Promising thermoelectric material: Zn₄Sb₃ or Zn_{6-δ}Sb₅. Its composition, structure, stability, and polymorphs. Structure and stability of Zn_{1-δ}Sb," (in English), *Chemistry of Materials*, Article vol. 16, no. 8, pp. 1580-1589, Apr 2004.
- [41] G. J. Snyder, M. Christensen, E. Nishibori, T. Caillat, and B. B. Iversen, "Disordered zinc in Zn₄Sb₃ with phonon-glass and electron-crystal thermoelectric properties," (in English), *Nature Materials*, Article vol. 3, no. 7, pp. 458-463, Jul 2004.
- [42] E. Chalfin, H. X. Lu, and R. Dieckmann, "Cation tracer diffusion in the thermoelectric materials Cu₃Mo₆Se₈ and "beta-Zn₄Sb₃," (in English), *Solid State Ionics*, Article vol. 178, no. 5-6, pp. 447-456, Mar 2007.
- [43] H. Yin, B. L. Pedersen, and B. B. Iversen, "Thermal Stability of High Performance Thermoelectric beta-Zn₄Sb₃ in Argon," (in English), *European Journal of Inorganic Chemistry*, Article no. 17, pp. 2733-2737, Jun 2011.

Chapter 3. Effect of Single Metal Doping on the Thermoelectric Properties of SnTe

3-1. Abstract

SnTe, a lead-free chalcogenide-based material, shows the potential to achieve high thermoelectric performance. However, intrinsic Sn vacancies lead to low Seebeck coefficient and high electrical thermal conductivity and, thus, present a challenge for practical applications. Several reports have suggested that proper cation doping can adjust the charge carrier concentration and mobility in SnTe and increase its thermoelectric performance. This report presents a comparison study of different metallic dopants on SnTe and their effect on the microstructures, mechanical and thermoelectric properties. Doped SnTe ($\text{Sn}_{1-x}\text{A}_x\text{Te}$, A= Co, Ni, Zn, Ge, and $x = 0.01, 0.03, 0.05$) materials are prepared by melting-quenching synthesis followed by spark plasma sintering. X-ray powder diffraction analysis showed that the solubility of Co, Ni, and Zn in the structure is in a range from 0 to 0.01, however, Ge can be doped in higher amounts. The back-scattered electron images and elemental maps revealed that the CoTe, Ni_3SnTe_2 and ZnTe impurity phases precipitate on the grain boundaries in the SnTe matrix. Ge-doped samples have more uniform microstructures with a very few Ge-rich regions, which implies higher Ge solubility in agreement with X-ray results. The existence of impurity phases in the Co-, Ni-, Zn-doped samples yields lower lattice thermal conductivities without deterioration in charge transport properties, leading to higher ZT values relative to the pristine SnTe sample. Microhardness of the doped samples is also improved due to the crack growth suppression and crack branching.

3-2. Introduction

Owing to growing global demands for energy efficiency and conservation, green, safe and reliable energy conversion technologies are becoming highly desirable. Thermoelectric materials (TE) are of particular interest as they can scavenge waste heat and turn it into electric current by using the Seebeck effect. Promising TE materials display high Seebeck coefficient, S , high electrical conductivity, σ , and low thermal conductivity, k , whose values determine the dimensionless figure-of-merit $ZT = S^2\sigma T/k$ at a given

temperature T [1-3]. Lead chalcogenide PbQ ($Q = S, Se, \text{ and } Te$) compounds are among the promising thermoelectric materials as they possess high thermoelectric performance at mid-temperature ranges (600–900 K), and for this reason, they have long been studied for power generation applications [4-7]. For instance, recent studies on lead chalcogenides yielded $ZT \sim 2.0$ by applying band engineering, and microstructure control [5, 8-10]. However, new regulations for environmentally hazardous substances aim to limit the use of lead, and adoption of lead chalcogenides for thermoelectric power generators does not seem viable. For this reason, lead-free TE materials such as tin chalcogenides (SnQ) have attracted significant attention. Zhao et. al. has recently reported very high ZT of 2.6 at 900 K for $SnSe$ single crystals [11]. However, poor mechanical properties, as well as the anisotropic nature of $SnSe$ single crystals annihilates the feasibility of using them in real devices. On the other hand, thermoelectric properties of polycrystalline $SnSe$ is not as exciting as of its single crystalline analogue [12, 13]. Meanwhile, tin telluride ($SnTe$), another member of tin chalcogenides, has physicochemical properties very similar to $PbTe$; the same rock salt structure, narrow band gap, and similar band structure. Therefore, one can assume that TE properties of $SnTe$ can be improved by using the similar techniques applied to $PbTe$, such as the resonant level effect, band engineering, and nanostructuring [14-16].

However, $SnTe$ has its shortcomings; due to the intrinsic Sn vacancies, it possesses ultrahigh hole density ($>10^{21} \text{ cm}^{-3}$), leading to poor Seebeck coefficient, high thermal conductivity, and thus relatively low ZT values. Several studies have been conducted to suppress the hole concentration to a suitable level of ca. 10^{19} cm^{-3} through doping with the elements that are efficient electron donors in lead chalcogenides, such as Sb and Bi [17, 18]. However, the outcomes were not satisfactory. Instead, it has been reported that Sn self-compensation (i.e. extra Sn) can successfully diminish the Sn vacancies and bring down the hole carrier concentration, leading to a 50% enhancement in the ZT value for the $Sn_{1.03}Te$ sample [15]. While Sn self-compensation does reduce the hole concentration in $SnTe$, the resulting hole density is still relatively high and needs further optimization to achieve suitable TE performance.

A desirable band gap for a good thermoelectric material operating around 800 K is at least ~ 0.3 eV (or $6-10 k_B T$, where k_B is Boltzmann constant, and T is the operating temperature) according to the theoretical studies, but it can also be larger depending on the specific mechanism of electron scattering [19]. SnTe has band gaps (E_g) of ~ 0.18 and ~ 0.27 eV at room temperature and higher temperatures, respectively, which are smaller than the optimum values [15, 19, 20]. The small band gap of SnTe (smaller than that of PbTe) causes bipolar effects at high temperatures. Furthermore, the energy separation between the light hole and the heavy hole valence bands ($\Delta E_{V_{B_L-\Sigma}}$) is about 0.3-0.4 eV at 300 K, which is larger than that in PbTe [21, 22]. Therefore, SnTe has low S as a consequence of large $\Delta E_{V_{B_L-\Sigma}}$, which means heavy holes from the valence band do not contribute to charge carrier transport. Therefore, optimization of the electronic band structure of SnTe through the band engineering is needed, if SnTe were to be used at high temperatures. Using appropriate dopant elements, one can simultaneously increase the band gap and reduce the energy difference between the light-hole and heavy-hole bands. Tan et al. [15] demonstrated valence band engineering via isoelectronic doping of Sn with Cd. The Cd presence affects the electronic band structure through the convergence of the light-hole and heavy-hole valence bands, leading to a larger Seebeck coefficient [15, 23]. In addition, bipolar diffusion as a result of the very small band gap of pure SnTe causes low thermoelectric performance at elevated temperature, while Cd doping yields a larger band gap and better thermoelectric performance at high temperatures [15, 23]. As a result, a ZT value of ~ 0.96 was achieved at 823 K for the p-type $\text{SnCd}_{0.03}\text{Te}$ sample, a 60% improvement over the undoped sample [15]. Moreover, $\text{SnCd}_{0.03}\text{Te}$ with endotaxial CdS and ZnS nanoprecipitates displayed reduced lattice thermal conductivity while the power factor was preserved. The maximum ZT s of ~ 1.3 and ~ 1.1 was achieved at 873 K for CdS and ZnS added specimens, respectively [15]. Similar effects on the electronic band structure of SnTe were observed in Mg-, Mn-, Ca-doped samples [14, 24, 25].

To further investigate the TE properties of doped SnTe, we explored new cation-doped SnTe samples. To the best of our knowledge, very few systematic studies have been conducted on the TE properties of Co-, Ni-, Zn-, and Ge-doped SnTe phases.

3-3. Experimental procedure

Co (99.999 wt. %), Ni (99.995 wt.%), Zn (99.995 wt.%), Ge (99.995 wt.%), Tin (99.995 wt.%), and tellurium (99.999 wt.%) pieces were used for the synthesis without further purification. Initially, high-quality polycrystalline ingots of $\text{Sn}_{1-x}\text{A}_x\text{Te}$ ($x = 0-0.05$) were prepared through melting stoichiometric amounts of the starting elements in vacuum sealed silica tubes (10^{-3} Torr, 10 mm in diameter). The samples were slowly heated to 1273 K over 10 h, then soaked for 6 h, and then rapidly quenched in the ice-water mixture. The ingots were hand ground in an agate mortar and the powders were densified by spark plasma sintering at 600 °C with a uniaxial pressure of ~50 MPa for 5 minutes. The density of all sintered samples was determined using Archimedes' method, which gave values $\geq 96\%$ of the theoretical density. In order to measure thermoelectric properties, the samples were cut into pellets and bars ($2 \times 2 \times 10 \text{ mm}^3$) with a low speed saw.

X-ray diffraction (XRD) and energy dispersive spectroscopy (EDX) were employed to characterise the samples' crystallinity, homogeneity, chemical composition and elemental distributions. Powder XRD data were collected for $2\theta = 20-140^\circ$ on a PANalytical X'Pert Pro diffractometer with a linear X'Celerator detector and $\text{Cu-K}\alpha_1$ ($\lambda = 1.5406 \text{ \AA}$) radiation at room temperature. Sample powders were deposited on a zero-background silicon disc. The XRD data were refined by the Rietveld method using the Rietica program [26]. Microstructural analyses were done using scanning electron microscopy (SEM, Tescan Vega II LSU, USA) in both secondary and backscatter modes of imaging. The samples were prepared by hand polishing using 2400 SiC and 4000 SiC polishing papers.

Electrical conductivity and Seebeck coefficients were measured simultaneously under a He atmosphere from room temperature to 600 °C on a ULVAC-RIKO ZEM-3 instrument system. Pure SnTe, as the reference samples, were measured using two different ZEM-3 instruments in two different places, and the average amount is taken. Surfaces of each specimen were gently polished using 2400 SiC and 4000 SiC papers before measurements.

The thermal diffusivity, D , was directly measured from room temperature to 600 °C by using the laser flash diffusivity method of a Netzsch LFA-457 instrument. Square samples with the dimensions of $\sim 10 \times 10$ mm and ~ 1 mm thickness were used for the measurements. The temperature dependent heat capacity, C_p , was derived using a standard sample (pyroceram) in a LFA-457. The total thermal conductivity, κ_{total} , was calculated using the formula: $\kappa_{\text{total}} = DC_p\rho$, where ρ is the density.

Vickers microhardness was measured on the 5% doped samples using a diamond indenter on a commercial Zwick Roell ZHU 2.5 instrument, where the force applied was 2 N and the indent was kept for 10 s. The equation $H_v = 1.854 \times L/(2d)^2$ was used to determine the Vickers hardness values ($\text{kgf}\cdot\text{mm}^{-2}$), with L being the indentation load and $2d$ the diagonal length of the indentation. The uncertainty for the microhardness measurements is about 5%.

3-4. Results and Discussions

Figure 3-1 demonstrates the powder XRD patterns of the Co, Ni, Zn, and Ge-doped $\text{Sn}_{1-x}\text{A}_x\text{Te}$ bulk samples after SPS along with the Rietveld refinement results for the 5% doped samples. The main Bragg reflections of all the samples fit the face-centered cubic (fcc) structure of SnTe (space group $\text{Fm}\bar{3}\text{m}$). The 1% doped samples are pure within the X-ray detection limits. Rietveld refinements show an excellent agreement between the experimental spectra and the theoretical patterns generated. When the dopant fractions are above 1 %, second phases can be clearly observed. The amount of impurities calculated from the Rietveld refinement is summarized in Table 3-1. When dopant elements are introduced on the Sn-site, the lattice parameters are expected to decrease since the cationic radii of the dopants are smaller than that of Sn^{2+} (Ge^{2+} 0.65 Å [27, 28] < Co^{2+} 0.70 Å \cong Ni^{2+} 0.70 Å < Zn^{2+} 0.74 Å < Sn^{2+} 0.93 Å)[29]. Indeed, there is a slight peak shift towards higher 2θ for Co-, Ni-, Zn- and Ge-doped samples, which proves successful substitutions on the Sn site (Table 3-1).

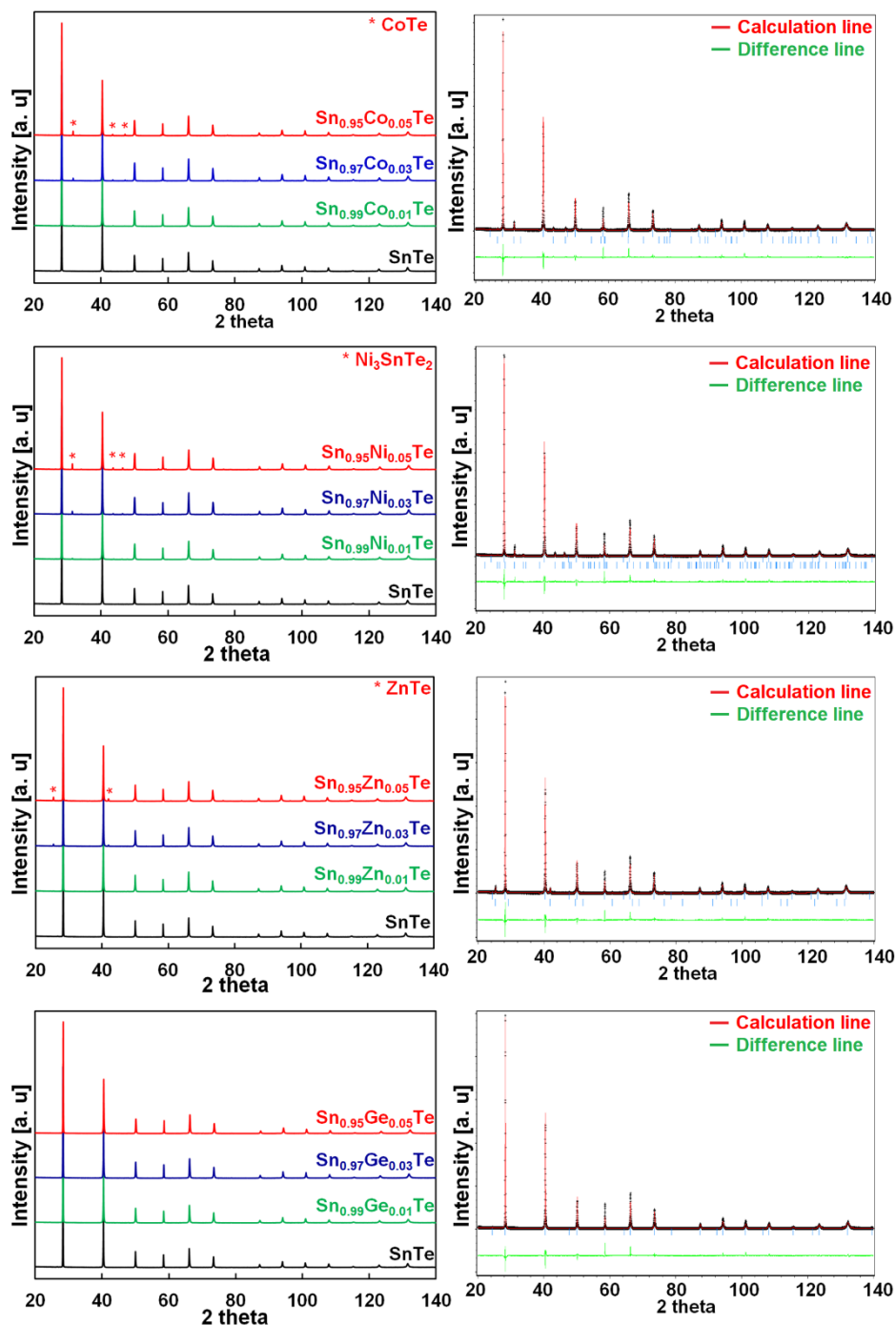


Figure 3-1. (a, c, e, g) Powder XRD patterns of the $\text{Sn}_{1-x}\text{A}_x\text{Te}$ samples doped with Co, Ni, Zn, and Ge from 1 to 5%. (b, d, f, h) Rietveld refinement results for the 5% doped samples. The impurity phases are very well matched with CoTe, Ni_3SnTe_2 and ZnTe for the Co-, Ni-, and Zn-doped samples, respectively.

The refined pattern for the 5% Ge-doped sample shows no detectable impurity peaks.

The 3 and 5% Co-, Ni-, and Zn-doped samples contain CoTe, Ni₃SnTe₂, and ZnTe impurities, respectively, and their fraction increases with the doping level (Table 3-1). The lattice parameters combined with the phase analysis suggest that solubility limits for Co and Ni are about 1%. For the Zn case, the lattice parameters are not a reliable guide, however, the phase analysis suggests similar solubility. For the Ge substitution, the lattice parameter decreases gradually to 5 at. % of Ge and nearly no impurities are detected (Table 3-1).

Table 3-1. Lattice parameters and weight percentages of secondary phases in the Co-, Ni, Zn-, Ge-doped samples after SPS.

Sample	SnTe	Co-doped			Ni-doped			Zn-doped			Ge-doped		
		1%	3%	5%	1%	3%	5%	1%	3%	5%	1%	3%	5%
Lattice parameter	6.3234(1)	6.3198(1)	6.3202(1)	6.3211(1)	6.3164(1)	6.3140(1)	6.3151(1)	6.3222(1)	6.3212(1)	6.3217(1)	6.3186(1)	6.3117(1)	6.3047(1)
Secondary phase wt.%	0	0.23(2)	0.80(2)	1.36(2)	0.34(4)	1.08(3)	1.88(4)	0.47(5)	1.35(3)	2.36(4)	0	0	<0.1*

* A very small impurity peak is observed at $2\theta \approx 27.3$. It can be attributed to elemental Ge.

It has been demonstrated that different elements have different solubility behaviour in SnTe, however, the solubility limits for Co, Ni and Zn are much lower than those observed for other dopants [14, 24, 25, 30]. Wu et. al. [25] reported on up to 13% solubility of Mn in SnTe (on the Sn site). The authors observed that the (200) peak shifts to larger angles up to 13% of Mn and then to a lower angle for higher Mn concentrations (Mn²⁺ radius is 0.66 Å and that of Sn²⁺ is 0.93 Å). Banik et. al. [31] observed a similar effect in the Sb-doped SnTe, where an increase in the Sb concentration up to $x = 0.12$ in Sn_{1-x}Sb_xTe resulted in smaller lattice parameters. However, past $x = 0.12$, the lattice parameters of Sn_{1-x}Sb_xTe started to increase and this was accompanied by the formation of Sn_mSb_{2n}Te_{3n+m} intergrowth nanostructures in the SnTe matrix [31]. In the current work, similar lattice behaviour is observed in the Co-, Ni-, and Zn-doped samples.

Scanning electron microscope (SEM) and backscattered electron (BSE) images (Figure 3-2 – 3-5) were taken for 5% doped samples. Significant differences between the bright and dark contrast were observed in the Co, Ni, and Zn -doped specimens. The Co-, Ni-, and Zn-containing impurities precipitated primarily on the grain boundaries, additionally, the impurities displayed different precipitation patterns at the grain boundaries. Presence of secondary phases agrees with the XRD results that showed two phases for doping levels above 1%. However, the secondary electron (SE) and backscattered electron (BSE) images for the Ge-doped sample are different from those with other dopants. The distribution of Ge is almost homogeneous on a microscale, showing very few regions rich in Ge. When the Ge amount is below 5 %, the samples can be assumed in a single phase, in the agreement with the XRD results. The formation of impurities can have beneficial effects on the lattice thermal conductivity, and this relationship is discussed below.

Figure 3-6 shows the temperature-dependent electrical conductivity $\sigma(T)$ of the $\text{Sn}_{1-x}\text{A}_x\text{Te}$ sample. The $\sigma(T)$ of all samples decreases with increasing temperature, which is representative of heavily doped semiconductors. Overall, the electrical conductivities of $\text{Sn}_{1-x}\text{A}_x\text{Te}$ samples reach 7130–1130 $\text{S}\cdot\text{cm}^{-1}$, 7300–1220 $\text{S}\cdot\text{cm}^{-1}$, 7710–870 $\text{S}\cdot\text{cm}^{-1}$, 7270–860 $\text{S}\cdot\text{cm}^{-1}$ and for the Co-, Ni-, Zn-, and Ge-doped samples, respectively, within the measured temperature range. For all dopants, the electrical conductivity of the 1%-doped samples is higher than that of SnTe, which is likely due to higher carrier density. For the Zn- and Ge-containing samples, the conductivity generally decreases for the dopant concentrations above 1%. For the Ni-doped samples, electrical conductivity rises slightly as the Ni amount increases from 1% to 3% (Figure 6(b)). This can be attributed to the formation of the Ni_3SnTe_2 impurity, which reduces the overall Sn/Te ratio and thus increases the charge carrier concentration in the SnTe matrix. With increasing temperature, the electrical conductivity of 1, 3 and 5% doped samples converges and remains almost similar at higher temperatures.

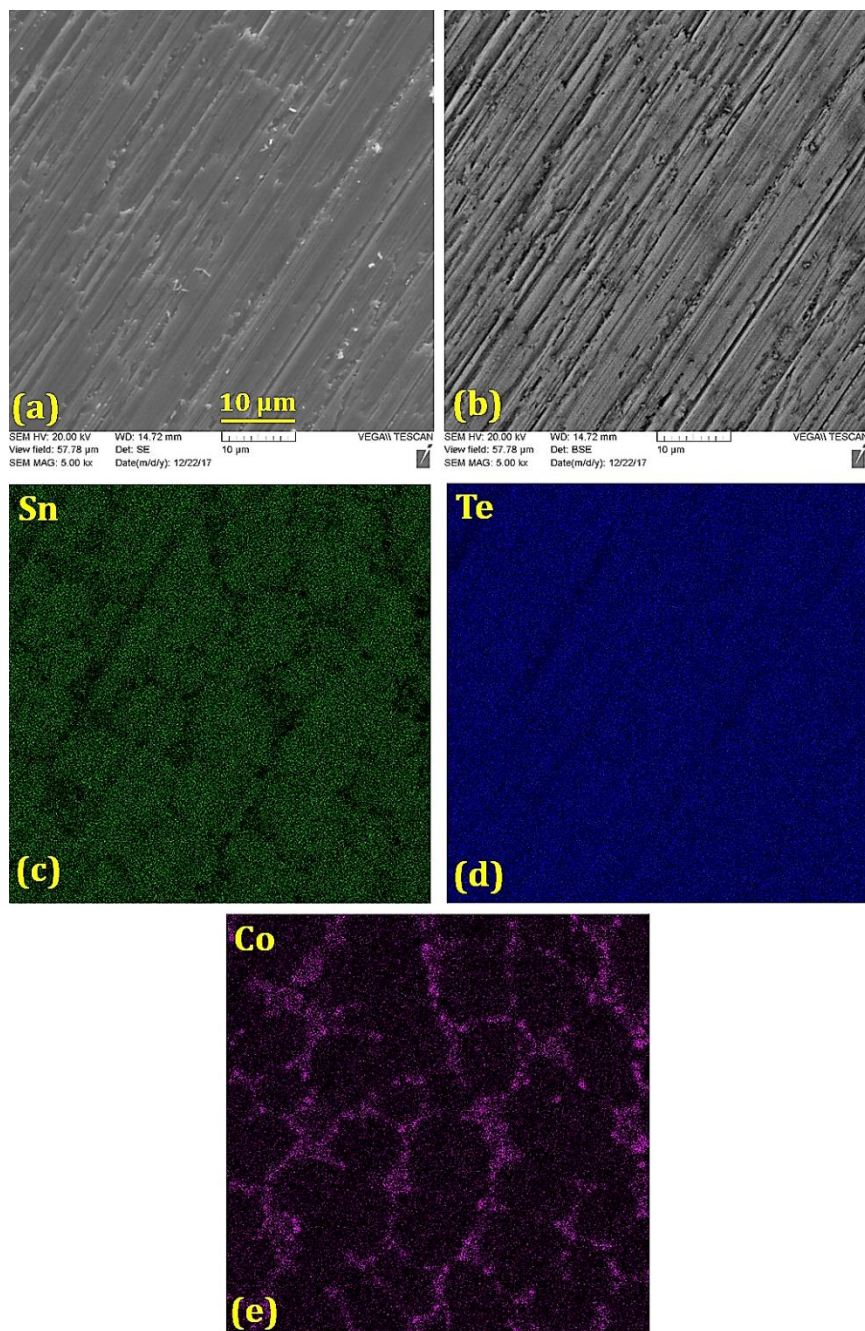


Figure 3-2. (a) Secondary electron image, (b) back-scattered electron image and (c-e) elemental mappings of Sn, Te and Co in the polished $\text{Sn}_{0.95}\text{Co}_{0.05}\text{Te}$ sample prepared via SPS. Co-richer precipitates are found on the grain boundaries with the average grain size of $\sim 10 \mu\text{m}$. Lack of Sn on the grain boundaries and uniform Te distribution confirms the formation of CoTe on the grain boundaries, in agreement with the XRD results (Figure 1 (a) and (b)).

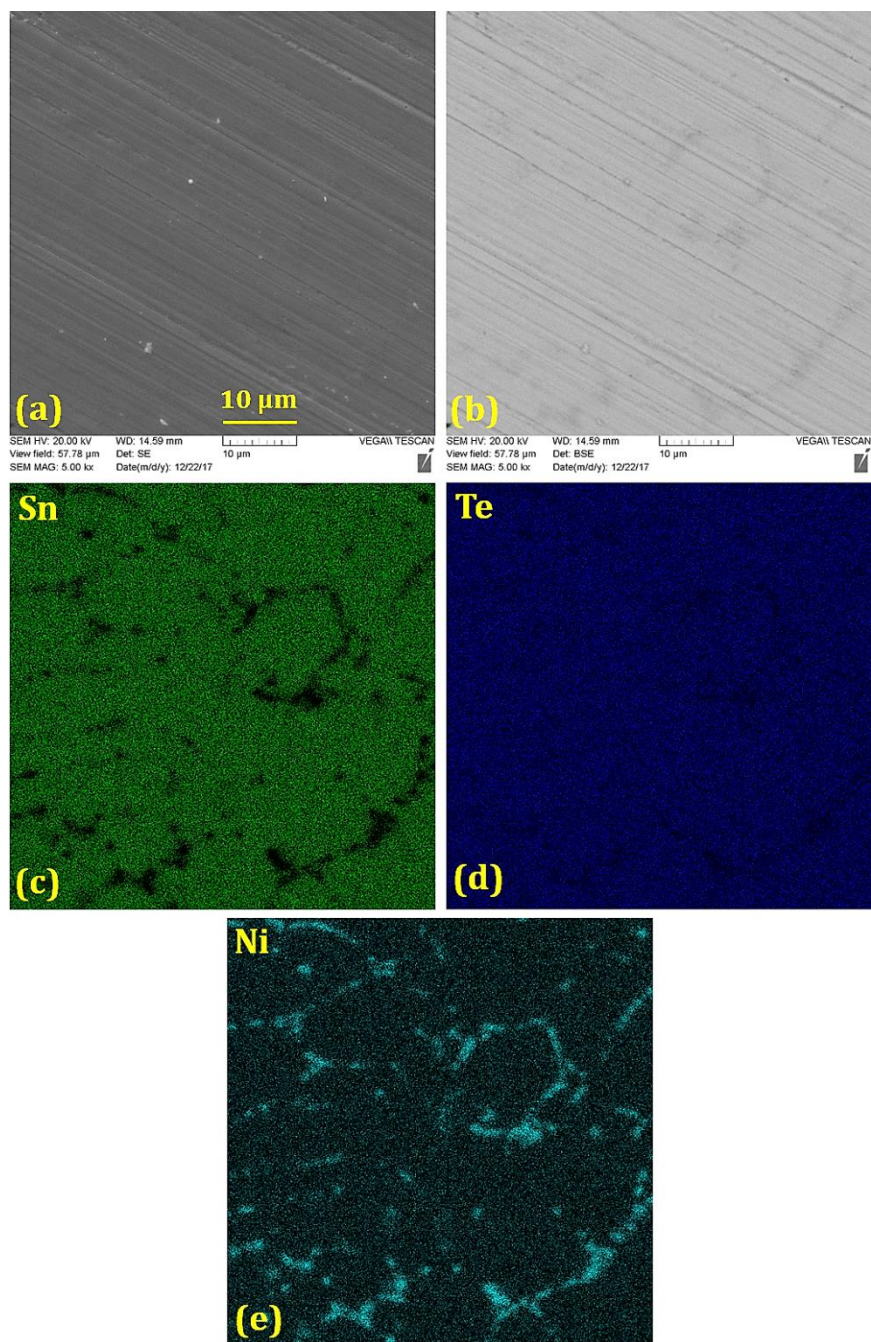


Figure 3-3. (a) Secondary electron image, (b) back-scattered electron image and (c-e) elemental mappings of Sn, Te and Ni in the polished $\text{Sn}_{0.95}\text{Ni}_{10.05}\text{Te}$ sample prepared via SPS. A Ni-richer phase precipitates on the grain boundaries and within the grains with the average grain size $\leq 10 \mu\text{m}$. Significant reduction in the Sn signal and slight reduction in the Te signal on the grain boundaries is consistent with the formation of Ni_3SnTe_2 as identified in the XRD data (Figure 1 (g) and (h)).

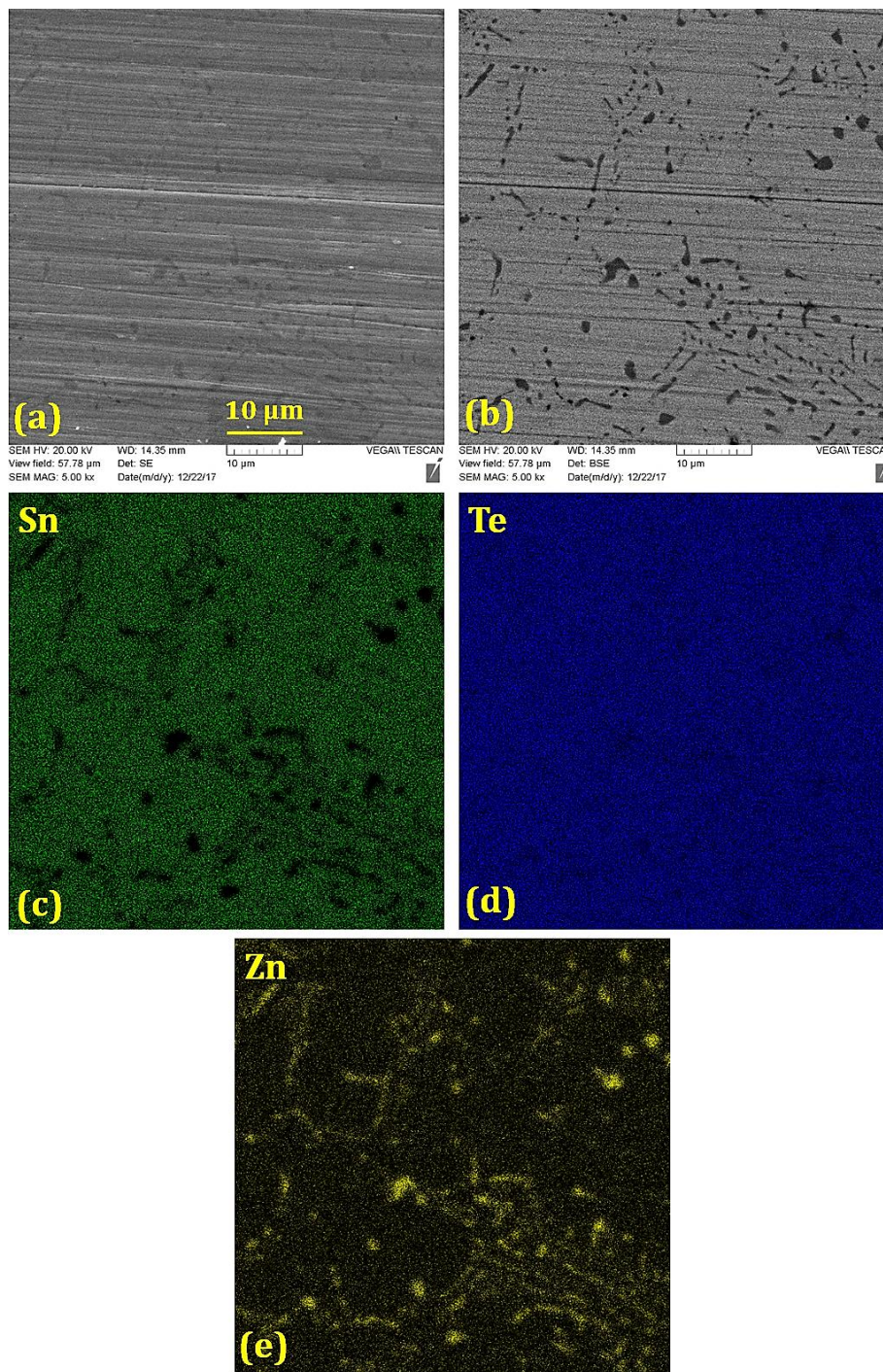


Figure 3-4. (a) Secondary electron image, (b) back-scattered electron image and (c-e) elemental mappings of Sn, Te and Zn in the polished $\text{Sn}_{0.95}\text{Zn}_{0.05}\text{Te}$ sample prepared via SPS. Sn is absent in the Zn-rich areas, while the Te distribution is uniform throughout the sample. The elemental mapping supports the formation of the ZnTe impurity, as witnessed from the XRD data (Figure 1 (c) and (d)).

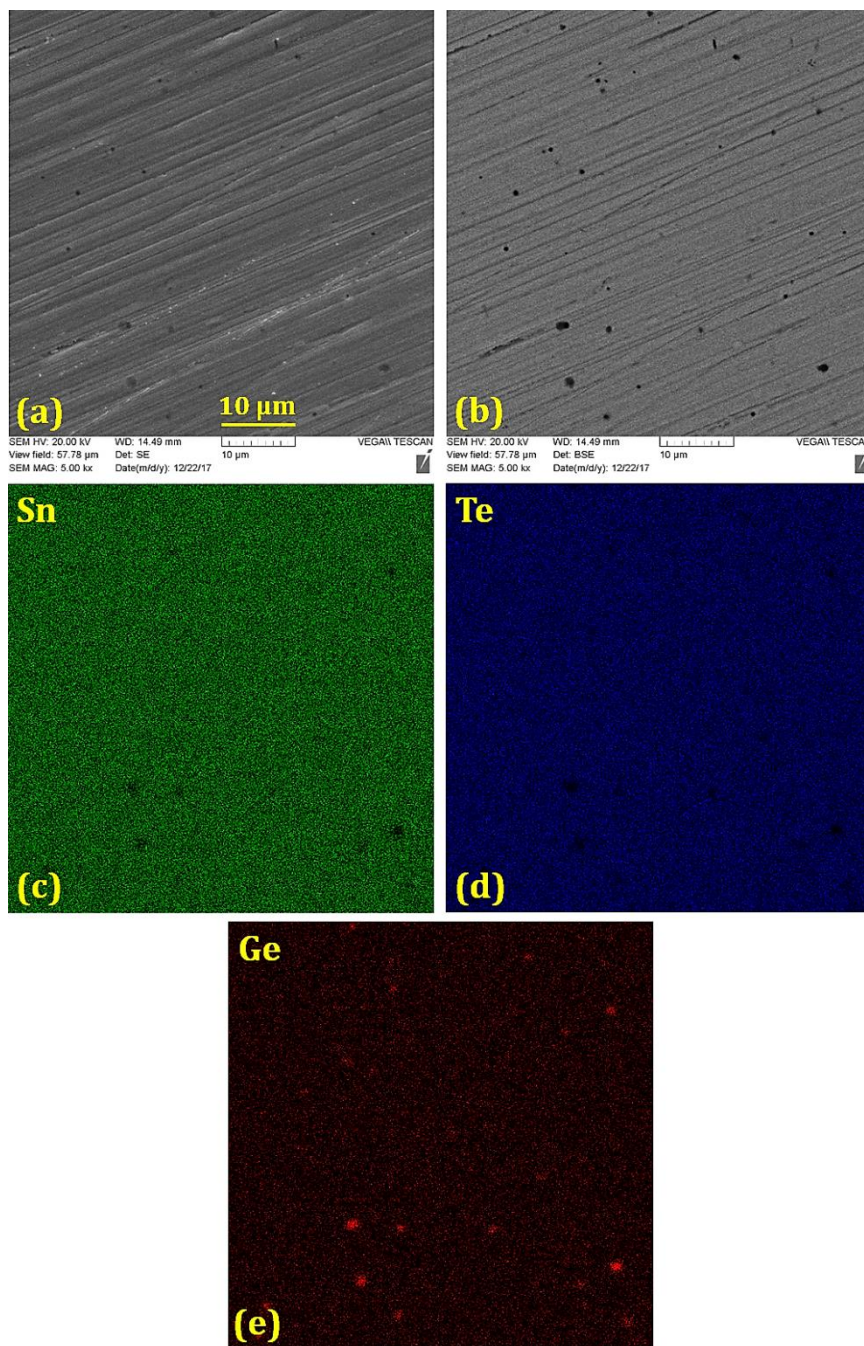


Figure 3-5. (a) Secondary electron image, (b) back-scattered electron image and (c-e) elemental mappings of Sn, Te and Ge in the polished $\text{Sn}_{0.95}\text{Ge}_{0.05}\text{Te}$ sample prepared via SPS. Ge distribution is almost uniform with very few Ge rich regions smaller than $1\mu\text{m}$. Sn and Te are deficient in the Ge-rich regions. The Ge-rich regions are not detected in the XRD patterns due to their small size and numbers

(Figure 1 (e) and (f)).

If we treat the dopant substitutions on the Sn site as an isovalent one, the carrier concentration should remain unchanged upon doping. In general, this is true as the electrical conductivity of all doped samples is relatively close to that of the pristine one (Figure 3-6). However, almost all 1% doped samples have a slightly higher electrical conductivity compared to the pristine sample suggesting an increased number of charge carriers. This observation is in an agreement with the literature results, which indicate that Sn vacancies can be induced by limited doping on the Sn site, leading to an increase in the hole concentration [29]. Doping above 1% in our samples does not change the charge carrier concentration but instead introduces more impurities/defects, leading to lower carrier mobility and conductivity. Similar effects were reported for Ag-doped SnTe specimens, where electrical conductivity decreased because of the increased charge carrier scattering by Ag-doping in the SnTe matrix [29].

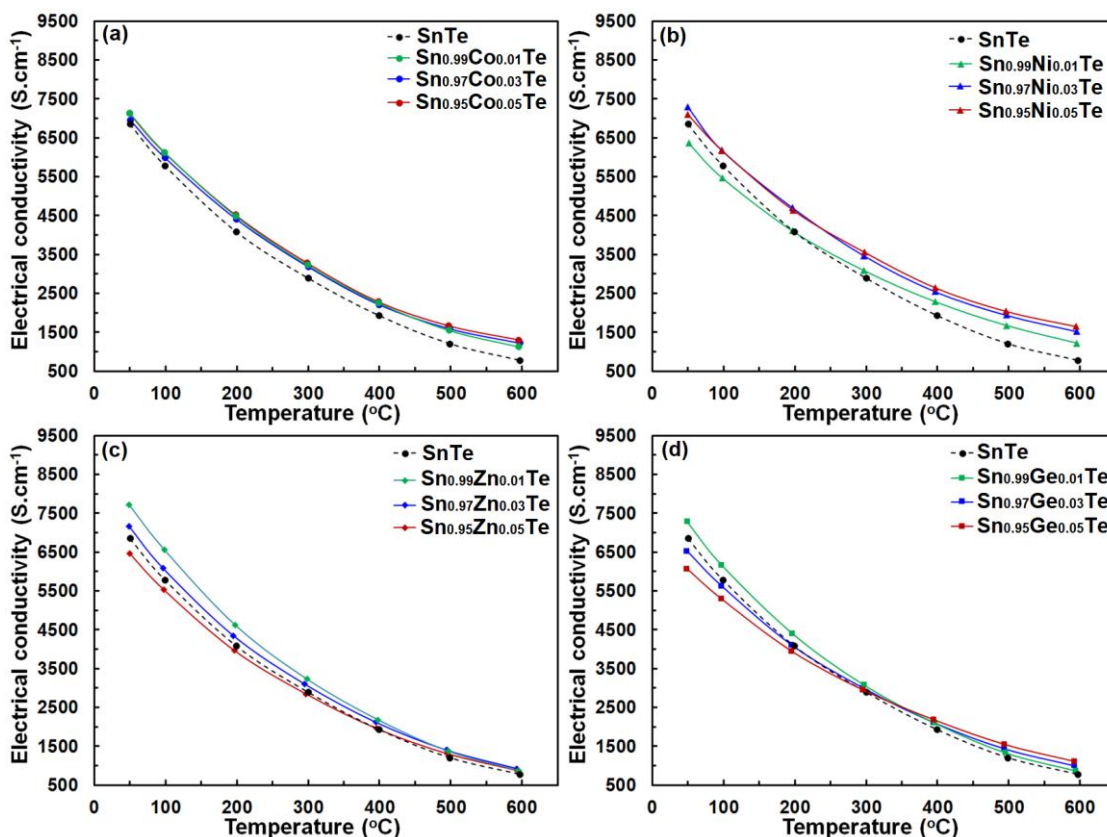


Figure 3-6. Temperature-dependent electrical conductivity for (a) $\text{Sn}_{1-x}\text{Co}_x\text{Te}$, (b) $\text{Sn}_{1-x}\text{Zn}_x\text{Te}$, (c) $\text{Sn}_{1-x}\text{Ge}_x\text{Te}$, and (d) $\text{Sn}_{1-x}\text{Ni}_x\text{Te}$. All samples demonstrate metallic-type behaviour for electrical conductivity.

The Seebeck coefficient, S , for all $\text{Sn}_{1-x}\text{A}_x\text{Te}$ sample is positive (Figure 3-7), indicating p -type conductivity. Changes in S upon doping are in general agreement with changes in $\sigma(T)$; i.e. a larger charge carrier concentration yields higher conductivity but lower thermopower. Additionally, for a given dopant, the Seebeck coefficient and its temperature behaviour are similar for different dopant levels. Interestingly, the room temperature Seebeck coefficients of the Co- and Ni-doped samples are visibly higher than for the pristine sample despite their higher electrical conductivity, which is contradictory to the typical behaviour expected for a degenerate semiconductor.

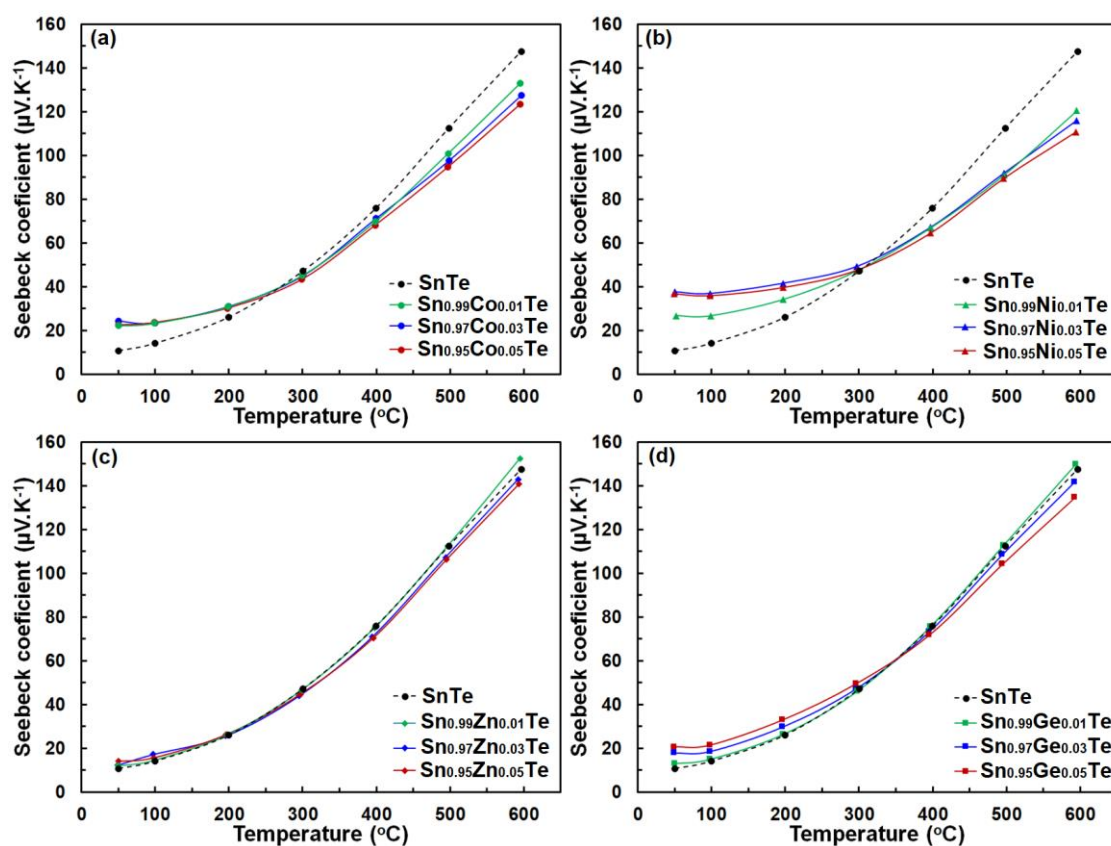


Figure 3-7. Temperature-dependent Seebeck coefficient of pure SnTe in comparison with (a) $\text{Sn}_{1-x}\text{Co}_x\text{Te}$, (b) $\text{Sn}_{1-x}\text{Zn}_x\text{Te}$, (c) $\text{Sn}_{1-x}\text{Ge}_x\text{Te}$, and (d) $\text{Sn}_{1-x}\text{Ni}_x\text{Te}$. Samples with different dopants display thermopower values close to that of pure SnTe, except for the Ni-doped samples.

However, the thermopower of the Co- and Ni-doped samples becomes lower at higher temperatures. While we cannot explain the relative thermopower values, the steeper slope for the SnTe phase might be attributed to the energy of the two nondegenerate valence bands, light- and heavy-hole ones [15, 32]. It appears that the Fermi level in pure SnTe is closer to the to the heavy-hole band, which yields a steeper increase in thermopower. Carriers excited by the heavy-hole band affect the Seebeck coefficient predominantly at high temperatures [33, 34]. In the case of the Co- and Ni-doped samples, the opposite is true and light holes dictate the thermopower behaviour. The heavy hole band contribution in the high-temperature properties of Sn_{1-x}Te was confirmed by Tan et al [15] through temperature dependent Hall measurement.

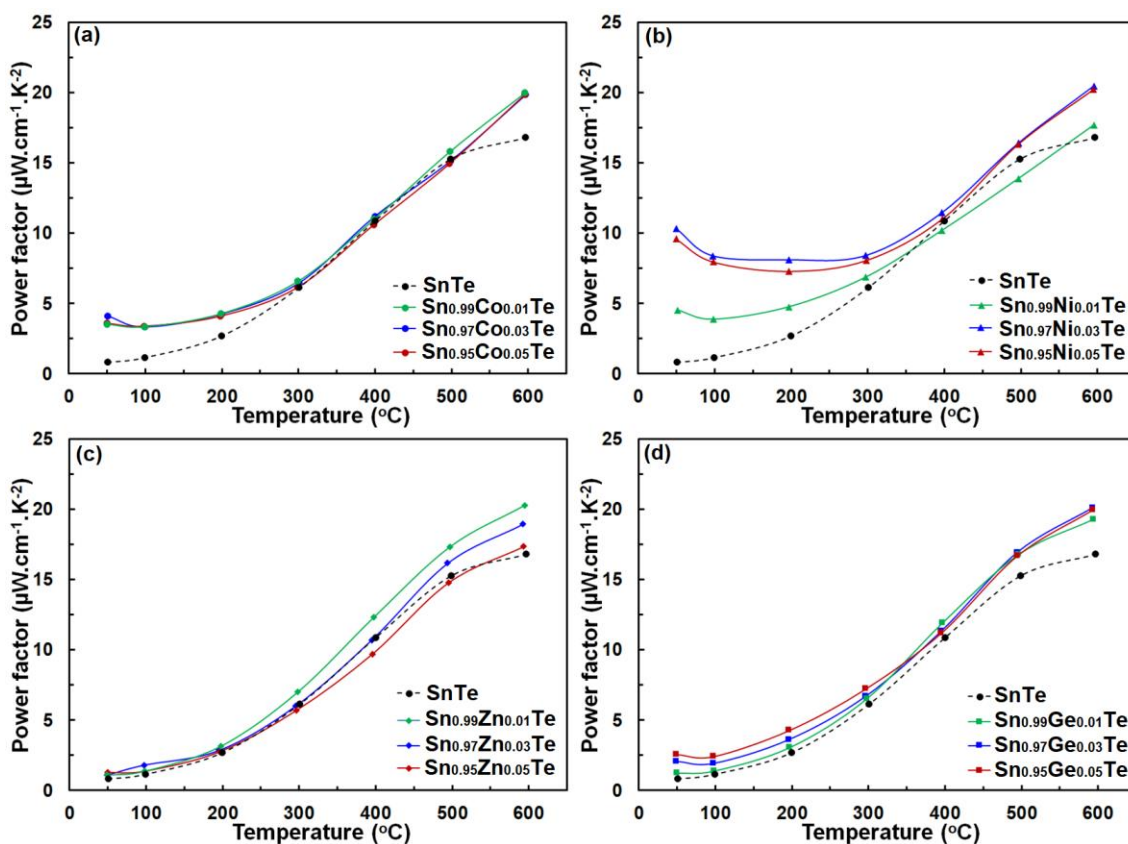


Figure 3-8. Temperature dependent power factor of (a) $\text{Sn}_{1-x}\text{Co}_x\text{Te}$, (b) $\text{Sn}_{1-x}\text{Zn}_x\text{Te}$, (c) $\text{Sn}_{1-x}\text{Ge}_x\text{Te}$, and (d) $\text{Sn}_{1-x}\text{Ni}_x\text{Te}$ in comparison with the pure SnTe. Doped samples possess increased power factors, especially at high temperatures.

Power factors for the pristine and doped samples are depicted in Figure 3-8. The pure SnTe has a power factor of $\sim 17 \mu\text{W cm}^{-1} \text{K}^{-2}$ at 300 °C, which is in good agreement with the literature data [14, 24, 30, 31]. Overall, power factors of doped samples ($\text{Sn}_{1-x}\text{A}_x\text{Te}$) are higher than that of the pristine one, mainly due to their higher electrical conductivity.

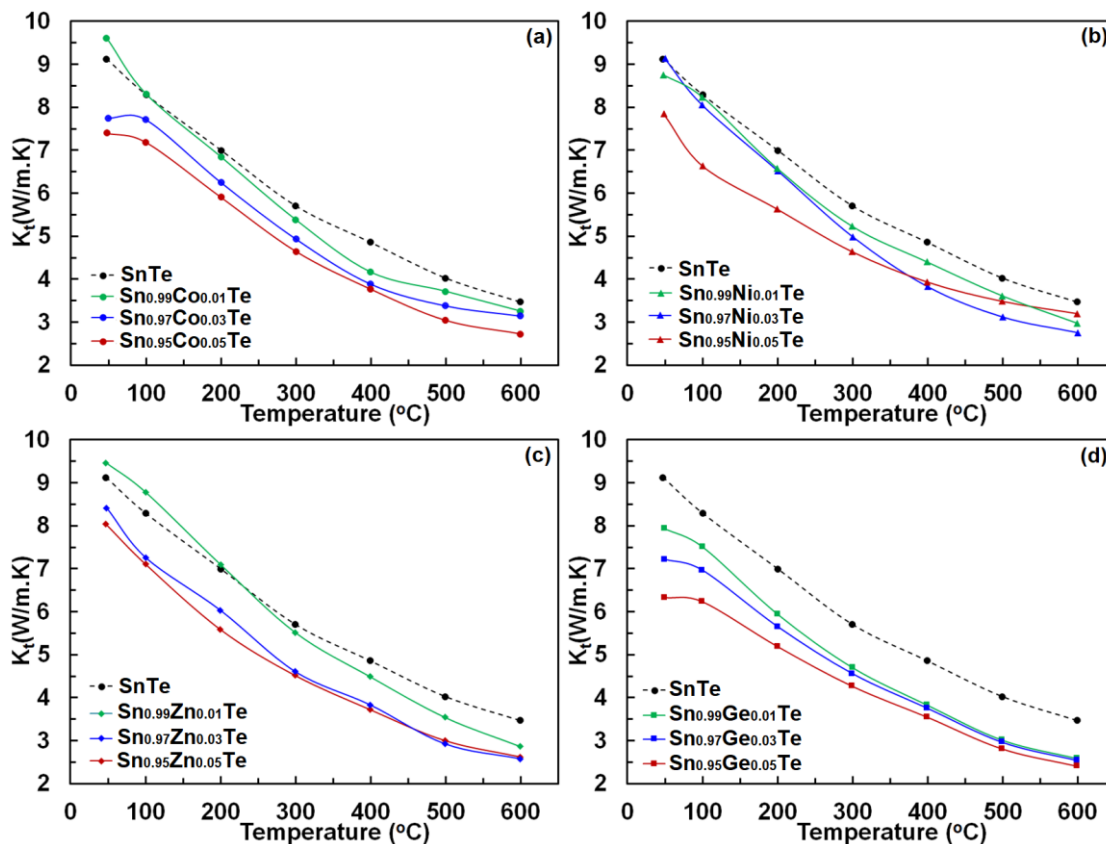


Figure 3-9. Total thermal conductivity, κ_{total} , of (a) $\text{Sn}_{1-x}\text{Co}_x\text{Te}$, (b) $\text{Sn}_{1-x}\text{Zn}_x\text{Te}$, (c) $\text{Sn}_{1-x}\text{Ge}_x\text{Te}$, and (d) $\text{Sn}_{1-x}\text{Ni}_x\text{Te}$ in comparison with pure SnTe as a function of temperature.

Thermal conductivities of the $\text{Sn}_{1-x}\text{A}_x\text{Te}$ samples are presented in Figure 3-9. All thermal conductivities decrease with increasing temperature and doping concentrations. Thermal conductivity contains electronic κ_e and lattice thermal conductivity κ_{lat} ; $\kappa_t = \kappa_e + \kappa_{\text{lat}}$. The electronic part, κ_e , can be estimated from the Wiedemann–Franz law ($\kappa_e = L\sigma T$), where L , σ , and T are the Lorenz number, electrical conductivity, and absolute temperature, respectively. The Lorenz number at a given temperature can be approximated from the experimental Seebeck coefficient according to [35]:

$$L = 1.5 + \exp \left[\frac{-|S|}{116} \right] \quad (1)$$

Table 3-2 summarizes the calculated Lorenz number as well as electronic and lattice thermal conductivities for the pristine and 5% doped samples at 50 and 600 °C. Since electrical conductivities of the doped samples are close to that of the undoped one, their electronic thermal conductivities at given temperatures are almost identical. However, the lattice thermal conductivities of the $\text{Sn}_{1-x}\text{A}_x\text{Te}$ samples are lower than that of the undoped one. This decrease can be associated with the higher phonon scattering due to the higher impurity concentrations upon doping. The thermal conductivity values are similar to those in the literature [14, 24, 30, 31].

Table 3-2. Room and high temperature total thermal conductivity κ_t , Lorenz number, electronic and lattice thermal conductivity for the pristine and 5% Co-, Ni-, Zn-, and Ge-doped samples.

Sample	Temperature (°C)	κ_t ($\text{Wm}^{-1}\text{K}^{-1}$)	L ($\times 10^{-8} \text{W}\Omega\text{K}^{-2}$)	κ_e ($\text{Wm}^{-1}\text{K}^{-1}$)	κ_{lat} ($\text{Wm}^{-1}\text{K}^{-1}$)
Pristine	50	9.12	2.41	5.34	3.78
	600	3.47	1.78	1.20	2.26
5% Co	50	7.40	2.32	5.35	2.05
	600	2.72	1.84	2.09	0.63
5% Ni	50	7.84	2.23	5.11	2.73
	600	3.20	1.88	2.71	0.49
5% Zn	50	8.04	2.39	4.98	3.05
	600	2.62	1.80	1.37	1.25
5% Ge	50	6.33	2.34	4.57	1.76
	600	2.41	1.81	1.74	0.67

The order of the lattice thermal conductivities of $\text{Sn}_{1-x}\text{A}_x\text{Te}$ at room temperature is: pristine > Zn-doped > Ni-doped > Co-doped > Ge-doped samples. It worth mentioning that the Ge-doped sample is very homogeneous, but the Co-, Ni- and Zn-doped samples have significant intergrain impurity precipitates (Figure 3-2 – 3-5). The sequence becomes pristine > Zn-doped > Ge-doped > Co-doped > Ni-doped samples at the highest temperature, indicating that precipitates on grain boundaries become more effective in scattering phonons at higher temperatures. Remarkably, the substitution of 5% Co, Ge, and Ni decreases

the lattice thermal conductivity to the point, where it is close to the amorphous limit at high temperature ($\kappa_{\text{lat}} \sim 0.4-0.5$) [21, 36].

As mentioned above, the difference in the thermal conductivity between the doped and pristine SnTe samples can be rationalized in terms of the microstructure. Generally, the thermal conductivity is highly sensitive to the precipitates at the grain boundaries, whereas the electrical conductivity and Seebeck coefficient are less. The 5% Co-, Ni- and Zn-doped samples have slightly different lattice thermal conductivities. This may stem from the different sizes of the CoTe, Ni₃SnTe₂, and ZnTe precipitates as well as their different distribution patterns. Similar reductions in the lattice thermal conductivities have been reported for Ga-, Mn-, Ca-, and Cu-doped SnTe due to the strong phonon scattering produced by the formation of GaTe, MnTe, CaTe, Cu₂Te impurities, respectively [14, 24, 25, 30, 36]. Analogous behaviour was also observed for CdS/ZnS second phases introduced into the SnTe samples. Tan et al [15] composited SnCd_{0.03}Te with endotaxial CdS and ZnS nanoscale precipitates to reduce the lattice thermal conductivity without affecting the power factor. These nanostructures formed point defects via integrating Cd or Zn atoms into the matrix at high temperatures with minimal influence on both the carrier mobility and the band gap of SnTe, thus enhancing the high-temperature thermoelectric performance.

In comparison to the Co-, Ni- and Zn-doped samples, the Ge-doped ones appear to have a different mechanism for phonon scattering. Ge is nearly uniformly distributed within the matrix with very few Ge-rich regions smaller than 1 μm . Lee et. al. [29] found a significant reduction in κ_{lat} due to Sn defects induced by doping, and the same might be happening in the Ge-doped samples here. There is also the possibility of formation of nanoclusters embedded in the structure, causing further lattice thermal conductivity reduction. However, the validity of this idea can only be verified with future TEM studies.

Figure 3-10 illustrates lattice thermal conductivities of the Co-, Ni- and Ge-doped SnTe samples (result for the Zn-doped sample are not shown as it has higher lattice thermal conductivity) in comparison with other singly doped SnTe compounds [14, 15, 17, 24, 25, 36-40]. It is apparent that the current dopants yield a significant reduction in the lattice thermal conductivity ($0.6-0.5 \text{ W}\cdot\text{m}^{-1}\cdot\text{K}^{-1}$ at 600 °C K) and bring it close

to the amorphous limit of κ_{lat} (0.4-0.5) [41]. However, both electronic thermal conductivities and low-temperature lattice thermal conductivities are still high, and further reductions are necessary to optimize the TE performance of the Co-, Ni-, Zn- and Ge-doped SnTe samples.

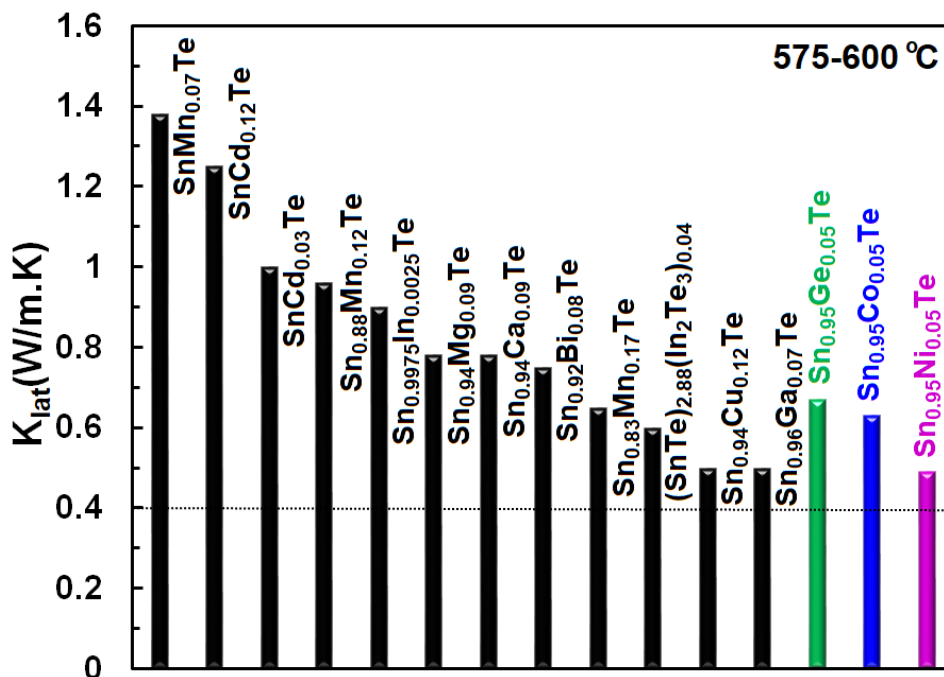


Figure 3-10. Comparison of the lattice thermal conductivity for different singly-doped SnTe samples [14, 15, 17, 24, 25, 36-40] at 575-600 °C. The lattice thermal conductivities of our Co-, Ni-, and Ge-doped samples are comparable to the lowest κ_{L} values reported for SnTe so far.

The ZT values as a function of temperature for the pristine and doped samples are presented in Figure 3-11. The Maximum ZT values of 0.63, 0.65, 0.64, and 0.72 are achieved for the Sn_{0.95}Co_{0.05}Te, Sn_{0.97}Ni_{0.03}Te, Sn_{0.97}Zn_{0.03}Te, and Sn_{0.95}Ge_{0.05}Te specimens at 600 °C, respectively. All doped samples show higher ZT values than that of the pure sample mostly due to decreases in their thermal conductivities. These results suggest that the current dopants can successfully improve the thermoelectric performance of SnTe. Moreover, Sn_{0.95}Co_{0.05}Te, Sn_{0.97}Ni_{0.03}Te, Sn_{0.97}Zn_{0.03}Te, and Sn_{0.95}Ge_{0.05}Te display 142, 159, 144, and 163% enhancements of the average figure of merit, ZT_{ave} (average of all ZT values from room temperature to 600 °C) in comparison with the pure SnTe (Figure 3-12).

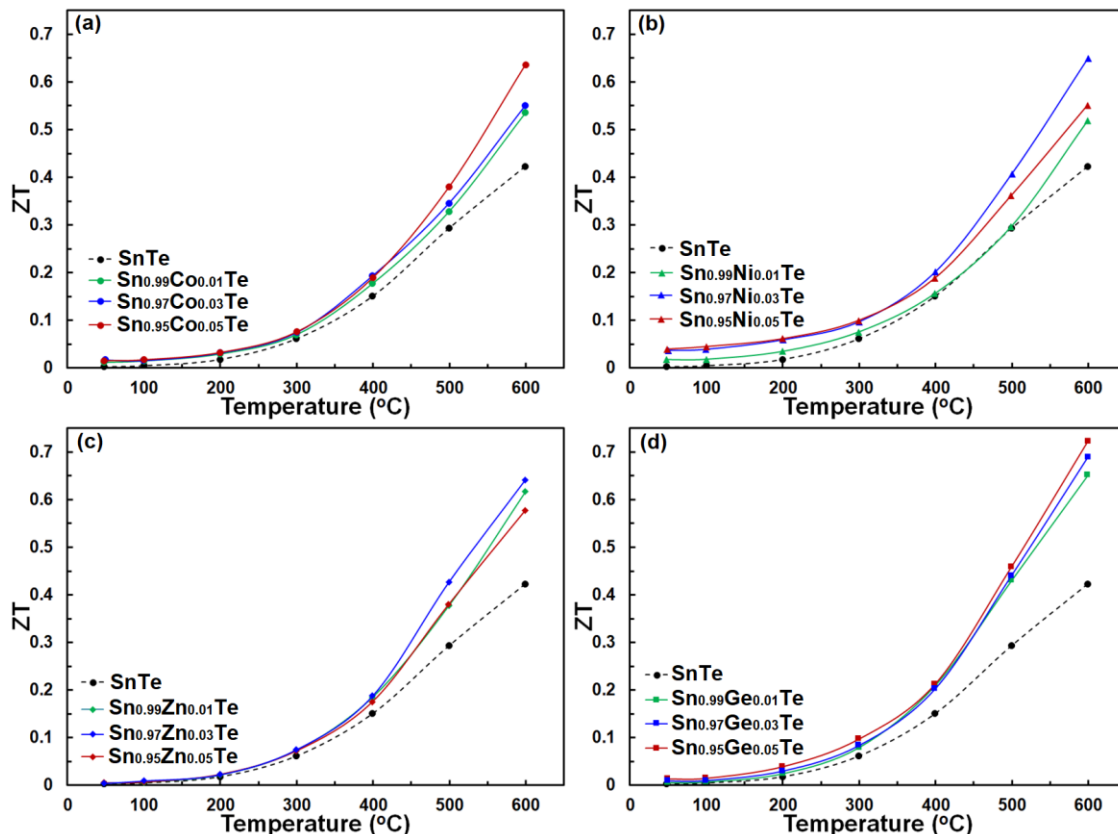


Figure 3-11. the dimensionless thermoelectric figure of merit, ZT , of (a) $\text{Sn}_{1-x}\text{Co}_x\text{Te}$, (b) $\text{Sn}_{1-x}\text{Zn}_x\text{Te}$, (c) $\text{Sn}_{1-x}\text{Ge}_x\text{Te}$, and (d) $\text{Sn}_{1-x}\text{Ni}_x\text{Te}$ in comparison with the pure SnTe from room temperature to 600 °C. All doped samples exhibit ZT values higher than that of the pure sample, especially at high temperatures.

Mechanical properties are vital for thermoelectric application as well. The material should be strong enough to withstand thermal cycling, thermal shock, machining, etc. in order to be used in large-scale device applications. Vickers microhardness indentation method has been used to measure the mechanical properties of the pristine and 5% doped samples (Figure 3-13). Overall, the rigidity of the doped materials is increased compared with the pure one. It is known that a pure SnTe material intrinsically contains Sn vacancies, which diminishes the mechanical strength. However, suitable dopants, leading to fewer Sn vacancies, increase the rigidity of the material. This effect was observed in the GeTe compounds, where Bi doping improved mechanical properties through Ge vacancy reduction [42]. Furthermore, crack growth suppression and crack branching are other two possible mechanisms contributing to the rigidity. Both can

be induced by dopants, which reduce the energy of the cracks and stop the crack propagation inside the sample. Examples of crack growth suppression and crack branching are shown in Figure 3-13. We believe these two mechanisms are dominant in the Co-, Ni-, and Zn-doped samples, while the reduction in the Sn vacancies can be instrumental in the Ge-doped one.

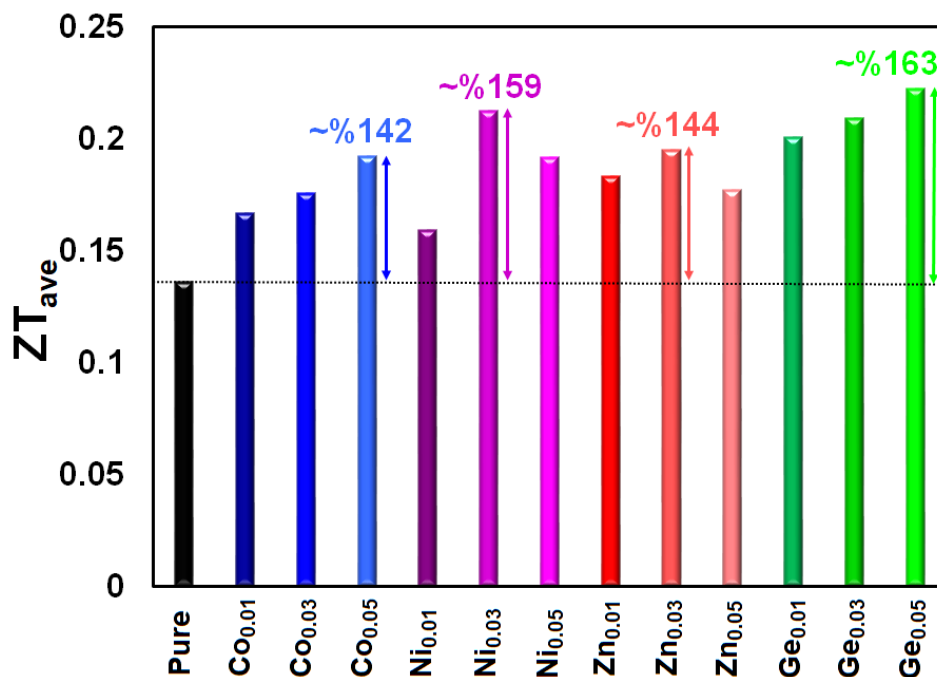


Figure 3-12. Average of the dimensionless thermoelectric figure of merit, ZT_{ave} (average of all ZT values from room temperature to 600 °C), of $Sn_{1-x}Co_xTe$, $Sn_{1-x}Zn_xTe$, $Sn_{1-x}Ge_xTe$, and $Sn_{1-x}Ni_xTe$ in comparison with pure SnTe. All doped samples demonstrate ZT_{ave} values higher than that of the pure sample. The maximum increase in ZT_{ave} is about 163%.

While doping increased the rigidity of our samples, our microhardness values are lower than some reported in the literature. This might be due to the large grain size of our samples ($\leq 10 \mu m$). In this respect, smaller grain size in the range of nanometers together with secondary nanosize phases not only could enhance the mechanical properties but could also lower the thermal conductivity by increased phonon scattering.

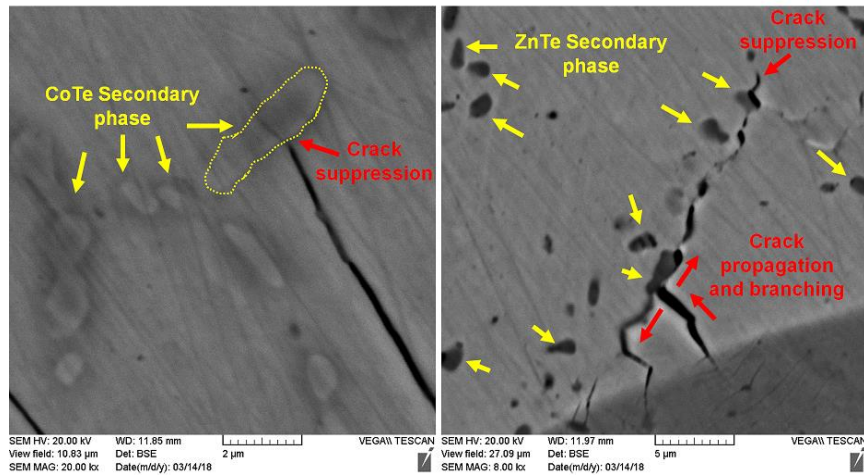
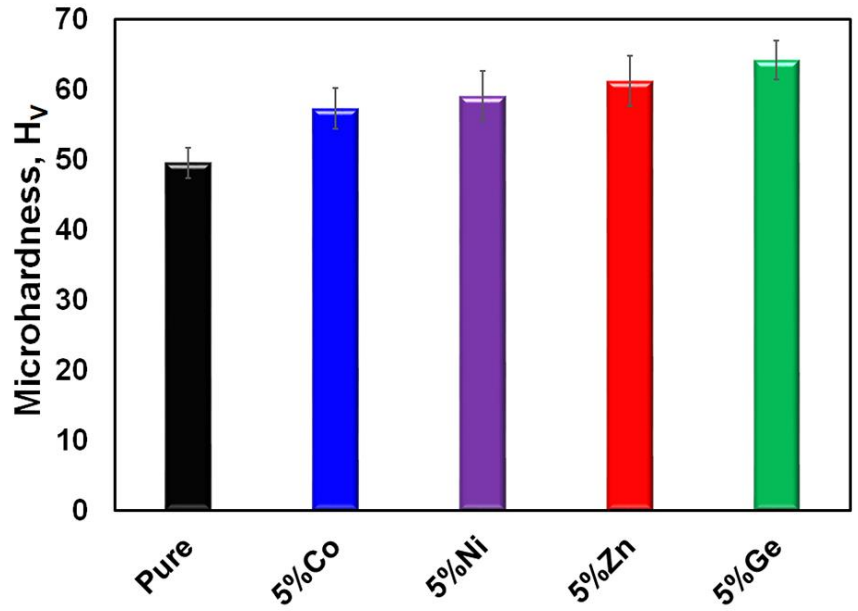


Figure 3-13. (top) Vickers microhardness values, H_v , for the 5% Co-, Ni-, Zn-, and Ge-doped SnTe in comparison with the pure sample. (bottom) Crack growth suppression and crack branching are depicted as the main toughening mechanisms.

3-5. Conclusion

As the lead-free rock-salt analogue of PbTe, SnTe can be used as a green thermoelectric material in real applications, if one can overcome its drawbacks such as high hole concentration, low Seebeck coefficient, and high thermal conductivity through appropriate doping and nanostructuring. The current study suggests that 5% substitution of Co, Ni, and Ge decreases the high-temperature lattice thermal conductivity to the point, where it is close to the amorphous limit ($\kappa_{\text{lat}} \sim 0.4\text{-}0.5$). This is one of the lowest lattice thermal conductivities reported in SnTe-based materials so far. Such reduction in the lattice thermal conductivity can be rationalized in terms of doping-related defects and existence of secondary phases between the grains, which increase the phonon scattering and thus decrease the lattice thermal conductivity. While impurities can affect carrier mobility, the almost unchanged Seebeck coefficient and substantial reduction in the lattice thermal conductivity yield enhancement in the ZT_{max} values for the doped samples. The lattice thermal conductivity is still high at lower temperatures and needs to be reduced if possible. Likewise, the Seebeck coefficient will have been optimized to improve the material TE efficiency. Potentially, this can be achieved by co-doping and nano structuring. Furthermore, the microhardness of doped samples can be further improved through enhanced crack growth suppression and crack branching.

3-6. References

- [1] L. Bell, "Cooling, heating, generating power, and recovering waste heat with thermoelectric systems," (in English), *Science*, Review vol. 321, no. 5895, pp. 1457-1461, SEP 12 2008 2008.
- [2] F. DiSalvo, "Thermoelectric cooling and power generation," (in English), *Science*, Review vol. 285, no. 5428, pp. 703-706, JUL 30 1999 1999.
- [3] J. Heremans, M. Dresselhaus, L. Bell, and D. Morelli, "When thermoelectrics reached the nanoscale," (in English), *Nature Nanotechnology*, Article vol. 8, no. 7, pp. 471-473, JUL 2013 2013.
- [4] J. P. Heremans *et al.*, "Enhancement of thermoelectric efficiency in PbTe by distortion of the electronic density of states," (in English), *Science*, Article vol. 321, no. 5888, pp. 554-557, Jul 2008.
- [5] Y. Z. Pei, X. Y. Shi, A. LaLonde, H. Wang, L. D. Chen, and G. J. Snyder, "Convergence of electronic bands for high performance bulk thermoelectrics," (in English), *Nature*, Article vol. 473, no. 7345, pp. 66-69, May 2011.
- [6] Q. Y. Zhang *et al.*, "Enhancement of thermoelectric figure-of-merit by resonant states of aluminium doping in lead selenide," (in English), *Energy & Environmental Science*, Article vol. 5, no. 1, pp. 5246-5251, Jan 2012.
- [7] L. D. Zhao *et al.*, "High Performance Thermoelectrics from Earth-Abundant Materials: Enhanced Figure of Merit in PbS by Second Phase Nanostructures," (in English), *Journal of the American Chemical Society*, Article vol. 133, no. 50, pp. 20476-20487, Dec 2011.
- [8] K. Biswas *et al.*, "Strained endotaxial nanostructures with high thermoelectric figure of merit," (in English), *Nature Chemistry*, Article vol. 3, no. 2, pp. 160-166, Feb 2011.
- [9] K. Biswas *et al.*, "High-performance bulk thermoelectrics with all-scale hierarchical architectures," (in English), *Nature*, Article vol. 489, no. 7416, pp. 414-418, Sep 2012.

- [10] H. Wang *et al.*, "Right sizes of nano- and microstructures for high-performance and rigid bulk thermoelectrics," (in English), *Proceedings of the National Academy of Sciences of the United States of America*, Article vol. 111, no. 30, pp. 10949-10954, Jul 2014.
- [11] L. D. Zhao *et al.*, "Ultralow thermal conductivity and high thermoelectric figure of merit in SnSe crystals," (in English), *Nature*, Article vol. 508, no. 7496, pp. 373-+, Apr 2014.
- [12] E. K. Chere, Q. Zhang, K. Dahal, F. Cao, J. Mao, and Z. F. Ren, "Studies on thermoelectric figure of merit of Na-doped p-type polycrystalline SnSe," (in English), *Journal of Materials Chemistry A*, Article vol. 4, no. 5, pp. 1848-1854, 2016.
- [13] S. Sassi *et al.*, "Assessment of the thermoelectric performance of polycrystalline p-type SnSe," (in English), *Applied Physics Letters*, Article vol. 104, no. 21, p. 4, May 2014, Art. no. 212105.
- [14] A. Banik, U. S. Shenoy, S. Anand, U. V. Waghmare, and K. Biswas, "Mg Alloying in SnTe Facilitates Valence Band Convergence and Optimizes Thermoelectric Properties," (in English), *Chemistry of Materials*, Article vol. 27, no. 2, pp. 581-587, Jan 2015.
- [15] G. J. Tan *et al.*, "High Thermoelectric Performance of p-Type SnTe via a Synergistic Band Engineering and Nanostructuring Approach," (in English), *Journal of the American Chemical Society*, Article vol. 136, no. 19, pp. 7006-7017, May 2014.
- [16] G. J. Tan *et al.*, "Codoping in SnTe: Enhancement of Thermoelectric Performance through Synergy of Resonance Levels and Band Convergence," *Journal of the American Chemical Society*, vol. 137, no. 15, pp. 5100-5112, Apr 2015.
- [17] Q. Zhang *et al.*, "High thermoelectric performance by resonant dopant indium in nanostructured SnTe," (in English), *Proceedings of the National Academy of Sciences of the United States of America*, Article vol. 110, no. 33, pp. 13261-13266, Aug 2013.
- [18] E. I. Rogacheva, "The problem of doping of non-stoichiometric phases," (in English), *Journal of Physics and Chemistry of Solids*, Article; Proceedings Paper vol. 69, no. 2-3, pp. 259-268, Feb-Mar 2008.

- [19] J. O. Sofo and G. D. Mahan, "OPTIMUM BAND-GAP OF A THERMOELECTRIC-MATERIAL," (in English), *Physical Review B*, Article vol. 49, no. 7, pp. 4565-4570, Feb 1994.
- [20] A. J. Strauss, I. Melngailis, and J. O. Dimmock, "Band structure and laser action in $\text{Pb}_x\text{Sn}_{1-x}\text{Te}$," *Physical Review Letters*, vol. 16, pp. 1193-1196, 1966.
- [21] R. Moshwan, L. Yang, J. Zou, and Z. G. Chen, "Eco-Friendly SnTe Thermoelectric Materials: Progress and Future Challenges," (in English), *Advanced Functional Materials*, Article vol. 27, no. 43, p. 18, Nov 2017, Art. no. 1703278.
- [22] S. Li, X. F. Li, Z. F. Ren, and Q. Zhang, "Recent progress towards high performance of tin chalcogenide thermoelectric materials," (in English), *Journal of Materials Chemistry A*, Review vol. 6, no. 6, pp. 2432-2448, Feb 2018.
- [23] J. He *et al.*, "Enhanced thermopower in rock-salt SnTe-CdTe from band convergence," (in English), *Rsc Advances*, Article vol. 6, no. 38, pp. 32189-32192, 2016.
- [24] R. A. Al Orabi *et al.*, "Band Degeneracy, Low Thermal Conductivity, and High Thermoelectric Figure of Merit in SnTe-CaTe Alloys," (in English), *Chemistry of Materials*, Article vol. 28, no. 1, pp. 376-384, Jan 2016.
- [25] H. J. Wu *et al.*, "Synergistically optimized electrical and thermal transport properties of SnTe via alloying high-solubility MnTe," (in English), *Energy & Environmental Science*, Article vol. 8, no. 11, pp. 3298-3312, 2015.
- [26] B. A. Hunter and C. J. Howard, *Rietica*. Menai, Australia: Australian Nuclear Science and Technology Organization, 2000.
- [27] B. Macalik, M. Siu-Li, and S. Zazubovich, "ITC study of Ga^{+-} , Ge^{2+-} , and Sn^{2+-} -doped alkali halides," (in English), *Radiation Effects and Defects in Solids*, Article; Proceedings Paper vol. 147, no. 1-2, pp. 11-16, 1998.

- [28] T. Tsuboi, "OFF-CENTER DISPLACEMENT OF Ge^{2+} IONS IN KCL CRYSTALS (I) OPTICAL-ABSORPTION SPECTRA," (in English), *Physica B*, Article vol. 193, no. 1, pp. 92-96, Jan 1994.
- [29] M. H. Lee, D. G. Byeon, J. S. Rhyee, and B. Ryu, "Defect chemistry and enhancement of thermoelectric performance in Ag-doped $Sn_{1+\delta-x}Ag_xTe$," (in English), *Journal of Materials Chemistry A*, Article vol. 5, no. 5, pp. 2235-2242, Feb 2017.
- [30] R. Orabi *et al.*, "Ultralow Lattice Thermal Conductivity and Enhanced Thermoelectric Performance in SnTe:Ga Materials," (in English), *Chemistry of Materials*, Article vol. 29, no. 2, pp. 612-620, Jan 2017.
- [31] A. Banik, B. Vishal, S. Perumal, R. Datta, and K. Biswas, "The origin of low thermal conductivity in $Sn_{1-x}Sb_xTe$: phonon scattering via layered intergrowth nanostructures," (in English), *Energy & Environmental Science*, Article vol. 9, no. 6, pp. 2011-2019, 2016.
- [32] R. F. Brebrick, A. J., and Strauss, "Anomalous Thermoelectric Power as Evidence for Two-Valence Bands in SnTe," *Physical Review*, vol. 131, pp. 104-110, 1963.
- [33] P. B. Littlewood *et al.*, "Band Structure of SnTe Studied by Photoemission Spectroscopy," (in English), *Physical Review Letters*, Article vol. 105, no. 8, p. 4, Aug 2010, Art. no. 086404.
- [34] C. M. Jaworski *et al.*, "Valence-band structure of highly efficient p-type thermoelectric PbTe-PbS alloys," (in English), *Physical Review B*, Article vol. 87, no. 4, p. 10, Jan 2013, Art. no. 045203.
- [35] H. S. Kim, Z. M. Gibbs, Y. L. Tang, H. Wang, and G. J. Snyder, "Characterization of Lorenz number with Seebeck coefficient measurement," (in English), *Apl Materials*, Article vol. 3, no. 4, p. 5, Apr 2015, Art. no. 041506.
- [36] Y. Z. Pei *et al.*, "Interstitial Point Defect Scattering Contributing to High Thermoelectric Performance in SnTe," (in English), *Advanced Electronic Materials*, Article vol. 2, no. 6, p. 8, Jun 2016, Art. no. 1600019.

- [37] J. He *et al.*, "Valence band engineering and thermoelectric performance optimization in SnTe by Mn-alloying via a zone-melting method," (in English), *Journal of Materials Chemistry A*, Article vol. 3, no. 39, pp. 19974-19979, 2015.
- [38] G. J. Tan *et al.*, "High Thermoelectric Performance SnTe-In₂Te₃ Solid Solutions Enabled by Resonant Levels and Strong Vacancy Phonon Scattering," (in English), *Chemistry of Materials*, Article vol. 27, no. 22, pp. 7801-7811, Nov 2015.
- [39] G. J. Tan *et al.*, "Valence Band Modification and High Thermoelectric Performance in SnTe Heavily Alloyed with MnTe," (in English), *Journal of the American Chemical Society*, Article vol. 137, no. 35, pp. 11507-11516, Sep 2015.
- [40] Z. W. Zhou *et al.*, "Multiple effects of Bi doping in enhancing the thermoelectric properties of SnTe," (in English), *Journal of Materials Chemistry A*, Article vol. 4, no. 34, pp. 13171-13175, 2016.
- [41] D. G. Cahill, S. K. Watson, and R. O. Pohl, "LOWER LIMIT TO THE THERMAL-CONDUCTIVITY OF DISORDERED CRYSTALS," (in English), *Physical Review B*, Article vol. 46, no. 10, pp. 6131-6140, Sep 1992.
- [42] S. Perumal, S. Roychowdhury, and K. Biswas, "Reduction of thermal conductivity through nanostructuring enhances the thermoelectric figure of merit in Ge_{1-x}Bi_xTe," (in English), *Inorganic Chemistry Frontiers*, Article vol. 3, no. 1, pp. 125-132, 2016.